Dislocation-Based Modeling of Creep Deformation and Fracture in Modified 9Cr-1Mo Steels

A Dissertation

Presented in Partial Fulfillment of the Requirements for the

Doctor of Philosophy

with a

Major in Mechanical Engineering

in the

College of Graduate Studies

University of Idaho

by

Mehdi Basirat

Major Professor: Gabriel P. Potirniche, Ph.D.

Committee Members: Robert Stephens, Ph.D.; Michael Maughan, Ph.D.; Indrajit Charit, Ph.D.

Department Administrator: Steven Beyerlein, Ph.D.y

May 2018

AUTHORIZATION TO SUBMIT DISSERTATION

This Dissertation of Mehdi Basirat, submitted for the degree of Doctor of Philosophy with a major in Mechanical Engineering and titled " Dislocation-Based Modeling of Creep Deformation and Fracture in Modified 9Cr-1Mo Steels" has been reviewed in final form. Permission, as indicated by the signatures and dates given below, is now granted to submit final copies to the College of Graduate Studies for approval.

Major Professor _____Date_____
Gabriel Potirniche, Ph.D.

Committee Members _____Date_____
Robert Stephens, Ph.D.

_____Date_____
Michael Maughan, Ph.D.

_____Date_____
Indrajit Charit, Ph.D.

Department Administrator _____Date_____
Steven Beyerlein, Ph.D.

ABSTRACT

The very high-temperature reactor (VHTR) represents the next generation of high temperature gas-cooled reactors designed for the future nuclear power plants. The VHTR is operated at higher pressure and temperature for longer time compared with the Pressurized Water Reactors (PWRs). Modified 9Cr-1Mo steel is a suitable candidate material for VHTR pressure vessels. Although 9Cr-1Mo steel has good creep resistance, its microstructure degrades during manufacturing processes such as welding or high temperature operation. Hence, investigating the creep resistance of welded 9Cr-1Mo steel is crucial.

In this research, a micromechanical model is developed for the evaluation of creep deformation and rupture times of modified 9Cr-1Mo steel specimens. Creep deformation in metals is generally induced by dislocation generation, motion, and annihilation. Evolution of the dislocation density was modeled by considering the generation and annihilation of single and dipole dislocations. In addition to dislocation motion, there are several other factors which determine the creep resistance of this steel. Among these, the most significant are precipitate coarsening, solid solutions depletion, and void/crack nucleation and growth. The evolution of these mechanisms was accounted for by introducing specific continuum damage terms.

In this study a one-dimensional (1-D) model was successfully applied to specimens made of the as-received 9Cr-1Mo steel. Comparison of the numerical model results with experimental data showed satisfactory agreement. However, a 1-D model has several limitations including applicability limitation to only 1-D stress state problems, and the inability of studying components made of more than one material. Therefore, developing a three-dimensional (3-D) comprehensive model is required to meet the objective of this research

which was the prediction of creep life in welded joints made of modified 9Cr-1Mo steel. The developed 1-D model was modified and implemented in the commercial finite element software ABAQUS by means of a User Material Subroutine (UMAT). The creep of welded 9Cr-1Mo specimens was simulated by considering different material behavior in the heat affected zone (HAZ) and the welded material. Several creep experiments were conducted on 9Cr-1Mo welded specimens. The tensile creep tests were performed at a temperature range of 550-700 ˚C and stress level of 80-200 MPa. Finally, simulation results were compared to experiments, and excellent agreement was obtained between experiments and simulations.

ACKNOWLEDGMENTS

I would like to thank my advisor Dr. Gabriel Potirniche for encouraging me to engage in creative research work through his endless guidance and support. His guidance and immediate responses to my ideas have been of invaluable help to me in achieving significant advances in research. His technical excellence as well supportive personality not only helped me throughout these years, but also taught me how to continue on my personal as well as technical life.

I would like to thank my committee members, Dr. Charit, Dr. Stephens, and Dr Maughan for their advice and instruction. Immense thanks are also owed to my parents for their unfettered affection and support.

I would like to gratefully acknowledge the Nuclear Energy University Program (NEUP) for providing the financial support for this research through DOE grant 42246, release 59.

Lastly, I would like to thank Dr. Amin Ahmadzadeh and his Lovely wife Maryam for always being there for me, which gave me the confidence in my work and always motivated me during the hard times.

DEDICATION

This work is dedicated to my late mother, Parvin Mardani. I was lucky to have her love, support, and encouragement in my life.

TABLE OF CONTENTS

LIST OF FIGURES

LIST OF TABLES

Chapter 1 - Introduction

1.1 Motivation

It is estimated that in the next 20 years the world demand for power supplies will increase by up to 50%. Thus, developing advanced energy resources becomes essential. The developed energy sources must be sustainable, environmental friendly and cost effective. Nuclear power meets these requirements for large-scale power generation. The development of advanced nuclear power plants follows under the Next Generation Nuclear Plant (NGNP) program. The NGNP program focuses on the development of the Very-High-Temperature Reactor (VHTR), which represents the next generation of high temperature gas-cooled reactors. The VHTR is a helium-cooled, graphite-moderated reactor with a once-through uranium fuel cycle. VHTR design specifications include higher operating temperatures, longer design life, and higher working pressures compared with previous reactor types, which makes it necessary to consider new metallic alloys with improved creep properties for reactor pressure vessels and reactor internals. One such candidate material is modified 9Cr-1Mo steel.

1.2 Thesis contributions

This dissertation focuses on developing numerical algorithms to simulate the high temperature deformations in modified 9Cr-1Mo steel components, with a particular emphasis on implementing the numerical models in the finite element software ABAQUS Standard in order to enable the simulation and prediction of component service life when exposed to high temperatures. Furthermore, several experiments have been conducted on the as-received and welded material. This thesis presents both numerical model simulations and the experimental

results for both as-received and welded 9Cr-1Mo steel specimens. Moreover, a combined creep and isotropic hardening plasticity model has been developed and implemented in ABAQUS in order to study the creep fracture behavior of high temperature components.

1.3 Thesis organization

The content of this thesis is organized in five chapters, as follows. Chapter 2 reviews the development of a uniaxial creep model to study the creep behavior of modified 9Cr-1Mo steel. Moreover, it covers the simulation results and their corroboration with the experiments for creep strains and creep strain rates at different stress levels and temperatures. The content of this chapter has been published in the *International Journal of Plasticity*.

Chapter 3 focuses on the development of a creep damage model for welded specimens made of modified 9Cr-1Mo steel. In this model a forward explicit integration scheme was employed to solve the constitutive equations of creep. The model was successfully applied to welded specimens for different conditions, however the explicit integration scheme caused the integration procedure to be sensitive on the time increment. The model was not applicable to large time steps, which is the main condition of creep deformations. The content of this chapter was published in the *American Nuclear Society (ANS)* 2012 winter Meeting and Nuclear Technology Expo Proceedings.

Chapter 4 introduces and discusses the integration and implementation of the creep damage model using an implicit integration scheme in ABAQUS. The model was applied to several test cases, namely several welded specimens and a bolted flange. The model results match well the experimental testing results. The content of this chapter was published as a

research paper in the journal *Metals*.

Chapter 5 presents a unified creep-plasticity model. Combining plastic and creep deformations in a single theory is useful for components that are subjected to larges stresses over long periods at elevated temperatures. The model combines creep-damage and isotropic plasticity, and it has been applied to study the stress and strain fields in a cracked specimen.

Chapter 2 : A Dislocation Based Creep Model Combined with Continuum-Damage to Study the High Temperature Behavior of Modified 9Cr-1Mo Steel

"A Dislocation Based Creep Model Combined with Continuum-Damage to Study the High Temperature Behavior of Modified 9Cr-1Mo Steel." *International Journal of Plasticity 37, 95-107, 2012*

2.1 Introduction

Recently, several research studies have been performed to elucidate and model the creep behavior in metals. Preußner et al. (2009) developed a dislocation density-based creep model, and the creep behavior of single fcc, bcc, and hcp crystals was studied using this model. Venkataramani et al. (2008) developed a finite element crystal plasticity creep model and performed a parametric study to identify the primary microstructural parameters causing early crack initiation by load shedding in Ti-6242 during creep. They used the Schmid factor and the grain size and shape as the most critical parameters to prevent stress concentration and crack initiation.

Fischer and Svoboda (2011) extended the Nabarro creep model to the general dislocation microstructure. At low stress levels the creep is controlled by the generation/annihilation of vacancies at dislocations jogs. They developed a model based on vacancy activity, dislocation microstructure and applied stress state, and simulation results were compared to experimental measurements of creep rates in P91 steel at low stresses and high temperatures. Oberson and Ankem (2009) studied the creep deformation behavior of α-Ti–1.6 wt.% V. The formation of twinning at high strains was explained by dislocation pileups.

Morra et al. (2009) studied the precipitate coarsening in tempered SAE 52100 steel. It has been shown that the growth of carbide precipitates is in correlation with the plastic strain evolution. Creep strength of as-cast and annealed Fe–Ni–Al alloy has been investigated by Muñoz-Morris (2009). It has been shown that in the annealed alloy with less volume fraction of precipitates the creep strength decreases significantly while the ductility increases. Horstemeyer et al. (2011) performed a review on the development and the use of internal state variable theory based on the Coleman and Gurtin thermodynamics formulations for dislocations, creep, and continuum damage mechanics.

The material of interest in this study is modified 9Cr-1Mo steel, which was developed in the late 1970's for use in fossil fuel power plants, according to Swindeman et al. (2004). The main advantages of modified 9Cr-1Mo steel which make it a suitable candidate for VHTR structures are limited radiation hardening at higher temperature, lower shift in the Ductile-to-Brittle Transition Temperature (DBTT), low thermal expansion coefficient, and better void swelling resistance than austenitic steels. Furthermore, modified 9Cr-1Mo steel is a precipitate-hardened alloy with a stable microstructure. The mechanical behavior and chemical composition of the modified 9Cr-1Mo steel have been optimized in recent years. This steel contains alloying elements such as Nb and V, which form fine and stable particles, and help to improve its creep strength.

The creep behavior of 9Cr-1Mo steel has been studied by several researchers during the past years. Sklenicka et al. (1994, 2003) suggested that the role of dislocation substructure is dominant for the creep behavior of 9Cr-1Mo steels. According to their study, carbide particles merely stabilize the substructure, while the dislocation structure and/or substructure development determine the creep behavior of the steel. Spigarelli et al. (1997) concluded that

the high values of the activation energy and the creep stress exponent indicate that in the high stress regime creep strain is controlled by dislocation movement and particle-dislocation interaction (Orowan by-pass and/or climb). Böck et al. (2005) have performed an extensive research on the finite element modeling of the creep behavior of modified 9Cr-1Mo steel. Instead of using standard evolution laws for predicting long term creep, they proposed to utilize models which were based on microstructural variables. Artz and Wilkinson (1986) proposed a dislocation based model for creep. The model is valid for local and general climb of dislocations regardless of the climb mechanisms. In this model the threshold stress is defined as the dislocation-particle attractive interaction. Creep models based on microstructure have also been proposed by several other authors (Ghoniem et al., 1990; Blum et al., 2002; Raj et al., 1995, and Raj, 2002). The common theme of these models is that they employ multiple microstructural variables based on averaged microstructural quantities, such as the mobile dislocation density, static dislocation density, boundary dislocation density, subgrain radius, precipitate radius, precipitate concentration and glide energy.

Fujimitsu (2006) studied the material degradation in modified 9Cr-1Mo steel welds during creep deformations. He proposed a new approach for the evaluation of creep degradation and life assessment in modified 9Cr-1Mo steel welds by the hardness measurement method. The uniaxial high-temperature creep behavior of the base metal and weldment of 9Cr-1Mo-Nb-V steel was studied by Gaffard et al. (2005). They also investigated the type IV failure in the heat-affected zone. Furthermore, a one-dimensional model based on a power law and the Monkman–Grant models were proposed for lifetime assessment of the weldment. Besson et al. (2009) proposed a model, which integrated the power-law creep, diffusional creep and a simple damage term for simulating the creep-failure behavior of the

inter-critical heat affected zone. Fournier et al. (2011) introduced a micromechanically-based model considering the dislocation density and subgrain coarsening in order to predict the cyclic softening in 9–12%Cr martensitic steels. The model shows a good consistency with the experiments for strains over 0.3%. Sauzay (2009) studied the effect of annihilation of low angle boundaries and the micro-grain coarsening during creep deformation of tempered martensite steel, and developed physically-based computations following the Read and Shockley model.

Several studies have been performed to evaluate the effect of precipitates on the creep behavior of 9Cr-1Mo steel. The type, size and volume fraction of precipitates in the modified 9Cr-1Mo steel were investigated by Chilukurua et al. (2009). They showed that V forms fine particles of M_2X, which may provide short-term high creep strength, but the rapid coarsening of M_2X at the subgrain boundaries and Z-phase precipitation decrease the overall creep resistance. Kabadwal et al. (2010) found that the primary creep stage of a specimen tempered at 500 ˚C was controlled by the mobile dislocation density reduction and is a recovery process, while for the specimens tempered at 800 ˚C, the primary creep is controlled by the increase in creep resistance due to the fine precipitation of VX. Also, it has been mentioned that the growth of $M_{23}C_6$ in the tertiary creep stage relates to the creep rate increase.

In addition to temperature and applied stress, there are several microstructural parameters, which influence the creep behavior of modified 9Cr-1Mo steel. These microstructural factors that degrade the material have been considered in this model as creep damage terms. Creep damage is introduced to describe the progressive loss of load-bearing capacity, which manifests itself as tertiary creep in an isothermal constant load/stress test. In an effort to relate this empirical definition with the many studies of material degradation during creep, Ashby and Dyson identified four broad categories of creep damage due to loss of internal

and external sections, microstructure degradation and gaseous environmental attack. Each category was found to contain several micro-mechanisms (Miannay, 2001).

In the current research, a dislocation-based creep model combined with a continuum-damage model was employed to simulate the creep behavior of modified 9Cr-1Mo steel. The Orowan's equation, relating creep rate with the density of mobile dislocations and their glide velocity, was employed as a foundation for the model. The evolution of dislocations was estimated based on a model proposed by Blum et al. (2002). The effects of precipitate coarsening, solid solution depletion and cavity nucleation were taken into account by including continuum damage terms into the Orowan's equation. In order to evaluate the effects of precipitate coarsening and solid solution depletion, the Orowan's formula was modified by the respective damage terms similarly to the procedure outlined by Semba et al. (2005). Another mechanism affecting creep strain in materials is void and crack formation. Yin et al. (2008) modified the McLean et al. (2000) formula by defining a term for cavity nucleation in 9Cr steels. In this paper, a similar procedure was used, by adding a void formation term to the Orowan's equation, which makes it possible to evaluate the effect of void nucleation on creep strain rate.

2.2 Experimental procedure

The chemical composition and room temperature tensile properties of ASTM A387 Grade 91 CL2 steel investigated are shown in Tables 2-1 and 2-2, respectively. Hot rolled modified 9Cr-1Mo plates were received in a normalized condition at 1038 ^{o}C for 240 minutes and tempered at 788 ^{o}C for 43 minutes. The plate dimensions were 104 mm × 104 mm × 12.7 mm. Scanning and transmission electron microscopy (SEM and TEM) were performed to

characterize the microstructural characteristics of the modified 9Cr-1Mo steel. Creep specimens with a gauge length of 25.4 mm and gauge diameter of 6.35 mm were machined from the steel plates. The material has a yield strength of 533 MPa, an ultimate tensile strength of 683 MPa and percentage elongation at fracture of 26% at room temperature. Creep tests were performed at several combinations of temperature (600, 650 and 700 ^{o}C) and stress (35-350 MPa) using an Applied test systems (ATS) lever arm (20:1) creep tester.

Table 2-1. Chemical composition (wt.%) of Grade 91 steel used in this study.

Elements	Nominal	Measured
Cr	8.00 - 9.50	8.55
Mo	0.85 - 1.05	0.88
V	0.18 - 0.25	0.21
Nb	0.06 - 0.10	0.08
C	0.08 - 0.12	0.1
Mn	0.30 - 0.60	0.51
Cu	0.4(max.)	0.18
Si	0.20 - 0.50	0.32
N	0.03 - 0.07	0.035
Ni	0.40(max.)	0.15
P	0.02(max.)	0.012
S	0.01(max.)	0.005
Ti	0.01(max.)	0.002
Al	0.02(max.)	0.007
Zr	0.01(max.)	0.001
Fe	Balance	Balance

Table 2-2. Mechanical properties of Grade 91 steel used.

Yield Strength (MPa)	Tensile Strength (MPa)	Elongation	
		Gage Length (mm)	%
533.60	683.27	50.80	26.0

A detailed microstructural study of the modified 9Cr-1Mo steel has been performed by utilizing SEM using secondary electron imaging mode and TEM. Furthermore, the energy dispersive spectroscopy (EDS) was used for the elemental analysis and precipitate characterization. A description regarding the microstructural analysis has been avoided here; hence the results are similar to what has already been described in the literatures. A detailed description may be found in Sklenicka et al. (1994, 2003), Shrestha et al. (2012) or many others.

2.3 Model description

2.3.1 Evolution and kinetics of dislocations

In crystalline materials in the power law regime creep generally occurs by dislocation glide and climb. In order to simulate the creep behavior of a material, it is necessary to distinguish between the controlling mechanisms of dislocations motion. There are different methods to analyze the mechanisms of dislocations motion in a material. Stress change test and in-situ observation of dislocation motion are two common methods for understanding the dislocations motion mechanisms. Oikawa et al. (1978) studied the effect of stress changes on the creep behavior of some solid solutions. They mentioned that during a creep test, if the amount of instantaneous plastic strain under a rapid stress change is zero or negligible, the glide motion of dislocations is viscous. Hayakawa et al. (2009) performed stress change tests on modified 9Cr–1Mo and 2.25Cr–1Mo steel to evaluate their creep deformation mechanisms. No instantaneous plastic strain was observed during the stress change test, thus they concluded that the motion of dislocations was viscous. Furthermore, Terada et al. (2002) have made an in-situ observation of dislocation motion in Fe-W and Fe-Mo solid solutions. Analysis of the

video records of dislocation behavior in both Fe-W and Fe-Mo steels showed that the dislocation glide velocities were constant in both materials. It has also been observed that the dislocation dragged solute atmosphere with themselves. So, it can be concluded that the dislocations motion is viscous. According to this conclusion, the model proposed by Blum et al. (2002) for the viscous glide of dislocation was utilized in this study. In this model the accumulation of creep deformation is linked to the dislocation generation, motion, and annihilation.

In the present model, the Orowan's equation is employed to compute the creep strain rate. Because the stress levels tested were above 60 MPa, the only mechanism considered is the power law creep. At stresses lower than this value, other mechanisms, such as the Nabarro-Herring Newtonian creep should also be taken into consideration. Orowan's equation relates the creep strain rate caused by dislocation motion to the density of mobile dislocations, Burgers vector and the glide velocity. Orowan's equation is valid for either glide or climb controlled motion of dislocations (Poirier, 1985),

$$\dot{\varepsilon} = \frac{\rho_m b v_g}{M} \tag{2-1}$$

where b is Burgers vector, M is the Taylor factor, v_g is the glide velocity and ρ_m is the density of the mobile dislocations. It is convenient to represent the total dislocation density in a material as the summation of the mobile and dipole dislocations

$$\rho = \rho_m + \rho_{dip}, \tag{2-2}$$

Where ρ is the total dislocation density and ρ_{dip} is the dislocation dipole density. The evolution of dislocations can be described in terms of the generation and annihilation of single and dipole

dislocations. The subgrain formation and growth have not been taken into account in this study. It is assumed that all their effects are implicitly present in one of the curve-fitting parameters k_Λ, which is introduced below. Future studies should focus on the modeling of the subgrain formation effect on creep deformation in Cr-Mo steels. The generation of single dislocations and the formation and annihilation of dipoles are modeled according to the Blum model as follows

$$\dot{\rho}_m = \dot{\rho}_{m,gen} - \dot{\rho}_{m,spon} - \dot{\rho}_{dip,gen}, \tag{2-3}$$

$$\dot{\rho}_{dip} = \dot{\rho}_{dip,gen} - \dot{\rho}_{dip,spon} - \dot{\rho}_{dip,c}. \tag{2-4}$$

Here, $\dot{\rho}_m$ is the rate of evolution of the mobile dislocations, $\dot{\rho}_{m,gen}$ is the rate of generation of mobile dislocations, $\dot{\rho}_{m,spon}$ is the rate of spontaneous annihilation of mobile dislocations, $\dot{\rho}_{dip}$ is the evolution rate of dipoles dislocations, $\dot{\rho}_{dip,gen}$ is the rate of generation of dipoles, $\dot{\rho}_{dip,spon}$ is the spontaneous annihilation of the dipoles, and $\dot{\rho}_{dip,c}$ is the climb annihilation of dipoles. The rate of generation of the mobile dislocations is defined as

$$\dot{\rho}_{m,gen} = \frac{M\dot{\varepsilon}}{b\Lambda}, \tag{2-5}$$

where M represents the Taylor factor, $\dot{\varepsilon}$ the creep strain rate, and Λ represents the total distance a dislocation glides and is proportional to the average spacing of total dislocation density as expressed by

$$\Lambda = k_\Lambda \rho^{-0.5}, \tag{2-6}$$

where k_Λ is a material parameter, which in the present model is assumed to be a function of temperature and stress. The magnitude of k_Λ will decrease with increasing temperature and

stress. Two dislocations with Burgers vectors of opposite sign approaching each other on a slip plane within a distance smaller than a critical value, d_{dip} , will form a dipole. The average rate of annihilation of the mobile dislocations by forming dipoles on the active slip planes is defined as

$$\dot{\rho}_{m,ani} = \frac{4M\dot{\varepsilon}d_{dip}\rho_m}{b(n_g)}. \tag{2-7}$$

In the above equation $\dot{\rho}_{m,ani}$ is the rate of annihilation of mobile dislocations spontaneously and by forming dipoles, in other words it is equal to the summation of the $\dot{\rho}_{m,spon}$ and $\dot{\rho}_{dip,gen}$. The term $(\frac{M}{b})2d_{dip}\dot{\varepsilon}$ represents the change in time of the volume fraction single dislocations that can form dipoles. The term $1/(2n_g)$ is the average dislocation fraction with opposite Burgers vector sign, and n_g is the number of active slip planes (Blum et al., 2002). The distance d_{dip} is the capturing dipole configuration distance for either two screw or edge dislocations of opposite sign, which approach each other to form a stable dipole. The parameter d_{dip} is a function of applied stress, and it varies between 12-16 nm for stress levels between 100-200 MPa. The annihilation distance of edge and screw dislocations are equal to y_e =4 *nm* and y_s = 50 *nm* respectively (Fournier et al., 2011). It can be observed that the parameter d_{dip} is within the range of edge and screw dislocation annihilation distances, and shows a good agreement with the experimental values.

$$d_{dip} = \frac{M}{8\pi(1-\nu)}\frac{Gb}{\sigma}. \tag{2-8}$$

In the above equation, G is the shear modulus and σ is the applied stress. Within a certain distance, d_{spon}, between the slip planes of the dipole dislocations, the dipoles will annihilate spontaneously and form point or agglomerate defects behind, Blum et al. (2009). The spontaneous dislocation annihilation rate is defined as

$$\dot{\rho}_{m,spon} = \frac{d_{spon}}{d_{dip}} \dot{\rho}_{m,ani} . \tag{2-9}$$

The dipole dislocations may draw near each other by climbing or cross slipping over the parallel slip planes in-between until their spacing reaches d_{spon}. Neglecting the subgrain formation, the process of annihilation of the dipoles represents the dynamic recovery. The rate of dipole annihilation climb or cross slip is assumed to be proportional with the climb velocity of dislocations,

$$\dot{\rho}_{dip,c} = \rho_{dip} \frac{4v_c}{(d_{dip} - d_{spon})} . \tag{2-10}$$

The climb velocity is the velocity with which edge dislocations move perpendicularly to the slip plane and can be defined according to Takeuchi et al. (1976),

$$v_c = \frac{D\Omega\sigma_c}{bK_B T} , \tag{2-11}$$

$$\sigma_c + \frac{v_c}{B} = \frac{Gb}{2\pi(1-\nu)} \frac{2}{d_{spon} + d_{dip}} , \tag{2-12}$$

where Ω is the atomic volume, K_B is the Boltzmann constant, T is the temperature, D is the coefficient of self-diffusion, and the climb stress σ_c is found from Eq. (2-12). In this equation, B is the dislocation mobility term and defined as,

$$B = \frac{9\Omega D_{sol} K_B T}{M C_0 G^2 b^7 \varepsilon_a^2 \ln(\frac{r_2}{r_1})}. \quad (2\text{-}13)$$

The other mechanism which may annihilate dipole dislocations spontaneously is by passing a single dislocation near a dipole. The new single dislocation will annihilate with one side of the dipole. The remaining one will form a new single dislocation so that the single dislocation density will not change. The spontaneous rate of annihilation of dipoles is an athermal process, and is formulated as follows

$$\dot{\rho}_{dip,ani} = \frac{2M\dot{\varepsilon}d_{spon}\rho_{dip}}{bn_g}. \quad (2\text{-}14)$$

The kinetics of dislocation motion can be analyzed considering that the glide velocity of dislocations is a function of the effective stress, temperature, dislocation interactions, dislocation mobility, solute atom sizes, and the diffusion coefficient of solute atoms in the matrix. The effective applied stress is calculated from the applied external stress σ and the athermal stress component σ_i,

$$\sigma^* = \sigma - \sigma_i. \quad (2\text{-}15)$$

The athermal stress component resulting from the interdislocation interaction of both single dislocations and dipoles is

$$\sigma_i = \alpha MCGb\sqrt{\rho_m + c_{dip}\rho_{dip}}, \quad (2\text{-}16)$$

where α is a dislocation interaction constant, C is the inelastic deformation factor and c_{dip} is a weight factor. The glide velocity is directly proportional with the effective stress

$$v_g = B\sigma^* \quad (2\text{-}17)$$

where D_{sol} is the solute atom diffusion coefficient in solvent atoms, C_0 is the solute concentration, r_1 and r_2 are the outer and inner cut-off radii of the dislocation stress field, and ε_a is the relative size misfit between solute and solvent atoms.

2.4 Formulation of creep damage

2.4.1 Solid solution depletion

Experiments in 9Cr-1Mo have indicated that the precipitation of Fe_2Mo Laves phase decreases creep resistance. The decrease in creep resistance is caused by the Mo depletion in the subgrain matrix during long term high temperature and stress exposure. Mo is added to the material to increase the creep resistance by solid solution strengthening mechanism. While the low volume fraction and the large size of the Laves phase (Fe_2Mo) could rarely help decrease the dislocations motion. The large size Laves phases at grain boundaries are the most likely source of cavity nucleation and the intergranular fracture because they are brittle in nature and have the tendency to absorb dislocations (Lee et al., 2006). This mechanism is addressed in the next section concerning the damage evolution by void nucleation and crack formation. According to Kadoya, et al. (1997) and Semba et al. (2008), the damage caused by depletion of the Laves phase (D_s) is defined as

$$D_s = 1 - \frac{\bar{C}_t}{C_0}, \quad \text{where, } 0 < D_s < 1, \tag{2-18}$$

where C_0 is the initial concentration of solid solution, and $\bar{C}_t$ is their concentration at time t. In addition, the rate of change of D_s is

$$\dot{D}_s = K_s D_s^{1/3}(1 - D_s), \tag{2-19}$$

with the constant K_s defined as

$$K_s = \left[48\pi^2 (c_0 - \frac{c_e}{c_\beta})^{1/3} n^{2/3} D \right]. \quad (2\text{-}20)$$

Here, D is the diffusion coefficient of Mo in matrix, n the number of precipitate particles and c_β the concentration of solid solution in the precipitate of laves. Semba et al. (2008) computed the values of c_0 and c_e using Thermo-Calc and found c_0 = 0.56 mol% and c_e = 0.33 mol%.

2.4.2 Precipitate particle coarsening

The precipitate coarsening in modified 9Cr-1Mo steel plays an important role in the creep resistance of this material. Nakajima et al. (2003) studied the coarsening of $M_{23}C_6$ and MX precipitates in T91 steel during creep. They reported that the size of MX particles is smaller than that of $M_{23}C_6$, but the coarsening of $M_{23}C_6$ found on the subgrain boundaries and MX particles was consistent with the third power dependence of particle radius with activation energy similar to lattice diffusion. With the coarsening of the precipitates, the interparticle spacing between the precipitates increases. The increased interparticle spacing decreases the stress required for dislocations to climb over precipitates. Following Semba et al. (2008), the damage caused by the coarsening of $M_{23}C_6$ precipitate particles is modeled as

$$D_P = 1 - \frac{P_0}{P_t}, \quad (2\text{-}21)$$

where P_0 is the initial particle diameter and P_t is the particle size at time t. The rate of precipitate particle coarsening is described by

$$\dot{D}_p = \frac{k_p}{3}(1-D_p)^4, \qquad (2\text{-}22)$$

where k_p is the rate constant normalized by the third power of the initial particle size. As a result, D_P varies between zero and one.

2.4.3 Void nucleation and crack formation

As was mentioned previously, creep damage in modified 9Cr-1Mo steel is governed by different mechanisms, with one of the most important one being void nucleation and cavity formation. Creep cavities and crack formation are generally controlled by grain-boundary sliding. Decohesion caused by the stress irregularities at grain boundaries will initiate cavities and cracks. The grain boundary interaction with the subgrains or second-phase particles will form possible crack nucleation sites (Viswanathan, 1989). In 9Cr-1Mo steel cavities usually nucleate at triple junctions or at particles located on grain boundaries. It is observed that the major crack formation mechanism in this material is grain deformation. Moreover, as small inter-granular cavities coalesce, cavity growth increases, as observed by Gaffard et al. (2005). Typical voids and possible wedge crack formation by coalescence of small cavities are shown in Figure 2-1 for the creep-damaged specimens at 650 °C and 150 MPa. These effects are accounted for by using a damage parameter D_N for the cavity nucleation and growth. There are several void growth, and void coalescence modeling approaches available such as Gurson's constitutive law or damage indicators developed by Fischer et al (1995). In this work the formulation proposed by Yin et al. (2008) has been chosen. In this model the rate of evolution of D_N is defined as,

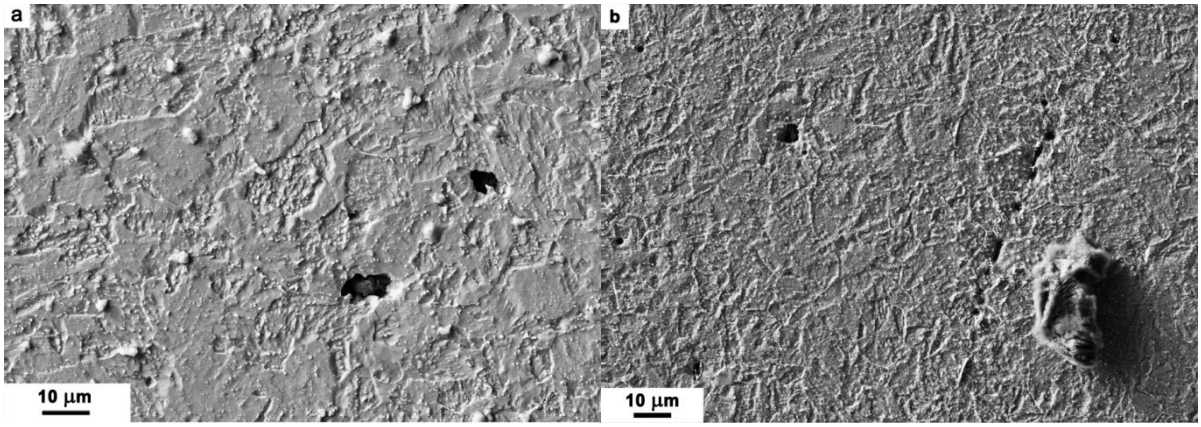

Figure 2-1. Voids nucleated in crept specimens at 650 ˚C and stress of 150 MPa

$$D_N = A\dot{\varepsilon}\varepsilon^{0.9}, \tag{2-23}$$

where the material constant A is a function of temperature and stress. At large strains and high strain rates, the magnitude of D_N may be equal to or larger than one. This will cause a divergence in the computation at high stress and strain; therefore the magnitude of D_N should not reach one, thus $0 < D_N < 1$.

2.5 Results and discussion

Inserting the damage terms in the Orowan's equation (Eq. (2-1)), the formula for computing creep strain rate becomes

$$\dot{\varepsilon} = \frac{b \cdot \rho_m \cdot v_g}{M(1-D_s)(1-D_P)(1-D_N)}. \tag{2-24}$$

In general, different creep mechanisms may be divided into three categories: viscous creep, power-law creep and power-law break down creep. The current model was utilized to simulate the creep behavior of the modified 9Cr-1Mo steel in power-law creep region. For the experiments conducted on the modified 9Cr-1Mo specimens at temperature levels equal to

600, 650 and 700 ˚C and stress levels over 80 MPa, the material follows the power low creep behavior. In this study, the numerical model was applied to the experimental data for temperatures from 600 to 700 ˚C and stress levels from 100 MPa to 200MPa. In the simulation procedure the engineering stress has been used. The computed results were compared with the experimental results, and they show a satisfactory match.

Figure 2-2 shows the comparison of creep strain rates predicted by the model with experimental data for the temperature of 650 ˚C and stresses of 150 MPa and 200 MPa. For the same temperature and stress levels, the creep strain variations with time are shown in Figure 2-3. For crept specimens tested at stresses of 80 MPa and 100 MPa and temperature of 700 ˚C, the creep strain rates and creep strain versus time are shown in Figures 2-4 and 2-5, respectively.

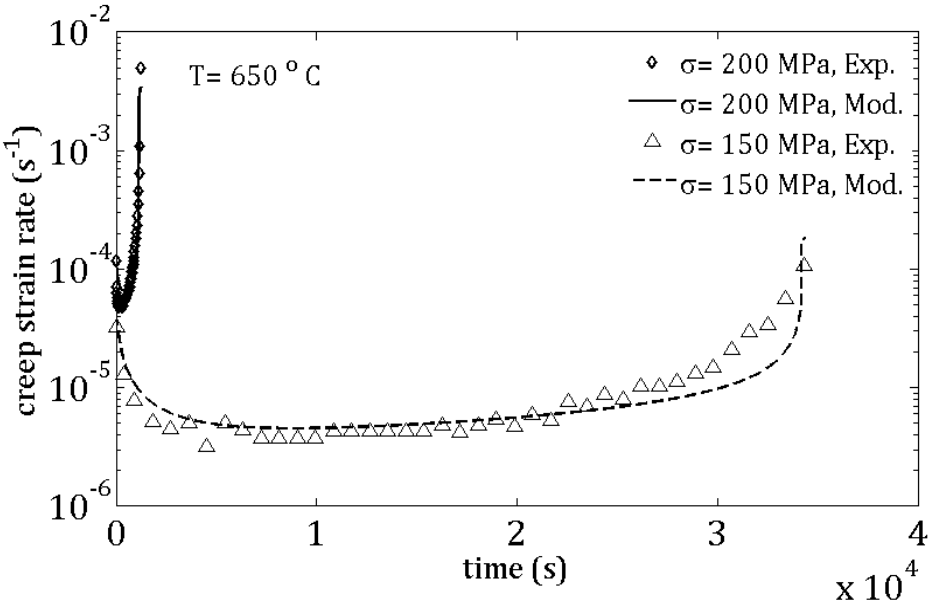

Figure 2-2. Comparison between the model predictions and experimental data for creep tests at 650 ˚C and stresses of 150 MPa and 200 MPa.

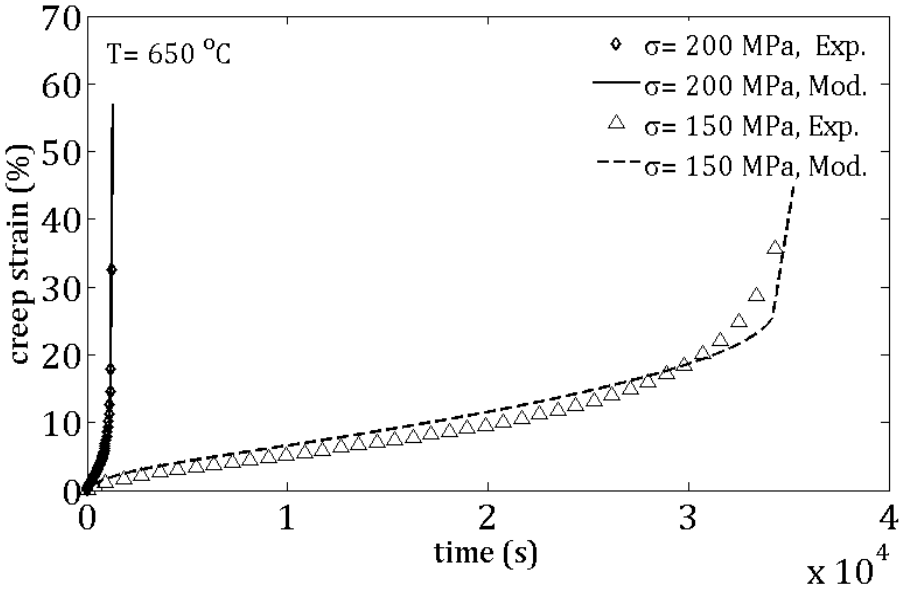

Figure 2-3. Comparison between the model predictions and experimental data for the creep strains at 650 ˚C and stresses of 150 MPa and 200 MPa.

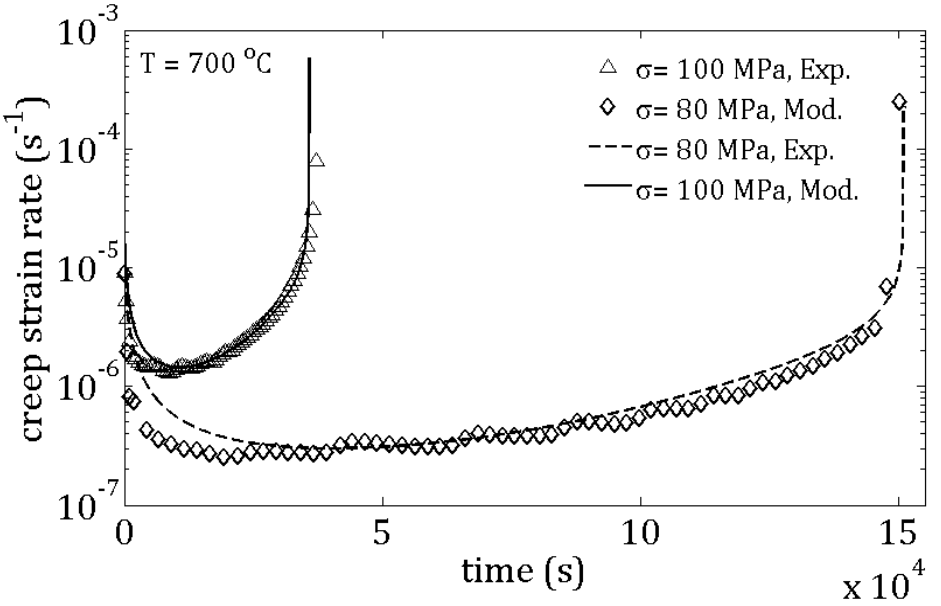

Figure 2-4. Comparison between the model predictions and experimental data for the creep tests at 700 ˚C and stresses of 80 MPa and 100 MPa.

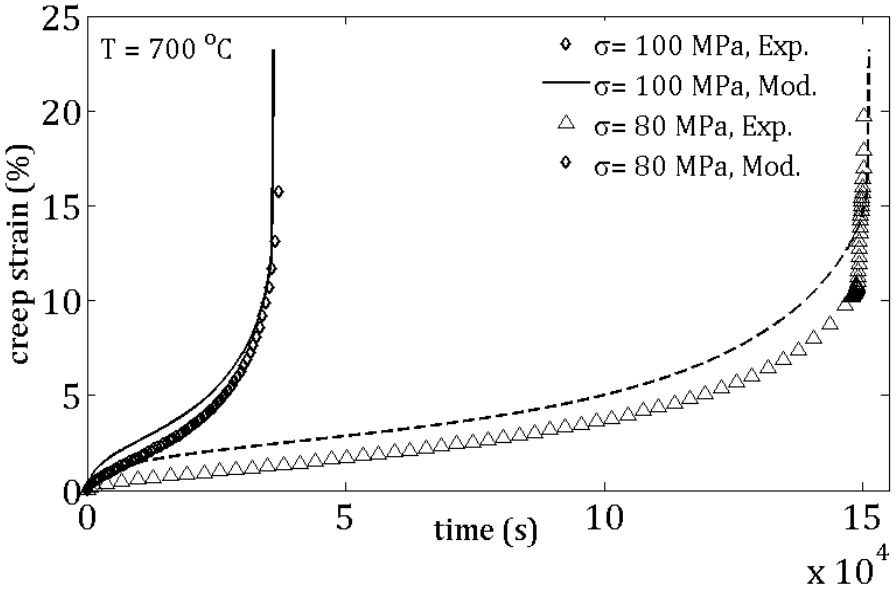

Figure 2-5. Comparison between the model predictions and experimental data for the creep strains at 700 ˚C and stresses of 80 MPa and 100 MPa.

Furthermore, the creep response for the stress levels of 150 MPa and 200 MPa at 700 ˚C was simulated, and the results are shown in Figures 2-6 and 2-7.

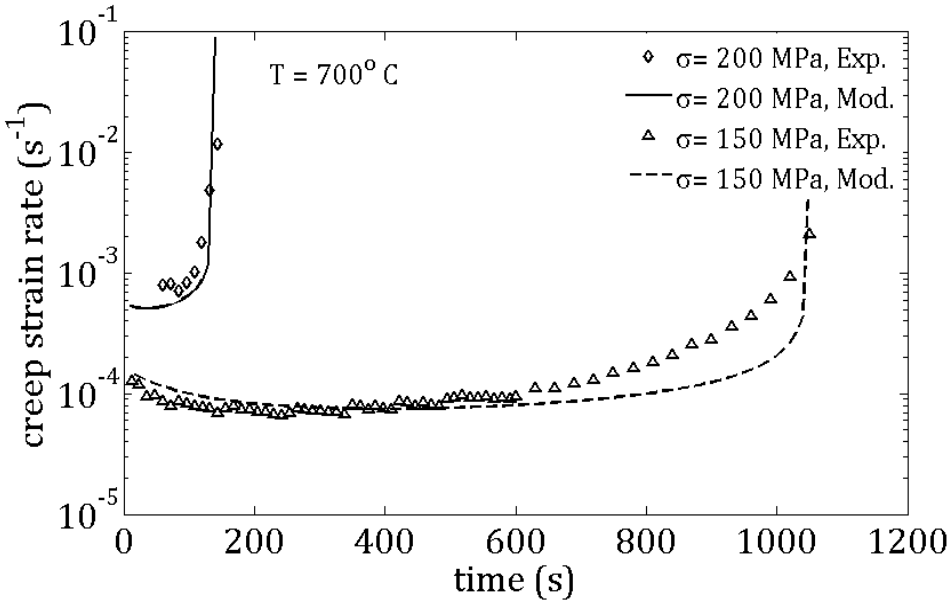

Figure 2-6. Comparison between the model predictions and experimental data for the creep tests at 700 ˚C and stresses of 150 MPa and 200 MPa.

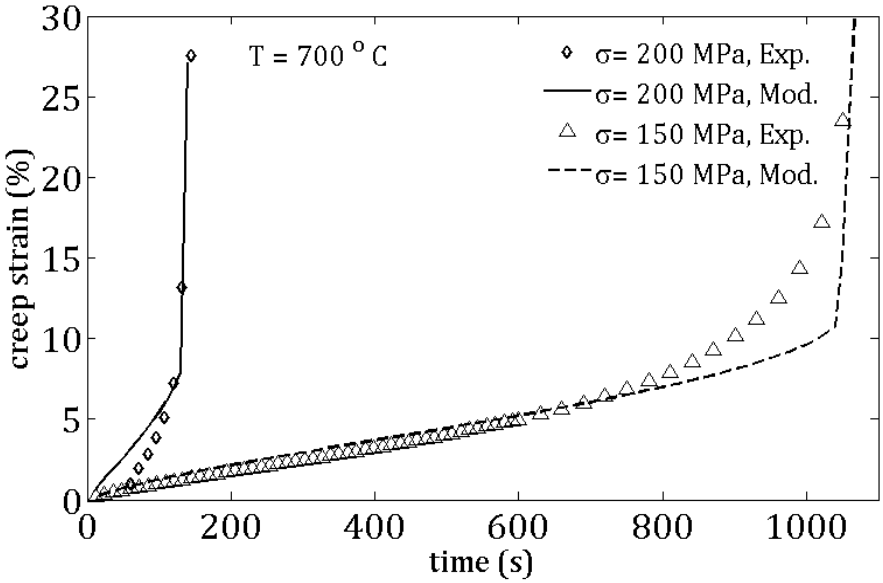

Figure 2-7. Comparison between the model predictions and experimental data for the creep strains at 700 ˚C and stresses of 150 MPa and 200 MPa.

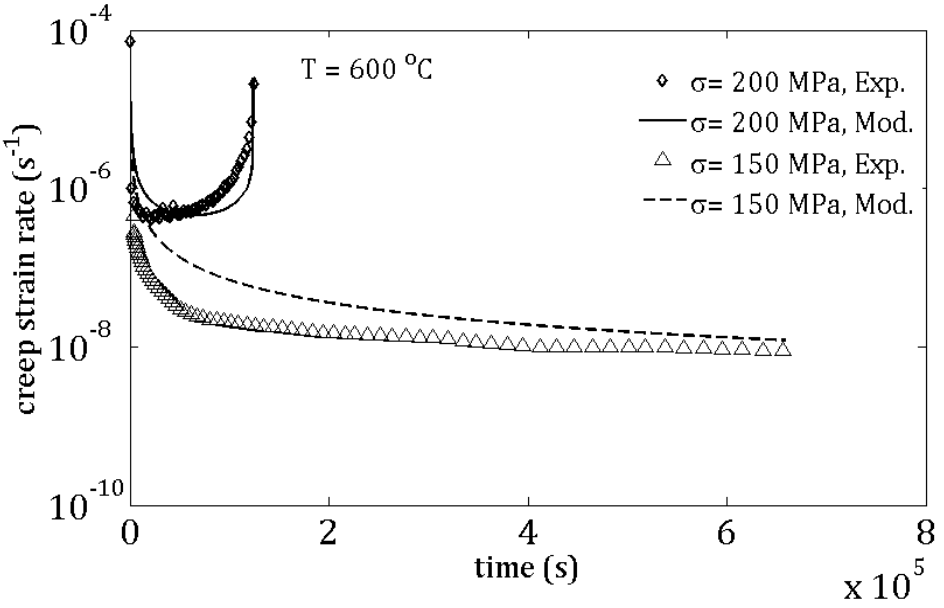

Figure 2-8. Comparison between the model predictions and experimental data for the creep tests at 600 ˚C and stresses of 150 MPa and 200 MPa.

Figures 2-8 and 2-9 show the creep behavior of the material at 600 ˚C and applied stresses of 150 MPa and 200 MPa. The material parameters used in the model are shown in Tables 2-3 and 2-4.

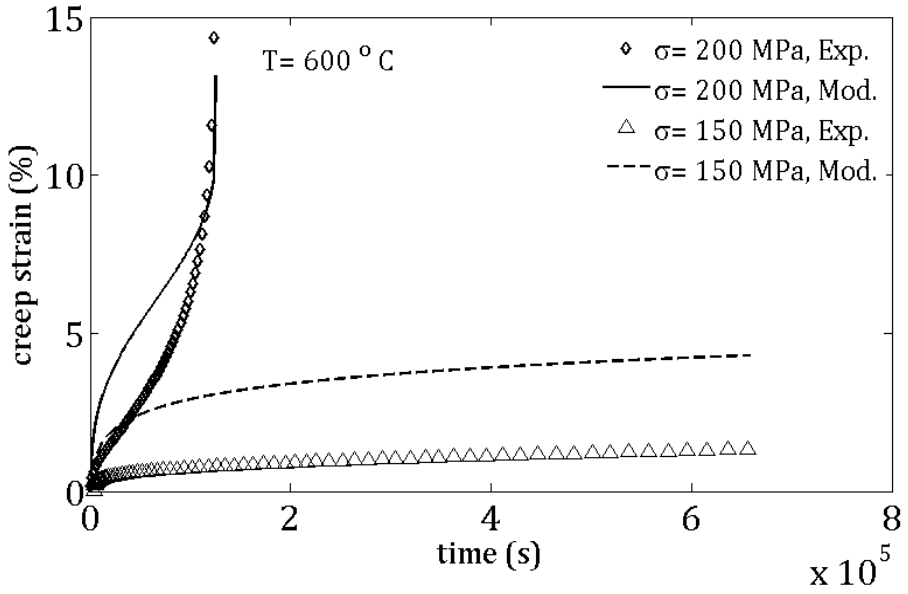

Figure 2-9. Comparison between the model predictions and experimental data for the creep tests at 600 ˚C and stresses of 150 MPa and 200 MPa.

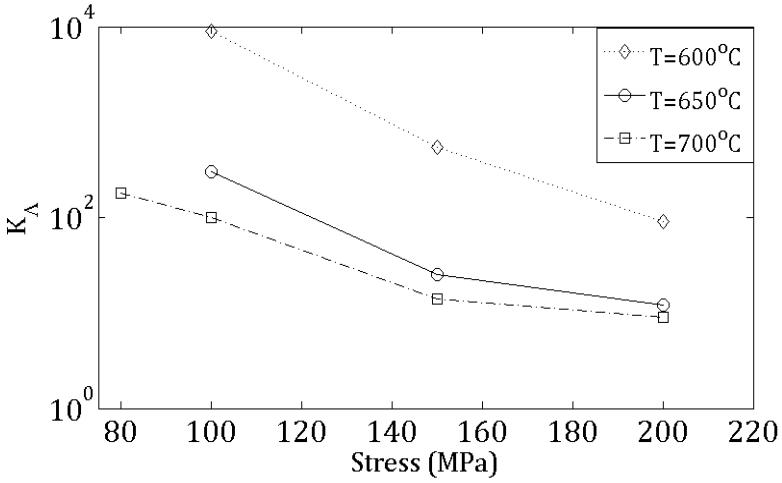

Figure 2-10. Variations of the parameter k_{Λ} with the applied stress at temperatures of 600, 650 and 700 ˚C.

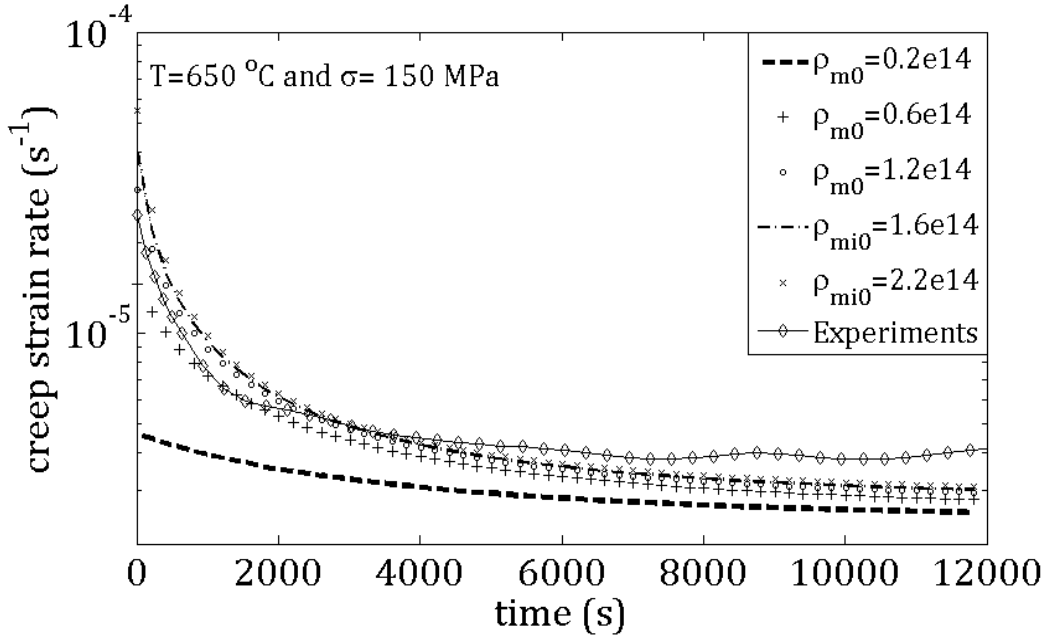

Figure 2-11. Creep strain rate versus time for different values of initial dislocation densities for a creep test simulation at 150 MPa and 650 ˚C.

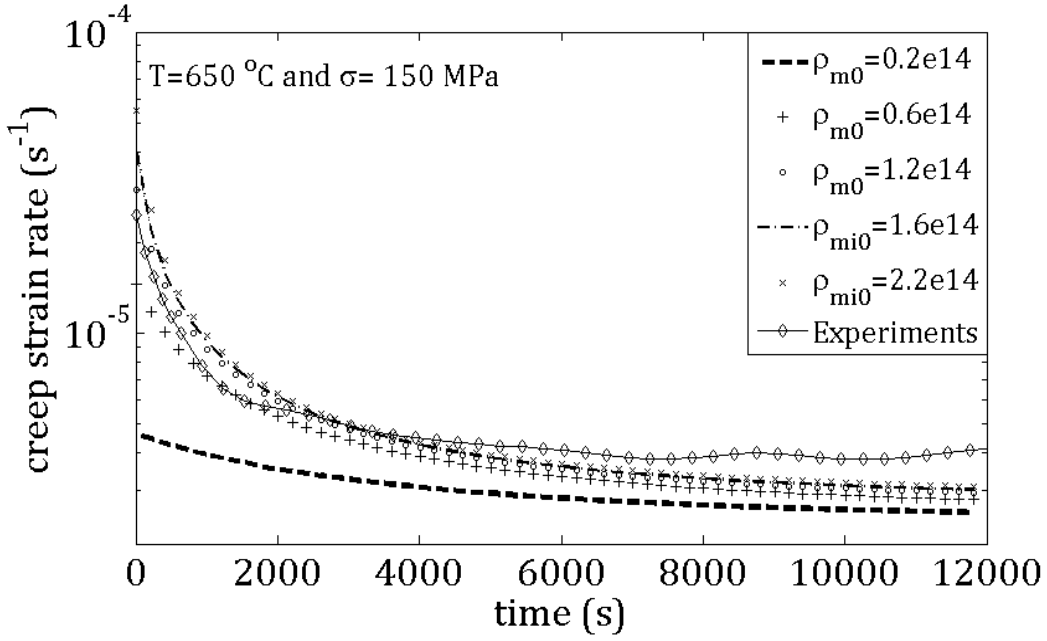

Figure 2-12. Creep strain rate versus time for different values of initial dislocation densities for a creep test simulation at 150 MPa and 700 ˚C.

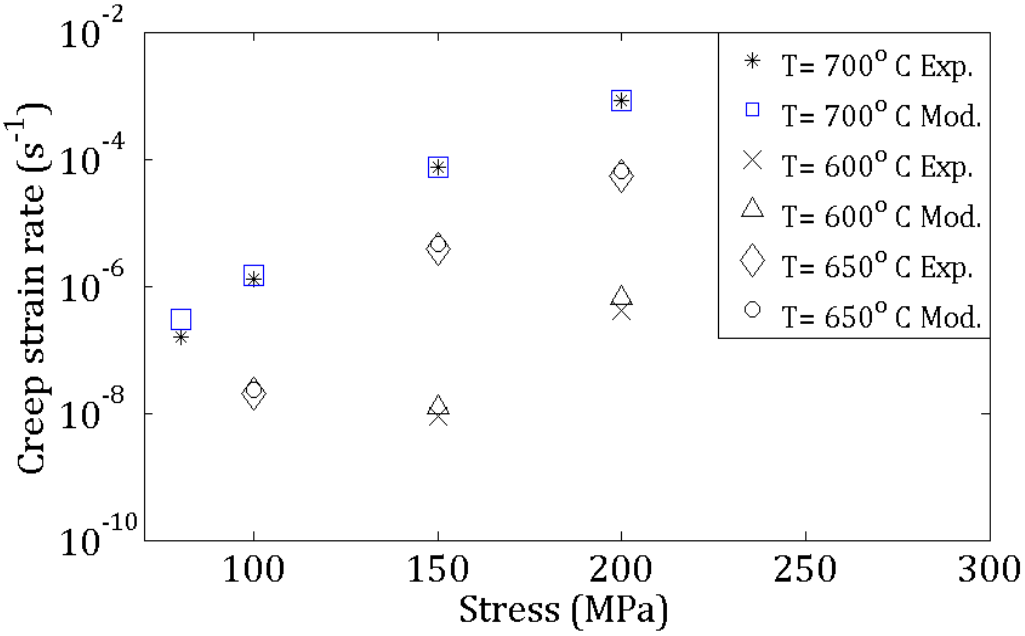

Figure 2-13 Comparison between the model predictions and experimental data for the minimum creep strain rate versus applied stress at temperatures of 600, 650 and 700 ˚C.

Table 2-3. Material parameters for the numerical model.

b (μm)	d_{spon} (μm)	M	n_g	C_0	ε_a	Ω $(\mu m)^3$	α	C	C_{dip}
2.47×10^{-4}	$6b$	3	5	0.056	0.08	b^3	0.02	1.0	0.3

Table 2-4. Damage parameters and the k_A values for the numerical model.

Parameters	σ = 80 MPa	σ = 100 MPa	σ = 150 MPa	σ =200 MPa	Temperatures
		1×10^4	550	90	600 ˚C
k_A		300	25.5	12	650 ˚C
	180	100	14	9	700 ˚C
			5.6×10^{-9}	2.7×10^{-6}	600 ˚C
K_s			5.5×10^{-9}	0.8×10^{-4}	650 ˚C
	0.25×10^{-4}	0.8×10^{-4}	0.8×10^{-4}	0.8×10^{-4}	700 ˚C
			1.9×10^{-6}	1.9×10^{-6}	600 ˚C
K_p			0.2×10^{-6}	0.6×10^{-3}	650 ˚C
	0.1×10^{-5}	0.1×10^{-5}	0.1×10^{-5}	0.1×10^{-5}	700 ˚C
			1	112	600 ˚C
A			47	145	650 ˚C
	57	83	113	146	700 ˚C

As it was mentioned in section 4, in this model k_Λ is considered as an adjustable parameter. The parameter k_Λ has a significant effect in this model for simulating the creep rate for the first and second stage of creep. In order to find the k_Λ values, the simulations have been performed without the damage terms for the steady state creep stage. The values of k_Λ vary with temperature and applied stress. Figure 2-10 shows the variation of k_Λ with the applied stress at different temperatures. At each temperature, by increasing the applied stress the value of k_Λ decreases. A similar conclusion can be drawn for the effect of temperature on the variation of k_Λ. At any stress level, the value of k_Λ will decrease with an increase in temperature. Future studies should focus on the physical relevance of k_Λ. The fitting procedure has been applied to k_Λ in each experiment, but as it was mentioned before, the variation of this parameter is inversely proportional with the increasing stress and temperature, thus it is possible to find an appropriate range with few experimental data available. The second major parameter is the term A in the damage caused by void nucleation and crack formation in Eq. (2-23). This parameter changes proportionally with stress and temperature, and it was fitted to all experimental data. Eq. (2-20) was used to determine K_s values for stress equal to 150 MPa and temperatures of 600 and 650 ˚C. Because of the lack of experimental values for the parameters in Eq. (2-20), the K_s parameter has been fitted to the rest of experiments. The parameter K_p has been fitted to all experiments.

In the present model, dislocation density is a major parameter for computing creep strain rate. The model must be provided with a correct estimate of the initial dislocation density at each stress level, however measuring the dislocation density is not a trivial process. Thus, it

is necessary to evaluate the sensitivity of the model to the initial values of dislocation density, and see how it affects the computed minimum creep rate. The dislocation density in the as-received material is known, and has been reported to be in order of 10^{14} m^{-2} by Fournier et al. (2011), Fournier et al. (2010), and Panait et al. (2010). The variation of the dislocation density is proportional to the second power of the applied stress. As it was mentioned, the dislocation density in current work is divided into mobile and dipole dislocation density. The initial value of dipole dislocation density is usually at least ten times less than that of mobile dislocations. Thus, only the effect of initial mobile dislocation density has been studied in this section.

It is possible to consider a value for the initial dislocation density which best fits the experiments. Based on the value, which has been chosen for the initial dislocation density at each stress level and the k_{Λ} value, the modeling result can be obtained. Figure 2-11 shows the creep strain rate versus time at 650 ˚C and 150 MPa for five different initial mobile dislocation densities at a fixed value of k_{Λ} . The initial mobile dislocation densities are 0.2×10^{14} m^{-2} ,0.6×10^{14} m^{-2}, 1.2×10^{14} m^{-2}, 1.6×10^{14} m^{-2}, and 2.2×10^{14} m^{-2}. As it can be observed, the curves have the same trend. For the initial mobile dislocation density equal to 0.2×10^{14} m^{-2}, the simulation results do not show a satisfactory correlation with the experimental results. For the other initial values, the simulation results are close to the experiments, and this is particularly true for the initial densities of 0.6×10^{14} m^{-2} and 1.2×10^{14} m^{-2}. Figure 2-12 shows the creep strain rate versus time at 700 ˚C and stress level of 150 MPa for different initial dislocation densities. Except for initial values equal to 0.2×10^{14} m^{-2} and 0.6×10^{14} m^{-2}, the simulation results are in good agreement with the experiments. Simulations have also been performed to investigate the effect of initial mobile dislocation densities for other loading cases. It can be concluded that the initial dislocation density has a significant effect on the simulation results,

but it is not necessary to determine the exact value in order to produce good correlations with the experimental data. If an initial value is chosen in a domain near the dislocation density of the as-received material, the simulation results will converge to the same value.

In general, there are two different approaches to modeling creep behavior of materials. One is to simulate the three stages of the creep curve and the other is to evaluate the minimum creep rate. The advantage of the current model is that it makes both possible. In order to simplify the computing of the minimum creep rate, the model has the potential of turning all the damage terms off and predicting the minimum creep rate. Figure 2-13 shows the minimum creep rates computed by the model and the comparison with experiments. In this figure, the minimum creep rate of the material at temperatures of 600, 650 and 700 ˚C and stresses of 80, 100, 150 and 200 MPa without considering the damage terms are shown. The model shows a good agreement with the experimental data.

2.6 Conclusions

This study addressed the creep behavior of the modified 9Cr-1Mo steel. By combining continuum damage terms with the Orowan's equation for creep deformation, a microstructure based model was developed. Viscous glide was considered as the main mechanism of deformation in the power-law creep region. A material parameter k_Λ in the formulation of mobile dislocation generation was considered as the only an adjustable constant, varying with both temperature and applied stress.

During creep deformation the material microstructure will degrade. The main microstructural degradations occurring in modified 9Cr-1Mo are coarsening of $M_{23}C_6$

precipitates, solid solution depletion and void and crack formation. In order to simulate the tertiary creep stage, the effect of these phenomena should be taken into account. A damage term has been defined for these microstructural changes. Three stages of creep deformation have been simulated utilizing the current model. Simulation results were compared with the experimental results for a temperature range of 600-700 ˚C and stress range of 80-200 MPa. The results obtained from the model are in a good agreement with the experimental data. As it was mentioned in this model the subgrain formation, coarsening, and also the grain boundary dislocations was neglected. The k_Λ parameter implicitly represents these effects of the afore-mentioned recovery processes. Future studies should focus on the physical aspects of the k_Λ parameter.

2.7 References

Arzt, E., Wilkinson, D.S., 1986. Threshold stresses for dislocation climb over hard particles: The effect of an attractive interaction. Acta Metallurgica 34(10), 1893-1898.

Besson, J. et al. 2009. Analysis of creep lifetime of a ASME Grade 91 welded pipe. Engineering Fracture Mechanics 76(10), 1460-1473.

Blum, W., Eisenlohr, P., 2009. Dislocation mechanics of creep. Materials Science and Engineering A 510-511, 7-13.

Blum, W., Eisenlohr, P., Breutinger, F., 2002. Understanding creep - a review. Metallurgical and Materials Transactions A 33, 291-303.

Böck, N., Kager, F., 2005. Finite element simulation of the creep behaviour of 9% chromium steels based on micromechanical considerations. Materials Science & Technology 2005 Conference and Exhibition, Pittsburgh, PA, USA, 25-28 September 2005, 149-158.

Chilukuru, H., Durst, K., Wadekar, S., Schwienheer, M.,Scholz, A., Berger, C., Mayer, K.H., Blum, W., 2009. Coarsening of precipitates and degradation of creep resistance in tempered martensite steels. Materials Science and Engineering A 510-511, 81-87.

Courtney, T. H., 2000. Mechanical Behavior of Materials. McGraw-Hill series in material science and engineering, USA.

Ennis, P. J., Zielinska-Lipiec, A., Wachter, O., Czyrska-Filemonowicz, A., 1997. Microstructural stability and creep rupture strength of the martensitic steel P92 for advanced power plant. Acta Materialia 45, 4901-4907.

Fischer, F.D., Svoboda, J., 2011. Chemically and mechanically driven creep due to generation and annihilation of vacancies with non-ideal sources and sinks. International Journal of Plasticity 27(9): 1384-1390.

Fischer, F.D. et al., 1995. “Note on calibration of ductile failure damage indicators.” International Journal of Fracture 73(4): 345–357.

Fournier, B., Sauzay, M., Pineau, A. 2011. Micromechanical model of the high temperature cyclic behaviour of 9-12%Cr martensitic steels. International Journal of Plasticity 27, 1803-1816.

Fujimitsu, M., 2006. Creep degradation in welds of Mod.9Cr-1Mo steel. International Journal of Pressure Vessels and Piping 83(11-12): 819-825.

Gaffard, V., Gourgues-Lorenzon, A.F., Besson, J., 2005. High temperature creep flow and damage properties of 9Cr1MoNbV steels: Base metal and weldment. Nuclear Engineering and Design 235(24), 2547-2562.

Ghoniem, N.M., Matthews, J.R., Amodeo, R.J., 1990. Dislocation model for creep in engineering materials. Res Mechanica 29, 197-219.

Horstemeyer, M. F., Bammann, D. J., 2010. Historical review of internal state variable theory for inelasticity. *International Journal of Plasticity* 26(9): 1310-1334.

Haney, E. M., Dalle, F., Sauzay, M., Vincent, L., Tournié, I., Allais, L., Fournier, B., 2009. Macroscopic results of long-term creep on a modified 9Cr–1Mo steel (T91). Materials Science and Engineering A 510-511, 99-103.

Hollner S., Fournier B., Le Pendu J., Cozzika T., Tournié I., Brachet J. C., Pineau A., 2010. High-temperature mechanical properties improvement on modified 9Cr–1Mo martensitic steel through thermomechanical treatments. Journal of Nuclear Materials 405, 101-108.

Kabadwal, A., Tamura, M., Shinozuka, K., Esaka, H., 2010. Recovery and precipitate analysis of 9 Pct Cr-1 Pct MoVNb steel during creep. Metallurgical and Materials Transactions A 41, 364-379.

Kadoya, Y., Nishimura, N., Dyson, B. F., McLean, M., 1997. In: Earthman, J. C., and Mohamed, F. A., (Eds.) Proceeding of Creep and Fracture of Engineering Materials & Structures, The Minerals, Metals & Materials Society 1997, Warrendale, PA, United states, 343–352.

Klueh, R. L., Harris, R., 2001. High-Chromium Ferritic and Martensitic Steels for Nuclear Applications. ASTM, West Conshohocken, PA, USA.

Lee, Jae Seung et al. 2006. Causes of breakdown of creep strength in 9Cr–1.8W–0.5Mo–VNb steel. Materials Science and Engineering *A* 428(1–2), 270-275.

Masuyama, F., 2006. Creep degradation in welds of Mod.9Cr-1Mo steel. International Journal of Pressure Vessels and Piping 83, 819–825.

McLean, M., Dyson, B. F., 2000. Modeling the effects of damage and microstructural evolution on the creep behavior of engineering alloys. Journal of Engineering Materials and Technology 122, 73-278.

Miannay, D. P., 2001. Time-Dependent Fracture Mechanics. Springer, New York, USA.

Morra, P.V. et al. 2009. Precipitate coarsening-induced plasticity: Low temperature creep behaviour of tempered SAE 52100. International Journal of Plasticity 25(12): 2331-2348.

Muñoz-Morris, M.A., Gutierrez-Urrutia, I., Morris, D. G., 2009. Influence of nanoprecipitates on the creep strength and ductility of a Fe–Ni–Al alloy. International Journal of Plasticity 25(6): 1011-1023.

Nakajima, T., Spigarelli, S., Evangelista, E., Endo, T. 2003. Strain Enhanced Growth of Precipitates during Creep of T91. Materials Transactions 44, 1802-1808.

Oberson, P.G., Ankem S., 2009. The effect of time-dependent twinning on low temperature ($<0.25 * Tm$) creep of an alpha-titanium alloy. International Journal of Plasticity 25(5): 881-900.

Panait, C. G., Zielińska-Lipieca, A. Z., Koziel, T., Czyrska-Filemonowicza, A., Gourgues-Lorenzonb, A. F., Bendickd, W., 2010. Evolution of dislocation density, size of subgrains and MX-type precipitates in a P91 steel during creep and during thermal

ageing at 600 ◦ C for more than 100,000 h. Materials Science and Engineering A 527, 4062–4069.

Poirier, J. P., 1985. Creep of Crystals. Cambridge: Cambridge: High-Temperature Deformation Processes in Metals, Ceramics, and Minerals, Cambridge University Press, Cambridge.

Preußner, J. et al. 2009. A Dislocation Density Based Material Model to Simulate the Anisotropic Creep Behavior of Single-Phase and Two-Phase Single Crystals. International Journal of Plasticity 25(5): 973-994.

Raj, S. V., 2002. Power-law and exponential creep in class M materials: Discrepancies in experimental observations and implications for creep modeling. Materials Science and Engineering A 322, 132-147.

Raj, S. V., Iskovitz, Ilana, S., Freed, A., 1995. Modeling the role of dislocation substructure during class M and exponential creep. In: Unified Constitutive Laws of Plastic Deformation. Academic Press, San Diego, CA, USA, 343–439.

Semba, H., Dyson, B. F., Mclean, M., 2005. Microstructural based creep modeling of a 9%Cr Martensitic steel. In: Shibli I. A., Holdsworth S. R., Merkling, G. (Eds.) Proceeding of Creep and Fracture in High Temperature Components-Design and Life Assessment, 12-14 September 2005, London, UK, DEStech Publications Lancaster, PA, USA, 419–27.

Shrestha T., et al. 2012. Creep deformation mechanisms in modified 9Cr–1Mo steel. Journal of Nuclear Materials 423, 110-119.

Sklenička, V., Kuchařová, K., Svoboda, M., Kloc, L., Burši, J., Kroupa K. A., 2003. Long-term creep behavior of 9–12 Cr power plant steels. Materials Characterization 51, 35-48.

Sklenička, V., Kuchařová, K., Dlouh, S, A., Krejci, J., 1994. Creep behaviour and microstructure of a 9%Cr steel In: Coutsouradis, D. Davidson, J. H., Ewald, J.,

Greenfield, P. (Eds.) Proceedings of the Conference on Materials for Advanced Power Engineering, Kluwer Academic Publishing, Dordrecht, Netherlands, 435–444.

Spigarelli, S., Kloc, L., Bontempi, P., 1997. Analysis of creep curves in a 9Cr-1Mo modified steel by means of simple constitutive equations. Scripta Materialia 37, 399-404.

Sauzay, M., 2009. Modelling of the evolution of micro-grain misorientations during creep of tempered martensite ferritic steels. Materials Science and Engineering A 510–511, 74-80.

Swindeman, R. W., Santella, M. L., Maziasz, P. J., Robertsb , B. W., Coleman , k., 2004. Issues in replacing Cr–Mo steels and stainless steels with 9Cr–1Mo–V steel term. International Journal of Pressure Vessels and Piping 81, 507-512.

Terada, D., Yoshida, F., Nakashima, H., Abe, H., & Kadoya, Y., 2002. In-situ Observation of Dislocation Motion and Its Mobility in Fe–Mo and Fe–W Solid Solutions at High Temperatures. ISIJ International 42, 1546-1552

Venkataramani, G., Kirane, K., Ghosh, S., 2008. Microstructural parameters affecting creep induced load shedding in Ti-6242 by a size dependent crystal plasticity FE model. *International Journal of Plasticity* 24(3): 428-454.

Viswanathan, R. 1989. Damage mechanisms and life assessment of high-temperature components. ASM International, Ohio, USA.

Yin, Y. F., Faulkner, R. G., 2008. Creep life predictions in 9% Cr Ferritic steels. In: Proceeding of International Conference on New Developments on Metallurgy and Applications of High Strength Steels (TMS). Buenos Aires, Argentina 2008, 283-296.

Chapter 3 - Creep Damage Analysis in Welded Joints of Modified 9Cr-1Mo Steel using a forward explicit scheme

"Creep Damage Analysis in Welded Joints of Modified 9Cr-1Mo Steel."

Transactions of the American Nuclear Society 107, 468, 2012.

3.1 Introduction

Modified 9Cr-1Mo steel is a candidate material for very high-temperature reactor (VHTR) pressure vessels. The material microstructure degrades during the welding process. Hence the material creep resistance reduces. In this research, a microstructural creep model combined with a continuum damage mechanics model is developed. The evolution of dislocation structure has been considered as the governing creep mechanism in this material. Furthermore, the effect of void growth and crack formation, precipitate coarsening, and solid solution depletion were taken into account by defining continuum damage terms. The numerical model has been implemented in the commercial finite element software ABAQUS by means of a User Material Subroutine (UMAT). The creep behavior of the material was simulated in the heat affected zone (HAZ) and the welded material. Several creep experiments have been conducted on the welded specimens. The tensile creep tests were performed at a temperature range of 550-700 ˚C and stress level of 80-200 MPa. Finally, the simulation results have been compared to the experiments.

The VHTR represents the next generation of high temperature gas-cooled reactors for the future nuclear power plants. The VHTR is operated at higher pressure and temperature for longer time period compared with the previous generation of gas cooled reactors. To account

for these operating conditions, it is necessary to consider a high creep resistance material for the reactor structure. Modified 9Cr-1Mo steel is a suitable candidate for VHTR pressure vessels. Although 9Cr-1Mo steel has a good creep resistance, the material microstructure degrades during the welding process. Hence, investigating the creep resistance welded 9Cr-1Mo steel is crucial.

In the previous chapter, a microstructural creep model combined with a continuum damage mechanics model was developed by (Basirat et al. 2012a). The evolution of dislocation structure was considered as the governing creep mechanism in this material. Furthermore, the effects of void growth and crack formation, precipitate coarsening, and solid solution depletion were taken into account by defining continuum damage terms. However, in that study the model was successfully applied only to specimens made of the base metal (BM) of 9Cr-1Mo, and the model was one-dimensional (1-D). Nevertheless, any comprehensive model should be applicable to three-dimensional (3-D) geometries. Moreover, once a 3-D model is developed, it should be tested for various loading cases in different structures. Therefore, the objective of this study was to develop a 3-D micromechanical creep damage model to predict the creep life of the welded joints of modified 9Cr-1Mo steel. Our hypothesis was that the 3-D model could predict the creep behavior of welded specimens of the modified 9Cr-1Mo steel.

3.2 Modeling and Experiments

Creep mechanism in crystalline materials is generally governed by dislocation glide and climb. Blum et al. (2002) proposed a model for the viscous glide of dislocations during creep deformations. In this model, Orowan's creep equation was employed to compute the creep strain rate. Orowan's equation related the creep strain rate caused by dislocation motion,

to the density of mobile dislocations, Burgers vector, and the glide velocity of these dislocations.

The depletion of Mo particles in the subgrain matrix under long term thermo-mechanical loading decreases the creep resistance. Moreover, the precipitate coarsening ($M_{23}C_6$ and MX) in modified 9Cr-1Mo increases the interparticle spacing between the precipitates. Precipitate coarsening leads to dislocations enhancing their mobility. Consequently, dislocations require less energy to climb over precipitates (Chilukuru et al. 2009). Furthermore, void nucleation and crack formation is one of the most important creep damage mechanisms in 9Cr-1Mo steel. The cavities usually nucleate at triple junctions or at particles located on grain boundaries. Grain deformation and cavity coalescence are the main crack formation mechanisms in 9Cr-1Mo. The Orowan's equation was modified in order to consider the effects of several material degradation mechanisms in the following format,

$$\dot{\bar{\varepsilon}}_{cr} = \frac{b \,.\, \rho_m \,.\, V_g}{M(1-D_s)(1-D_P)(1-D_N)}, \qquad (3\text{-}1)$$

where $\dot{\bar{\varepsilon}}_{cr}$ the effective creep strain rate, b is the Burgers vector, M is the Taylor factor, V_g is the glide velocity and ρ_m is the density of the mobile dislocations. Furthermore, D_s represents the damage caused by solid solution depletion, D_P is the damage caused by precipitate particle coarsening, and D_N is the damage induced by void nucleation and crack formation. The constitutive equations which have been used to derive the above equation have been described elsewhere (Basirat et al. 2012a).

In order to achieve our objectives, the previously developed 1-D numerical model was implemented in ABAQUS utilizing the following equations by writing a UMAT.

$$\dot{\varepsilon}_{ij}^{cr} = \lambda S_{ij} \tag{3-2}$$

$$\lambda = \frac{3}{2}\frac{\dot{\bar{\varepsilon}}_{cr}}{\sigma_{eq}} \tag{3-3}$$

where S_{ij} represents the components of the deviatoric stress tensor, and σ_{eq} is the von Misses stress, and λ is the factor of proportionality. Substituting Eq. (3-1) into Eq. (3-3) and inserting in Eq. (3-2) the creep strain rate tensor components will be

$$\dot{\varepsilon}_{ij}^{cr} = \frac{3S_{ij}}{2\sigma_{eq}} \frac{b \,.\, \rho_m \,.\, V_g}{M(1-D_s)(1-D_P)(1-D_N)} . \tag{3-4}$$

To implement the above equations in ABAQUS, a forward Euler explicit integration scheme was used. Furthermore, the elastic stiffness matrix was used for the material Jacobian.

In the present work, creep tests were performed on welded specimens with a round cross-section. The specimen gauge length was 45 mm with a diameter of 6.35 mm. A Post-Weld Heat Treatment (PWHT) was conducted on the specimens. They were tempered at 750 ˚C for two hours. Figure 3-1 shows the Vickers hardness profile across the length of as-welded and the PWHT specimens.

In order to perform a finite element analysis over the welded material it is necessary to perform the material characterization of the specimen. In general, it is acceptable to divide the specimen in three regions, the BM, the heat affected zone (HAZ) and the weld metal (WM). Although the HAZ microstructure changes gradually from the WM vicinity to BM, in this study, for simplicity the HAZ was considered as one homogeneous part. Gaffard, et al. (2009) showed that the WM and BM demonstrate similar steady state creep behaviors. Hence, same material properties were considered for BM and the WM.

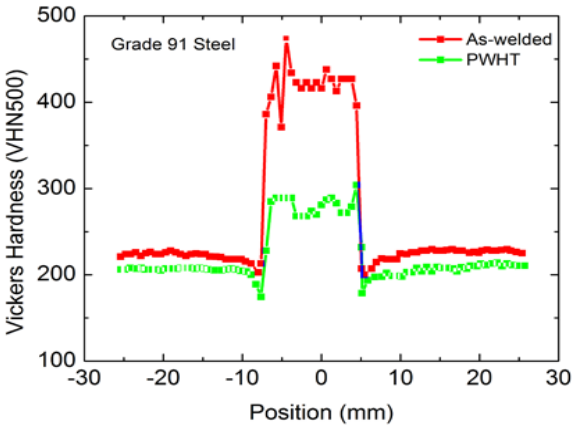

Figure 3-1. Hardness profile across the as-welded and PWHT specimens made of 9Cr-1Mo steel.

Simulations were performed on a simplified model with two materials, the BM and HAZ (Gaffard, et al. 2005; Besson et al. 2009). Consequently, the steady state creep rate in the material is computed in the following form

$$l_T \dot{\varepsilon}_{ss} = l_{HAZ} \dot{\varepsilon}_{HAZ} + l_{BM} \dot{\varepsilon}_{BM} \qquad (3\text{-}5)$$

where, $\dot{\varepsilon}_{ss}$, and $\dot{\varepsilon}_{BM}$ are represent the steady state creep rate of the welded specimen in the HAZ and BM. For the specimens used in this study, l_T is the total gauge length of the specimen measured at 45 mm, l_{HAZ} is the HAZ length which was measured at 6 mm, and l_{BM} is the total length of the BM and the WM.

3.3 Results and Conclusions

The tensile creep tests were performed at a temperature range of 550-700 ˚C and a stress level of 80-200 MPa on the BM and welded specimens. The creep behavior of the material was simulated in both the HAZ and BM in the ABAQUS model. The simulation results were compared to experiments data. Figure 3-2 shows the comparison between the

model predictions and experimental data for the welded specimen in a creep test performed at 150 MPa and 650 ˚C. The model was able to make a good prediction of creep behavior across these experiments.

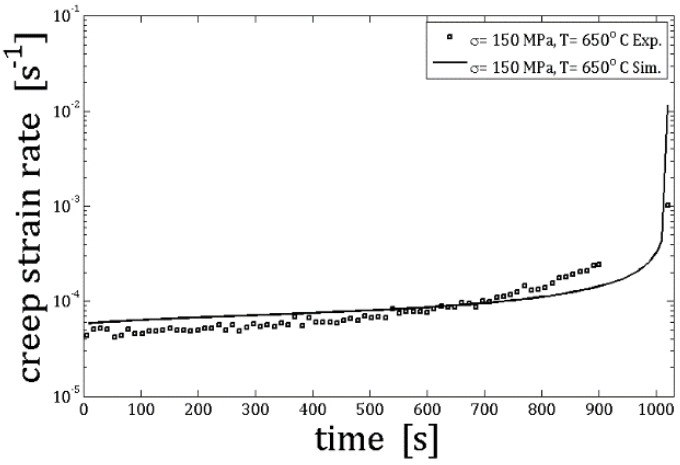

Figure 3-2 FEA simulation and experimental results for a creep test at 150 MPa and 650 ˚C

3.4 References

Basirat, M. et al. 2012a. "A Study of the Creep Behavior of Modified 9Cr-1Mo Steel Using Continuum-Damage Modeling." International Journal of Plasticity 37: 95–107.

Blum, W., P. Eisenlohr, and F. Breutinger. 2002. "Understanding Creep—a Review." Metallurgical and Materials Transactions A 33(2): 291–303.

Besson, J., S. Leclercq, V. Gaffard, and A. F. Gourgues-Lorenzon. 2009. "Analysis of Creep Lifetime of a ASME Grade 91 Welded Pipe." Engineering Fracture Mechanics 76(10):1460–73.

Chilukuru, H. et al. 2009. "Coarsening of Precipitates and Degradation of Creep Resistance in Tempered Martensite Steels." Materials Science and Engineering: A 510: 81–87.

Gaffard, V., A.F. Gourgues-Lorenzon, and J. Besson. 2005. “High Temperature Creep Flow and Damage Properties of 9Cr1MoNbV Steels: Base Metal and Weldment.” Nuclear Engineering and Design 235(24): 2547–62.

Lemaître, J. 1990. Mechanics of Solid Materials. Cambridge: Cambridge University Press.

Chapter 4 - A Creep Damage Model for High-Temperature Deformation and Failure of 9Cr-1Mo Steel Weldments

"A Creep Damage Model for High-Temperature Deformation and Failure of 9Cr-1Mo Steel Weldments." *Metals 5 (3), 1487-1506, 2015.*

4.1 Introduction

Creep failure has always been a concern when designing high-temperature components and structures in coal-fired, gas-fired or nuclear power plants. The Very High Temperature Reactor (VHTR) represents the next generation of high-temperature gas-cooled nuclear reactors. VHTRs operate at the temperature range of 450-550° C and pressures of 5-9 MPa. The target for the design life of the VHTR is 60+ years, and its size is almost twice as large as that of the current gas-cooled reactors. In order to satisfy the design conditions, it is necessary to employ heat and radiation resistant materials for the manufacturing of the reactor pressure vessel. Manufacturing such a large pressure vessel would involve on-site ring forging and welding. During welding, the material is exposed to high-temperatures which may result in the local degradation of the microstructure. One potential material for such use is modified 9Cr-1Mo steel. Although 9Cr-1Mo steel exhibits excellent heat resistance, it may undergo microstructural degradation during the welding process. Moreover, during service the material would experience elevated temperatures and stresses (Shrestha et al., 2012). Therefore, for applications such as pressure vessels for VHTRs, it is crucial to investigate the creep resistance of 9Cr-1Mo steel welded joints, and to develop robust computational models capable of predicting the creep and fracture behavior over the range of temperatures and stresses of

interest. The creep behavior of welded joints of 9Cr-1Mo steel has been previously studied by several authors (Auerkari et al. 2007; Besson et al. 2009; Gaffard, Gourgues-Lorenzon, and Besson 2005; Hyde, Saber, and Sun 2010; Hyde and Tang 1998; Laha et al. 2009; Spigarelli and Quadrini 2002; Watanabe et al. 2006; Yaghi et al. 2008; Yaguchi, Ogata, and Sakai 2010), however there is still a need for a physics-based computational model capable of predicting the creep life of welded joints over long and short service periods. Dislocations restructuring is the main mechanism that drives creep deformation in modified 9Cr-1Mo steel. Dislocation restructuring results from dislocation and dipole generation and annihilation, as well as dislocation glide and climb. The macroscopic effect of these microstructural changes is the resulting creep strain. In addition to deformation related to changes in dislocation density, other degradation phenomena leading to creep in 9Cr-1Mo steel include microstructural changes of solid solutions, precipitates, grain boundaries, and subgrains. For example, the depletion of Mo particles in the subgrain matrix under long-term thermo-mechanical loading decreases the creep resistance of the steel. Moreover, $M_{23}C_6$ and MX precipitates coarsening increases the spacing between precipitates, leading to enhanced dislocation mobility. Consequently, dislocations require less energy to climb over precipitates. Void/crack nucleation and growth is one of the most important damage mechanisms in 9Cr-1Mo steel. Cavities usually nucleate at triple junctions or at particles located at grain boundaries. Grain deformation and cavity coalescence are the main crack formation mechanism in 9Cr-1Mo (Gaffard et al. 2005; Igari et al. 2011; Lee et al. 2010). The primary goal of this paper is to propose a unified elastic-viscoplastic constitutive model for the creep and damage evolution in modified 9Cr-1Mo steel, in a format that can be implemented in the finite element method. A microstructural creep model combined with a continuum damage mechanics model was first developed and

presented in (Basirat et al. 2012). However, in that study the model was implemented as a one-dimensional material-point simulator code, and was successfully applied only to homogenous specimens made of the base metal (BM) of modified 9Cr-1Mo. In the present paper, the previous model was modified by considering only the generation and annihilation of dislocations as the driving mechanisms for creep. The authors observed that taking in consideration the dipole dynamics had little influence on the creep strain development. Another motivation of this paper was the need for a numerical model implementable in the finite element method to analyze three-dimensional geometries of non-homogenous materials (i.e. welded specimens) subjected to complicated loading configurations. To achieve these goals, the afore-mentioned model was modified and implemented by means of a semi-implicit integration scheme, suitable for creep simulations. The time integration algorithm was implemented in ABAQUS as a User Material Subroutine (UMAT). In order to check the accuracy and stability of the model, several case studies of elastic-viscoplastic deformations of single element under uniaxial tension loading have been studied. The implemented model was used to predict the creep deformation and fracture of welded joints of modified 9Cr-1Mo steel.

4.2 Constitutive Model

4.2.1 Elasticity and Creep Constitutive Equations

According to the theory of inelastic deformations, the accumulated strain is modeled as the summation of the elastic and creep strains,

$$\varepsilon_{ij} = \varepsilon_{ij}^{el} + \varepsilon_{ij}^{cr}, \tag{4-1}$$

and in the rate form

$$\dot{\varepsilon}_{ij} = \dot{\varepsilon}_{ij}^{el} + \dot{\varepsilon}_{ij}^{cr} \,. \tag{4-2}$$

Here, the creep strain rate is assumed to be a function of equivalent stress, temperature and some internal state variables,

$$\dot{\varepsilon} = \dot{\varepsilon}(\bar{\sigma}, T, \xi), \tag{4-3}$$

where $\bar{\sigma}$ is the equivalent von Mises stress, defined according to the *J2* plasticity theory as

$$\bar{\sigma} = \sqrt{\frac{3}{2} S_{ij} : S_{ij}}, \tag{4-4}$$

and $S_{ij} = \sigma_{ij} - \frac{1}{3}\delta_{ij}\sigma_{kk}$, T represents the temperature, and ξ indicates the internal state variables.

In the present model, internal state variables refer to the dislocation density, solid solutions, precipitate size, and other strengthening mechanisms terms. These strengthening mechanisms induce isotropic hardening in the material (Weber and Anand 1990). The isotropic hardening resistance evolves during a thermally activated deformation process such as creep. In a rate-dependent inelastic deformation, the rate of evolution of the internal variables can also be expressed by the rate of change of the internal state variables. Here, $\dot{\xi}_a$ is defined by some functions q_a dependent on $\bar{\sigma}, T, \xi$ and t. Respectively the evolution of the internal state variables can be defined as

$$\dot{\xi}_a = q_a(\bar{\sigma}, T, \xi, t) \quad . \tag{4-5}$$

As it was mentioned before, the decomposition rule is valid for creep deformations exposure. First the elastic response of the material will be modeled by utilizing the common linear isotropic elastic constitutive model. The widely used equation defining the linear isotropic elasticity of a material is

$$\sigma_{ij} = 2G\varepsilon_{ij}^{el} + \lambda \delta_{ij} \varepsilon_{kk}^{el} \quad , \tag{4-6}$$

where *G* is the shear modulus and λ is Lame's constant.

A continuum creep-damage model was developed previously in (Basirat et al. 2012). A simplified version of the mentioned model has been employed here to analyze the creep behavior of the modified 9Cr-1Mo steel. In the original model the density of the dipole dislocations was considered when computing the creep strain accumulation. By performing numerous simulations on the original model, it was observed that neglecting the dipole dislocations density reduces the number of equations in the model significantly, while it doesn't change the simulation results by any sizeable amount. The literature sources and a detailed description of the governing equations in the constitutive model for creep deformation are presented in (Basirat et al. 2012). Here, a summary of the main governing equations, after some algebra applied to the model equations from (Basirat et al. 2012), is presented.

The creep strain rate in a material can be evaluated by using the Orowan's equation modified for the presence of damage,

$$\dot{\bar{\varepsilon}}^{cr} = \frac{\rho_m b B_{visc}}{M\,D}(\bar{\sigma} - \alpha MCGb\sqrt{\rho_m}) \quad . \tag{4-7}$$

In this equation ρ_m is the mobile dislocation density, B_{visc} is the dislocation mobility term which are the dependent variables and b is the Burger's vector, α is a dislocation interaction constant, M is the Taylor factor, C is the inelastic deformation factor (C was taken 0.2 in this study), which are all independent variables. To simplify notations, the following constant is introduced $K_1 = \alpha MCGb$. In equation (4-7), *D* represents the total damage caused by the cumulative effects of precipitate coarsening, depletion of solid solutions, and void and crack formation. The dislocation mobility term is defined according to (Blum, Eisenlohr, and Breutinger 2002) as

$$B_{visc} = \frac{9\Omega D_{sol} K_B T}{MC_0 G^2 b^7 \varepsilon_a^2 \ln(\frac{r_2}{r_1})} \quad , \tag{4-8}$$

where Ω is the atomic volume (considered here as equal to b^3), K_B is the Boltzmann constant, *T* is the temperature, D_{sol} is the solute atom diffusion coefficient in solvent atoms, C_0 is the solute concentration, r_1 and r_2 are the inner and outer cut-off radii of the dislocation stress field, and ε_a is the relative size misfit between solute and solvent atoms. The rate of evolution of mobile dislocations density is defined as the difference between the rate of generation of mobile dislocations ($\dot{\rho}_{m,gen}$), and the rate of annihilation of mobile dislocations density ($\dot{\rho}_{m,ani}$),

$$\dot{\rho}_m = \dot{\rho}_{m,gen} - \dot{\rho}_{m,ani} \,. \tag{4-9}$$

Based on the results reported in (Basirat et al. 2012), it can be shown that the rate of generation of mobile dislocations can be computed as

$$\dot{\rho}_{m,gen} = \frac{\rho_m B_{visc} \sqrt{\rho_m}}{k_\lambda D} (\bar{\sigma} - K_1 \sqrt{\rho_m}), \tag{4-10}$$

where k_λ is a material parameter that depends on temperature and equivalent stress. Similarly, it can be shown that the rate of annihilation of the mobile dislocations is

$$\dot{\rho}_{m,ani} = \frac{4M \dot{\varepsilon} d_{dip} \rho_m}{b n_g} \,. \tag{4-11}$$

where d_{dip} is the dipole formation distance (Blum et al., 2002). The annihilation rate of mobile dislocations is given by the summation of the densities of dislocations which annihilate spontaneously and that of the dislocations that form dipoles. It is a function of the strain rate, the mobile dislocations density, the Burger's vector, the Taylor factor and the number of active slip planes n_g. Replacing $\dot{\varepsilon}$ in Eq. (4-11) by its value from equation Eq. (4-7), the rate of annihilation of mobile dislocations can be expressed as

$$\dot{\rho}_{m,ani} = \frac{4 d_{dip} \rho^2{}_m B_{visc}}{n_g D} (\bar{\sigma} - K_1 \sqrt{\rho_m}) \,, \tag{4-12}$$

As two mobile dislocations of opposite sign approach each other within a certain distance, d_{dip}, they form dipoles and produce sessile dislocations. d_{dip} is calculated as

$$d_{dip} = \frac{M}{8\pi(1-\nu)}\frac{Gb}{\bar{\sigma}} \quad . \tag{4-13}$$

In this equation, ν is the Poisson's ratio. Replacing d_{dip} in Eq. 4-12, the rate of annihilation of mobile dislocations becomes

$$\dot{\rho}_{m,ani} = \frac{4MbG\rho^2{}_m B_{visc}}{2\pi(1-\nu)n_g D\bar{\sigma}}(\bar{\sigma} - K_1\sqrt{\rho_m}) \, . \tag{4-14}$$

4.2.2 *Damage constitutive equations*

The material microstructure will degrade during high temperature exposure, which means that the strengthening mechanisms will become less effective during creep loading. The main strengthening mechanisms in modified 9Cr-1Mo steel are work hardening, solid solution strengthening, precipitation hardening, and subgrain boundary strengthening. It has been shown by several researchers that Mo atoms in solid solution precipitate to form coarse Laves-phase particles under long term thermo-mechanical loading (Chilukuru et al. 2009; Morra et al. 2009; Muñoz-Morris et al. 2009). Moreover, the precipitate ($M_{23}C_6$ and MX) coarsening in modified 9Cr-1Mo increases the inter-particle spacing between precipitates. Solid solutions depletion and precipitate coarsening increase the dislocations mobility. Consequently, dislocations require less energy to move. Furthermore, void nucleation and crack formation is one of the most important creep damage mechanisms in 9Cr-1Mo steel. The cavities usually nucleate at triple junctions or at particles located on grain boundaries. Grain deformation and cavity coalesce are the main crack formation mechanisms in 9Cr-1Mo steel.

Mo is added to 9Cr-1Mo steel to induce solid solution strengthening. During creep loading, a depletion of Mo particles occurs in the subgrain matrix, leading to the precipitation

of Fe_2Mo Laves phases. It has been shown by experiments that Fe_2Mo precipitates with low volume fraction and larger size could not effectively block dislocations motions during creep. These large size Laves phases (Fe_2Mo) are a source for dislocations absorption, and they are brittle phases. These inopportune properties lead to a reduction of the creep resistance of modified 9Cr-1Mo (Lee et al. 2010).

The following equations show the damage caused by solid solution depletion and its corresponding rate.

$$D_s = 1 - \frac{\bar{C}_t}{C_0}, \tag{4-15}$$

$$\dot{D}_S = K_S D_S^{1/3}(1 - D_S) \tag{4-16}$$

Here D_s is the damage term represented by the solid solution depletion, and is a function of the initial and current solid solution concentrations, C_0 and C_t, respectively K_S is a material constant.

Another important damage mechanism in 9Cr-1Mo steel is caused by the coarsening of $M_{23}C_6$ and MX precipitates. The coarsening of precipitates increases the interparticle spacing, and consequently the easier motion of dislocations (in the case of MX) and enhances recovery, i.e. subgrain coarsening (in case of M23C6), which means less creep resistance. The damage and damage rate, accounting for the precipitate coarsening, are written as

$$D_P = 1 - \frac{P_0}{P_t}, \tag{4-17}$$

$$\dot{D}_p = k_p(1 - D_p)^4, \tag{4-18}$$

where P_0 and P_t are the initial and current size of the precipitates, respectively, and k_P is a material constant.

A leading failure mechanism during creep deformation of modified 9Cr-1Mo is crack incubation and growth. Microstructural stress concentrations are responsible for grain boundary sliding leading to the formation of creep cavities and creep crack formation. Creep crack formation and growth has been extensively studied in the literature (Lemaître 1990). In this paper, a modified Kachanov damage model has been employed for the crack-driven creep damage. Simply, creep damage is expressed as a function of the creep exposure time (*t*), the creep rupture time $t_{rupture}$, and a material constant *B*, which is a function of the applied stress. The rupture time can be obtained from experiments. The dependence of rupture time on the applied stress for the 9Cr-1Mo steel welded specimens tested in this study is shown in Figure 4-1.

The crack-driven damage term is modeled as

$$D_N = 1-(1-\frac{t}{t_{rupture}})^{1/(1+B)}. \qquad (4\text{-}19)$$

To summarize, the total damage in the material caused by solid solution depletion, precipitate coarsening and crack formation is denoted as D, and is defined as

$$D = D(D_S, D_P, D_N) = (1-D_S)(1-D_P)(1-D_N). \qquad (4\text{-}20)$$

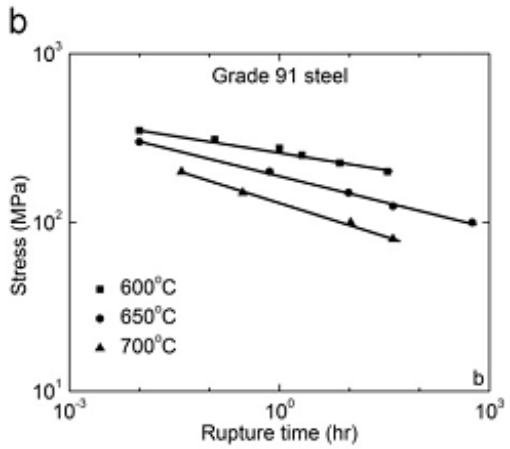

Figure 4-1. True stress versus creep rupture time for modified 9Cr-1Mo 91 steel specimens (Shrestha et al., 2012).

4.3 Numerical Implementation

The analytical model presented in the previous section was implemented in the finite element code ABAQUS Standard as a User Material (UMAT) subroutine. Creep deformation is a history-dependent process. In order to solve the set of governing differential equations for the constitutive model, it is necessary to discretize these equations and integrate them over time.

First, the governing equations for the equivalent stress are presented. The elastic strain at time step *n+1* is calculated from its value at the previous time step *n* and its increment

$$\varepsilon_{ij,n+1}^{el} = \varepsilon_{ij,n}^{el} + (\Delta\varepsilon_{ij}^{tr} - \Delta\varepsilon_{ij}^{cr}) . \quad (4\text{-}21)$$

Replacing Eq. 4-21 in Eq. 4-2 and after some algebra, the stress in the predictor-corrector format can be written as

$$\sigma_{ij} = \sigma_{ij}^{tr} - 2G\Delta\varepsilon_{ij}^{cr} . \quad (4\text{-}22)$$

According to the classical *J2* theory of plasticity, it is possible to express the components of the creep strain rate in the direction of stress as

$$\dot{\varepsilon}_{ij}^{cr} = \lambda S_{ij} = \frac{3}{2}\dot{\bar{\varepsilon}}^{cr}\frac{S_{ij}}{\bar{\sigma}}\ , \tag{4-23}$$

where $\lambda = \frac{3\dot{\bar{\varepsilon}}^{cr}}{2\bar{\sigma}}$ is the creep strain multiplier. Multiplying the above equation by the time increment Δt one obtains

$$\Delta\varepsilon_{ij}^{cr} = \frac{3}{2}\Delta\dot{\bar{\varepsilon}}\frac{S_{ij}}{\bar{\sigma}}\Delta t = \frac{3}{2}\Delta\bar{\varepsilon}^{cr}\frac{S_{ij}}{\bar{\sigma}} = \mathbf{n}\Delta\bar{\varepsilon}^{cr}\ . \tag{4-24}$$

In the above equation, $\mathbf{n}$ is the unit vector normal to the yield surface, and the above equation represents the normality rule. It can be shown that $\mathbf{n} = \frac{3}{2}\frac{S_{ij}}{\bar{\sigma}}$. With some algebra it is possible to rewrite Eq. 4-22 in an equivalent stress format presented by (Dunne 2007)

$$\bar{\sigma} - \bar{\sigma}^{tr} + 3G\Delta\bar{\varepsilon}^{cr} = 0\,. \tag{4-25}$$

The above formula is the governing equation for the equivalent creep stress, while the trial stress σ^{tr} is calculated using Eq. 4-6.

In addition to the creep strain, another state variable considered in this model is the density of mobile dislocations ρ_m. Replacing Eq. 4-10 and Eq. 4-14 in Eq. 4-9, the evolution rate of mobile dislocation density becomes

$$\dot{\rho}_m = g(\bar{\sigma}, \rho_m, D) = \frac{\rho_m B_{visc}(\bar{\sigma} - K_1\sqrt{\rho_m})}{D}\left(\frac{\sqrt{\rho_m}}{K_\Lambda} - \frac{4d_{dip}\rho_m}{n_g}\right). \tag{4-26}$$

In the current model, the integration of the damage term is performed using an explicit scheme. The following equations show the discretized form of Eq. 4-25 and Eq.4-26

$$F(\bar{\sigma}_{n+1}, \rho_{m_{n+1}}, D_n) = \bar{\sigma}_{n+1} - \bar{\sigma}_{n+1}^{Tr} + 3Gf(\bar{\sigma}_{n+1}, \rho_{m_{n+1}}, D_n) = 0\,, \tag{4-27}$$

$$G(\bar{\sigma}_{n+1}, \rho_{m_{n+1}}, D_n) = \rho_{m_{n+1}} - \rho_{m_n} + g(\bar{\sigma}_{n+1}, \rho_{m_{n+1}}, D_n) = 0\,. \tag{4-28}$$

To solve the above system of equations, the Newton-Raphson (N-R) method combined with a line search algorithm was used. The Jacobian matrix needed in the N-R method was computed numerically, however, an analytical form of the Jacobian matrix could also be straightforwardly obtained. At the end of each time step, the damage terms have been explicitly updated. The N-R method gives the increments in equivalent stress and dislocation density

$$\begin{pmatrix} \Delta\bar{\sigma}_{n+1} \\ \Delta\rho_{m_{n+1}} \end{pmatrix} = -\begin{pmatrix} \dfrac{\partial F}{\partial \bar{\sigma}_{n+1}} & \dfrac{\partial F}{\partial \rho_{m_{n+1}}} \\ \dfrac{\partial G}{\partial \bar{\sigma}_{n+1}} & \dfrac{\partial G}{\partial \rho_{m_{n+1}}} \end{pmatrix}^{-1} \begin{pmatrix} F(\bar{\sigma}_n, \rho_m, D_{T_{n-1}}) \\ G(\bar{\sigma}_n, \rho_{m_n}, D_{T_{n-1}}) \end{pmatrix} \tag{4-29}$$

while $\bar{\sigma}_{n+1}$, and $\rho_{m_{n+1}}$ are updated according to $\bar{\sigma}_{n+1} = \bar{\sigma}_n + \Delta\bar{\sigma}_{n+1}$, and $\rho_{m_{n+1}} = \rho_{m_n} + \Delta\rho_{m_{n+1}}$. The total damage *D* at time step *n+1* is updated using Eq. 4-20 in which each of the damage terms D_S, D_P, and D_N are used with their values at step *n+1*. D_S and D_P are updated according to $D_{n+1} = D_n + \dot{D}_n \Delta t$, and D_N is updated according to equation Eq. 4-19. Introducing the updated variables and D_{n+1} in Eq. 4-31, $\dot{\bar{\varepsilon}}^{cr}_{n+1}$ is computed,

$$\dot{\bar{\varepsilon}}^{cr}_{n+1} = f(\bar{\sigma}_{n+1}, \rho_{m_{n+1}}, D_{n+1}) = \frac{\rho_{m_{n+1}} bB_{visc}}{M\, D_n}(\bar{\sigma}_{n+1} - \alpha MCGb\sqrt{\rho_{m_{n+1}}})\,, \tag{4-30}$$

and $\Delta\bar{\varepsilon}^{cr} = \dot{\bar{\varepsilon}}^{cr}_{n+1}\Delta t$. Substituting the equivalent increment of creep strain $\Delta\bar{\varepsilon}^{cr}$ in Eq. 4-23, the components of creep strain tensor are calculated. Once the strain increment and strain tensors components are computed, the stress increment and stress tensor components will be obtained using the following equation

$$\sigma_{ij_{n+1}} = C_{ijkl}(\Delta\varepsilon^{tr}_{kl_{n+1}} - \Delta\varepsilon^{cr}_{kl_{n+1}}) + \sigma_{ij_n} . \quad (4\text{-}31)$$

The updated stress, internal state variables and the tangent stiffness matrix are returned to ABAQUS by the UMAT. The elastic stiffness matrix C_{ijkl} was used to update the tangent stiffness matrix, which is a common approach for finite element simulations of creep deformations (Naumenko 2007).

4.4 **Experiments**

Creep experiments were conducted on welded specimens at temperatures between 550˚C and 700˚C and stress levels between 80 and 200 MPa, by using an Applied Test Systems (ATS) lever arm (20:1) creep tester. Welded specimens were made of ASTM A387 Grade 91 CL2 steel (Grade 91) steel. The specimens were machined out of as-received plates, and were given a round cross-section with a diameter of 12.7 mm and gage length of 45 mm. The chemical composition of Grade 91 steel is indicated in Table 4-1.

The as-received plates were delivered from hot rolled Grade 91, in normalized and tempered condition (i.e., austenitized at 1038 K for 240 minutes, followed by air cooling, and tempered at 789 K for 43 minute). The original dimensions of the as-received Grade 91 plate were 104 mm×104 mm×12.7 mm. The mechanical properties of the material are shown in Table 4-2. In order to machine specimens, the plates were cut into halves and tapered for double

V welding joints, as shown in Figure 4-2. In this figure, Long, Trans, and TT are the longitudinal, the transversal and the through-thickness directions, respectively. The Metrode 2.4 mm diameter 9CrMoV-N TIG filler wire,

Table 4-1. Chemical composition (wt. %) of modified 9Cr-1Mo steel.

Elements	Nominal	Measured
Cr	8.00 - 9.50	8.55
Mo	0.85 - 1.05	0.88
V	0.18 - 0.25	0.21
Nb	0.06 - 0.10	0.08
C	0.08 - 0.12	0.1
Mn	0.30 - 0.60	0.51
Cu	0.4(max.)	0.18
Si	0.20 - 0.50	0.32
N	0.03 - 0.07	0.035
Ni	0.40(max.)	0.15
P	0.02(max.)	0.012
S	0.01(max.)	0.005
Ti	0.01(max.)	0.002
Al	0.02(max.)	0.007
Zr	0.01(max.)	0.001
Fe	Balance	Balance

Table 4-2. Mechanical properties of modified 9Cr-1Mo steel at room temperature.

Yield Strength (MPa)	Tensile Strength (MPa)	Elongation	
		Gage Length (mm)	%
533.60	683.27	50.80	26.0

which is well known for low residual stresses, was used for welding. The plates were preheated at 260°C before welding. To prevent overheating, the steel plates were placed on an aluminum plate during welding. The welding was completed in three successive passes with a current of 130 A and voltage of 15 V. The post-weld heat treatment (PWHT) was conducted at 750°C for 2 hr.

As it was mentioned earlier, the microstructure of the welding heat affected zone will undergo changes due to the temperature gradient during welding. The microstructure of the as-welded and post-weld heat-treated specimens exhibits three different zones, i.e. the unaffected base material, the heat affected zone and the weld material. A typical heat affected zone presents two distinct microstructures: the fine grain heat affected zone (FGHAZ), and the coarse grain heat affected zone (CGHAZ). It has been widely reported that type IV cracks initiate in the HAZ, being caused by the non-uniform structure of the HAZ. The non-uniform

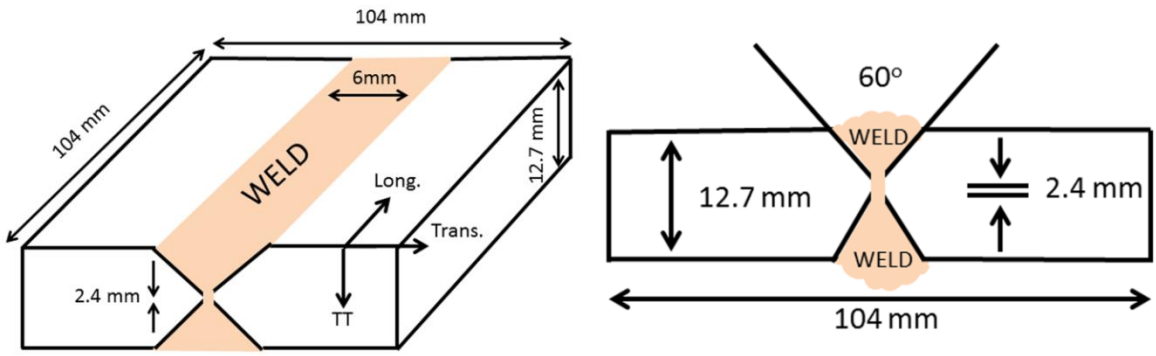

(a)

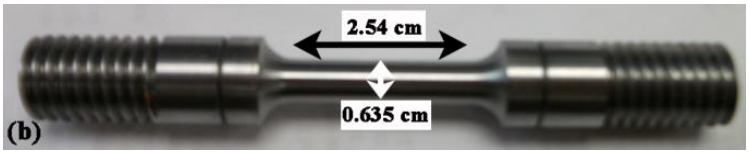

Figure 4-2. (a) Schematic representation of the double V-butt welded plate, and (b) specimen used for creep testing. The specimen is cut from the plate, and the central portion of the specimen matches the weld zone.

structure of HAZ is caused by the partial transformation of austenite into martensite, the presence of retained austenite, the formation of delta-ferrite, and differential migration of interstitial and precipitate forming elements through the heat affected zone which creates a complex microstructure prone to failure.

The hardness of Grade 91 steel in the as-received and PWHT condition has been measured using a Vickers microhardness tester. The hardness of the as-welded material increased across the weld but decreased in the HAZ, as shown in Figure 3a. The as-welded specimen had a maximum hardness of 474 VHN in the weld, while HAZ exhibited the lowest hardness of 200 VHN. The base material had a hardness of approximately 225 VHN. The HAZ was symmetric on either side of the weld. The hardness profile of specimen PWHT at 750^{o}C for 2 hours was similar to that of the as-welded specimen, but the hardness magnitudes were lower.

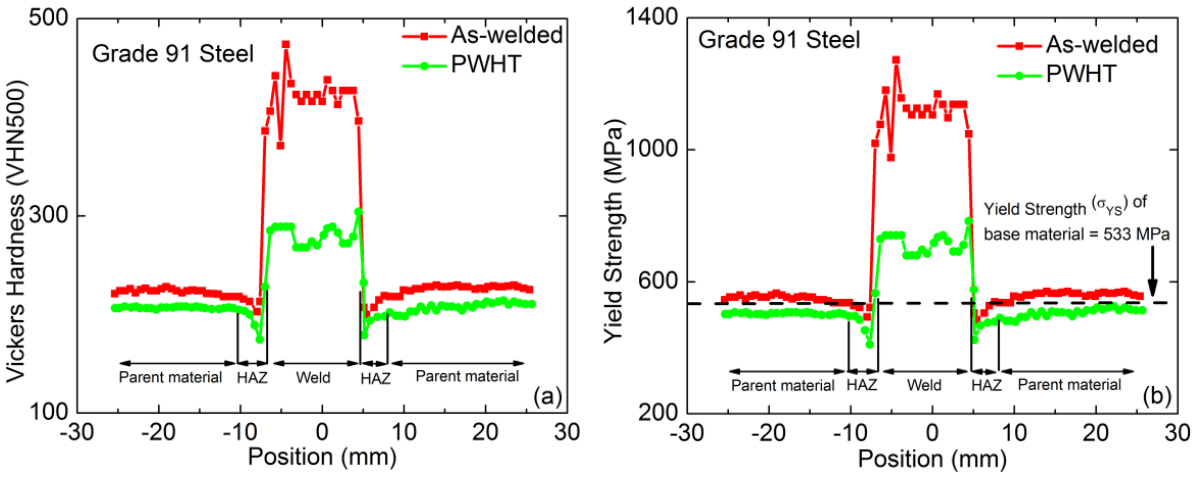

Figure 4-3. Vickers microhardness (a), and yield strength profile (b) of welded Grade 91 steel. Position '0' indicates the center of the weld.

The maximum hardness of 304 VHN was observed in the weld, while the lowest hardness of 174 VHN was observed in the HAZ. The hardness of steels can be correlated with the yield

stress, thus the yield stress profile of the as-welded and PWHT specimens is similar to the hardness profile, as illustrated in Figure 4-3b.

4.5 . Results and Discussion

To perform a finite element analysis on the welded specimen, one needs to obtain accurate material constants in the constitutive model for each distinct region of the specimen. In general, it is reasonable to divide the specimen into four regions, the BM, FGHAZ (HAZ II), CGHAZ (HAZ I) and the welded material (WM). Although the HAZ microstructure changes gradually from the WM to the BM, for simplicity, in this study the HAZ was considered as divided into two separate and homogeneous zones (HAZ I and HAZ II). In (Gaffard et al. 2005) , it was shown that the WM and BM demonstrate similar steady state creep behaviors. Hence, the same material properties were considered for the BM and WM regions in the finite element model. Simulations were performed on a model with three materials, the BM and two HAZ regions. The HAZ segment was divided into HAZ I and HAZ II. Figure 4-4 shows the schematic of each segments of the welded specimen.

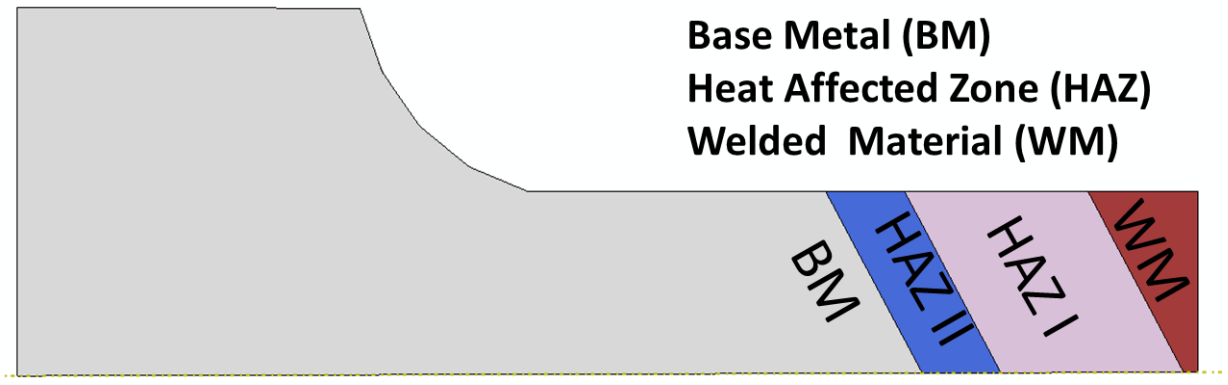

Figure 4-4. Schematic representation of the welded specimen, showing the Base Metal (BM), Heat Affected Zone I and II (HAZ I and II), and the Welded Material (WM).

Given such a configuration of the specimen, the steady state creep rate is computed using the following equation

$$\dot{\varepsilon}_{SS} l_T = l_{BM}\dot{\varepsilon}_{BM} + l_{WM}\dot{\varepsilon}_{WM} + l_{HAZ}\dot{\varepsilon}_{HAZ}, \quad (4\text{-}32)$$

where, $\dot{\varepsilon}_{SS}$, $\dot{\varepsilon}_{BM}$, $\dot{\varepsilon}_{WM}$ and $\dot{\varepsilon}_{HAZ}$ are the steady state creep strain rates of the welded specimen SS, BM, WM, and HAZ, respectively. l_T (=45 mm) is the total gage length of the specimen, l_{BM}, l_{WM} ($l_{BM} + l_{WM}$ = 39 mm) represent the length of BM, WM zones, and l_{HAZ} (= 6 mm) is the length of HAZ zone. If the steady state creep test data for both welded specimen and BM are available, the material properties for HAZ can be obtained. Considering the same material properties for the steady state creep rate of the welded specimen in the WM and BM, Eq. 4-32 is used to compute the creep developed in the HAZ as

$$\dot{\varepsilon}_{HAZ} = \frac{\dot{\varepsilon}_{SS} l_T - (l_{BM} + l_{WM})\dot{\varepsilon}_{BM}}{l_{HAZ}}. \quad (4\text{-}33)$$

As discussed before, the model requires a number of material constants. Some of them depend on temperature and applied stress, while others are independent of stress and temperature. The material properties independent of the testing conditions are $b = 2.47\times10^{-10}\, m$, $M = 3$, $ng = 5$, $\alpha = .02$, and $C_0 = 0.056$. Two key material parameters for the second stage creep are k_Λ and ρ_m. While it is not straightforward to measure the dislocation density ρ_m, it has been showed by (Basirat et al. 2012) that if the initial dislocation density is in a realistic range (i.e., between 0.2×10^{14} and 2.0×10^{14} m^{-2}), the results will converge to the approximately the same value (Basirat et al. 2012). The values for k_Λ may be determined by

performing simulations for the minimum creep rate in the welded and BM specimens, and by employing Eq. 4-33. Furthermore, $t_{rupture}$ for different loading conditions has been obtained from experiments and illustrated in Figure 4-1. Values for the remaining material constants used in this study are presented in Table 4-3.

To perform predictions at temperatures different than those that have been tested in this study, it is useful to perform curve-fitting of material parameters versus temperature. For exemplification, k_λ is chosen because it is a key material constant in this model. By studying the values of k_λ in Table 4-3, which were obtained from numerical simulations for each specimen microstructure (BM and WM, HAZ I and HAZ II), it is proposed that $\ln(k_\lambda)$ can be modeled as a quadratic function of σ with coefficients a, b, and c dependent on temperature T, namely

$$\ln(k_\lambda) = a(T)\sigma^2 + b(T)\sigma + c(T) \qquad (4\text{-}34)$$

where $a(T)$, $b(T)$, and $c(T)$ are different for each zone of the material and they need to be determined. Three values of k_λ are available at three values of the stress σ at temperatures T = 600˚C and T = 650˚C, and only one value is known at T = 700˚C, due to the available experimental data. The results of fitting $\ln(k_\lambda)$ to a quadratic polynomial for T = 600˚C and T = 650˚C are shown in Figure 4-5a and 4-5b using solid lines, while the symbols represent values from the simulations. Thus, we know $a(T)$, $b(T)$, and $c(T)$ at T = 600˚C and T = 650˚C. To find the coefficients a, b and c at T = 700˚C and describe k_λ as a function of temperature, we assume that a, b and c depend quadratically on T as well, i.e.

$$a(T) = \alpha_2 T^2 + \alpha_1 T + \alpha_0,\ b(T) = \beta_2 T^2 + \beta_1 T + \beta_0,\ c(T) = \gamma_2 T^2 + \gamma_1 T + \gamma_0 \quad (4\text{-}35)$$

Requiring that *a, b* and *c* assume the computed values at T = 600 ˚C and T = 650 ˚C as well as using the table value of k_λ at σ = 100 MPa and T = 700˚C in Eq. 4-34 produces a linear 10 × 12 underdetermined system for unknowns $\alpha_i, \beta_i, \gamma_i$, i = 1; 2; 3 and *a(T), b(T), c(T)* at T = 700˚C. The system was solved in a least squares sense using the truncated singular value decomposition (SVD) method because of ill-conditioning of the coefficient matrix. As an example, in Figure 4-5d coefficient *c* is shown as a quadratic function of *T* for different zones of the welded specimen. It was found that c = 17.366 at T = 700˚C for BM and WM and c = 14.517 for HAZ I and c = 12.414 for HAZ II. Coefficients *a* and *b* are much smaller ($a \sim 10^{-4}$, $a \sim 10^{-1}$) and they can be approximated at T = 700˚C in a similar manner. With *a, b* and *c* known at T = 700˚C, k_λ at T = 700˚C can be reconstructed using Eq. 4-34. The results of such reconstruction for each material are shown with a dashed line in Figure 4-5. These approximated curves provide an excellent agreement with a value of k_λ available at T = 700˚C and σ = 100MPa.

Table 4-3. Material constants used in the constitutive model.

Material	Temperatures	Constant	σ = 100 MPa	σ = 150 MPa	σ =200 MPa
BM & WM	600 ˚C		1×10^4	550	90
HAZ I	650 ˚C	k_λ	300	25.5	12
HAZ II	700 ˚C		100	14	9
	600 ˚C			5.6×10^{-9}	2.7×10^{-6}
HAZ I	650 ˚C	K_s	0.8×10^{-4}	5.5×10^{-9}	0.8×10^{-4}
	700 ˚C			0.8×10^{-4}	0.8×10^{-4}
	600 ˚C			1.9×10^{-6}	1.9×10^{-6}
HAZ II	650 ˚C	K_p	0.1×10^{-5}	0.2×10^{-6}	0.6×10^{-3}
	700 ˚C			0.1×10^{-5}	0.1×10^{-5}

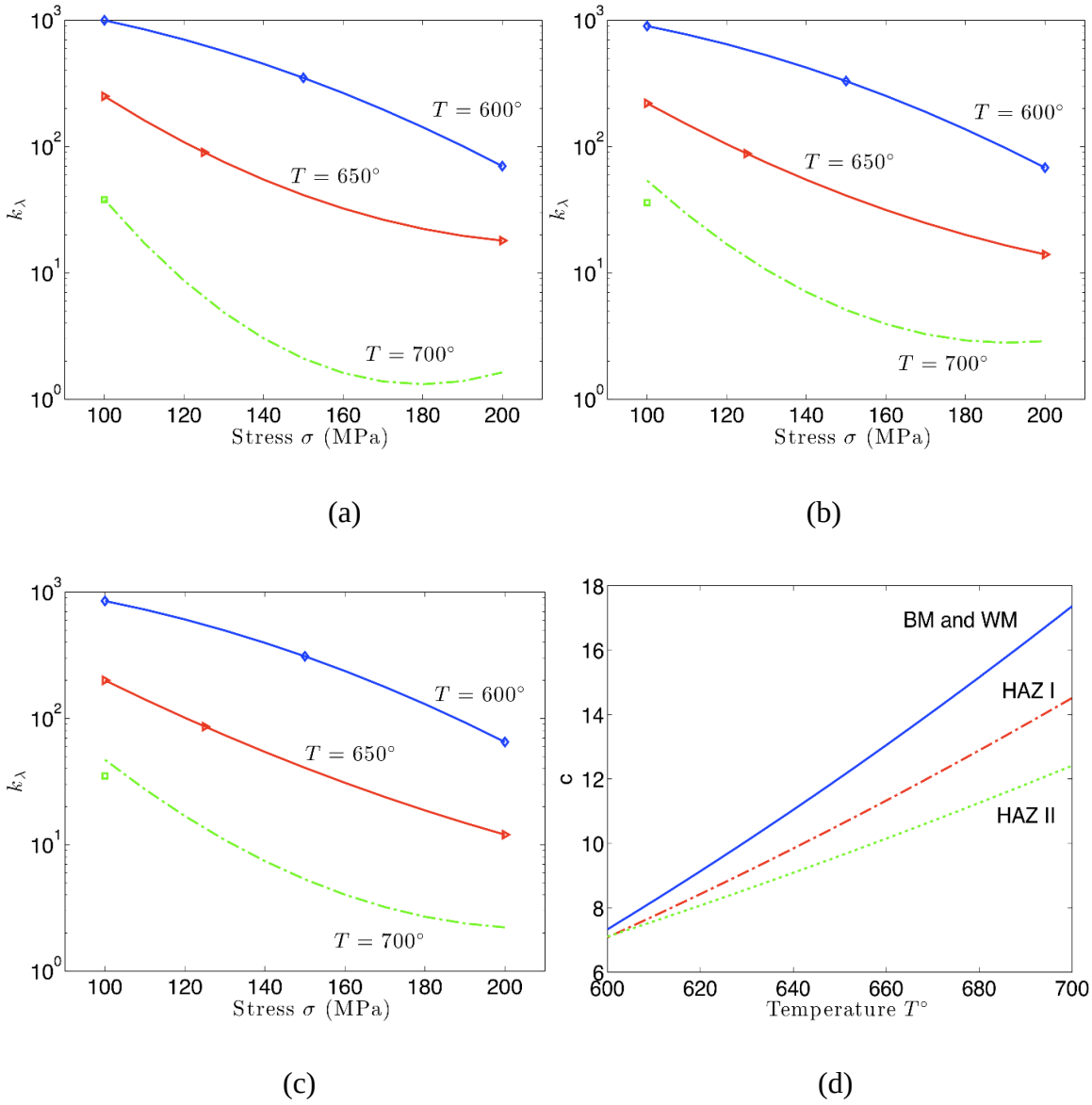

Figure 4-5. Logarithmic plot of k_i as a function of stress for T = 600 ˚C, 650˚C and 700˚C for (a) BM and WM, (b) HAZ I and (c) and HAZ II. (d) Quadratic curve-fitting of coefficient c. Solid curves represent fitted lines, while dash-dotted curve is the extrapolation for temperature T = 700˚C.

Finite element simulations have been performed in ABAQUS for a range of stresses and temperatures. Figures 4-6a-d show the displacement along the axis of the specimen, the maximum principle strain, and the von Mises stress on a cross-section and at the surface of the specimen, respectively.

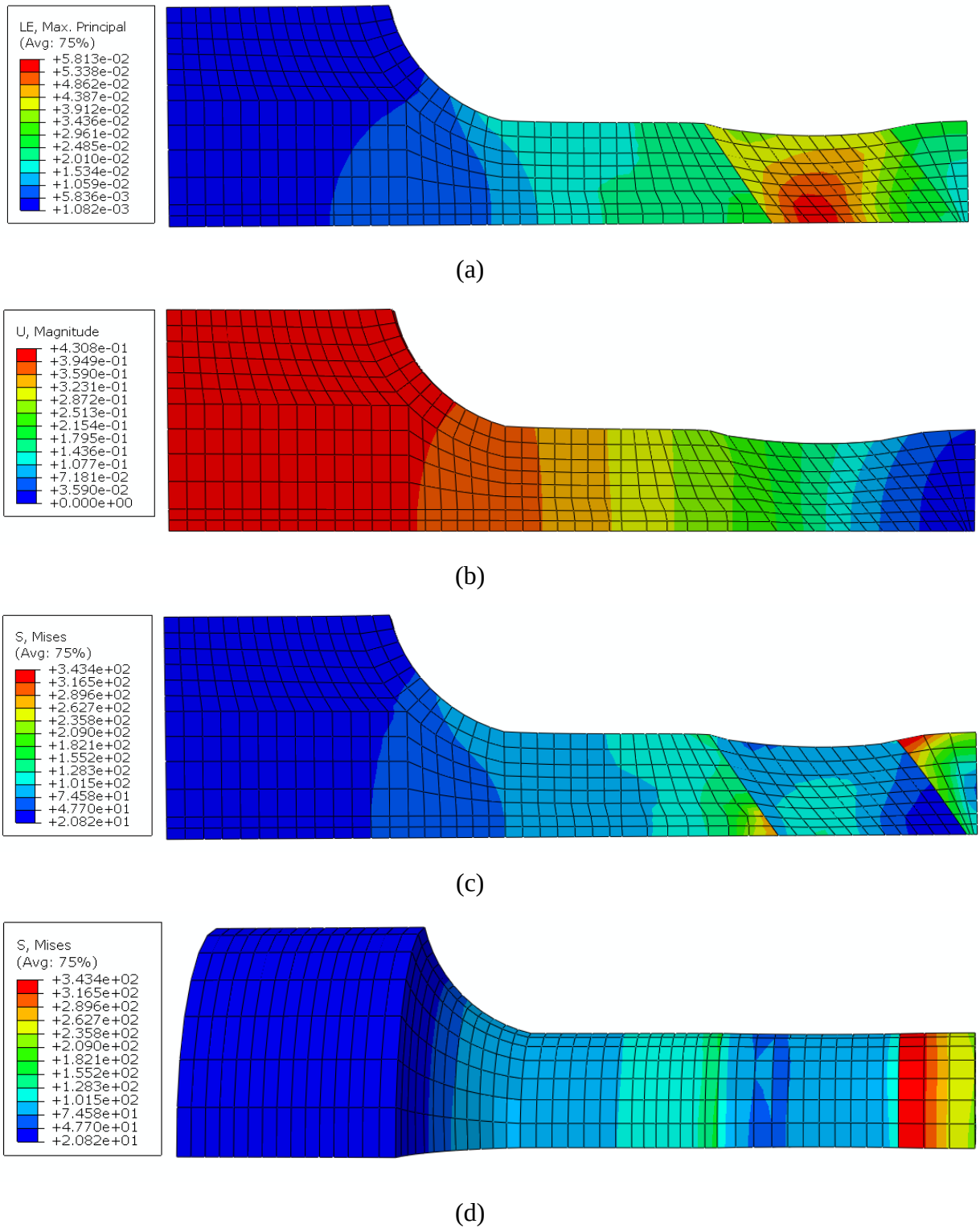

Figure 4-6. Finite element simulations of creep in a welded 9Cr-1Mo specimen subjected to an applied stress of 200 MPa and at a temperature of 600˚C: (a) maximum principal strain, (b) displacement along the axis of the specimen, (c) von Mises stress in the cross section of the specimen, and (d) the von Mises stress distribution at the surface of the specimen.

The constitutive model results and experimental results comparison for 100 MPa at 600˚C have been shown in Figure 4-7. Figure 4-7a is the creep strain rate versus time and Figure 4-7b is the true creep strain versus time. The simulation and experimental results comparison for 150 MPa at 600˚C have been shown in Figure 4-8. Again, Figure 4-8a is the creep strain rate versus time and Figure 4-8b is the true creep strain versus time.

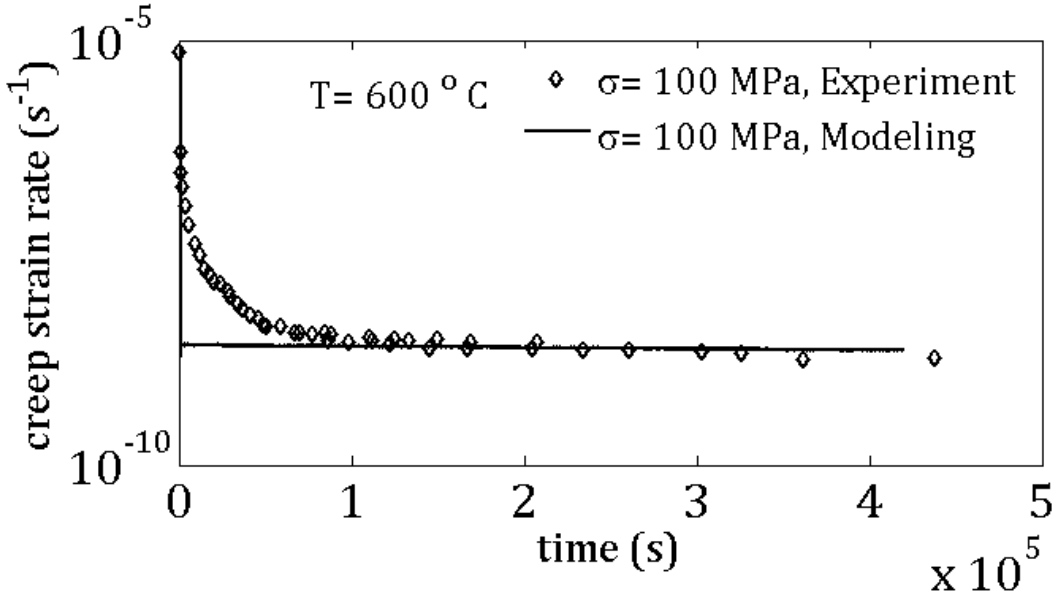

(a)

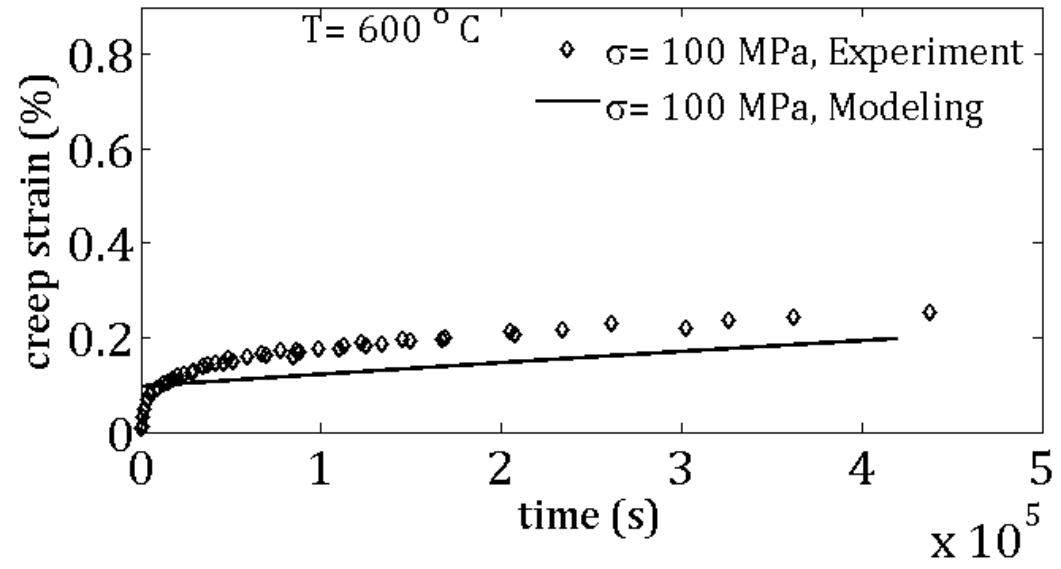

(b)

Figure 4-7. Creep results from experiments and finite element simulation for 100 MPa and 600˚C, (a) true creep strain rate versus time, (b) creep strain versus time.

For specimen crept at 200 MPa and 600˚C, Figures 4-9a and 4-9b, respectively, show the creep strain rate versus time and the true creep strain versus time.

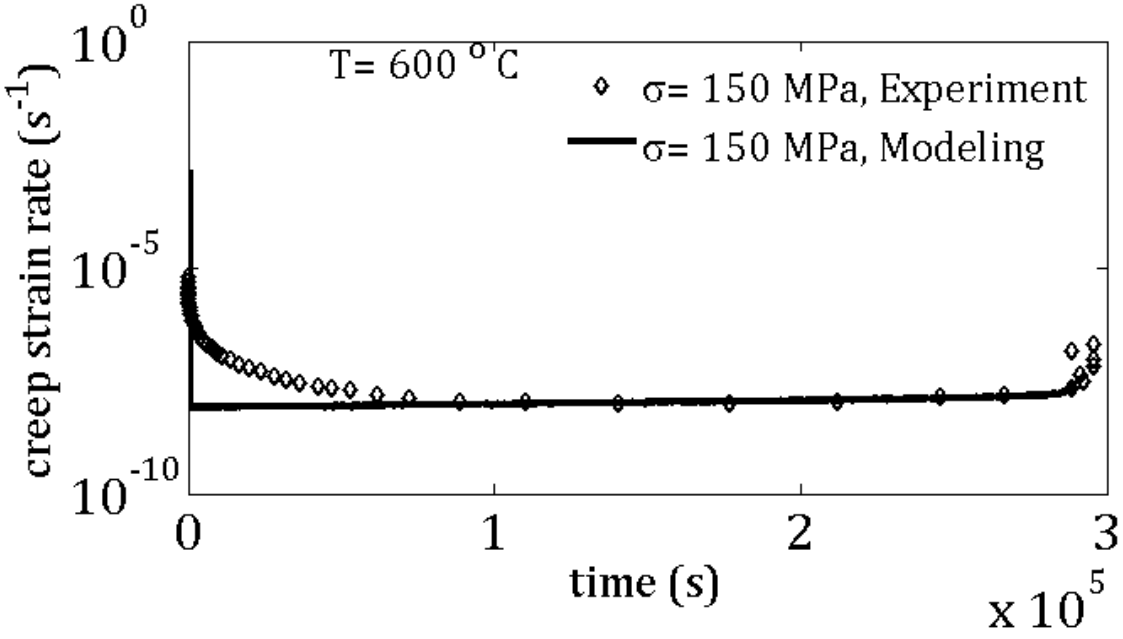

(a)

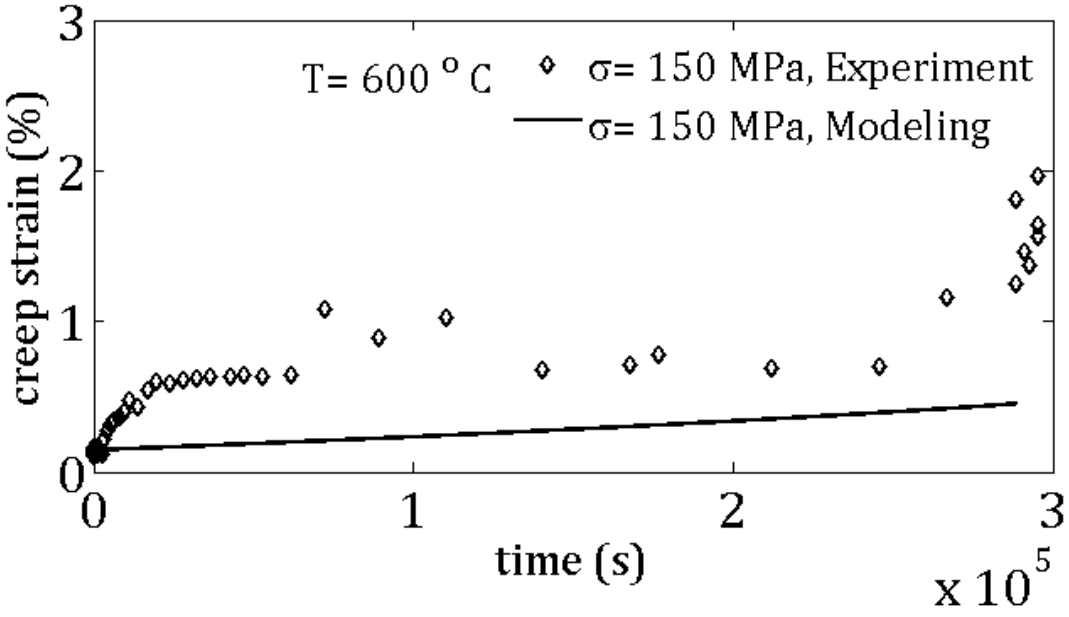

(b)

Figure 4-8. Creep results from experiments and finite element simulation for 150 MPa and 600˚C, (a) true creep strain rate versus time, (b) creep strain versus time.

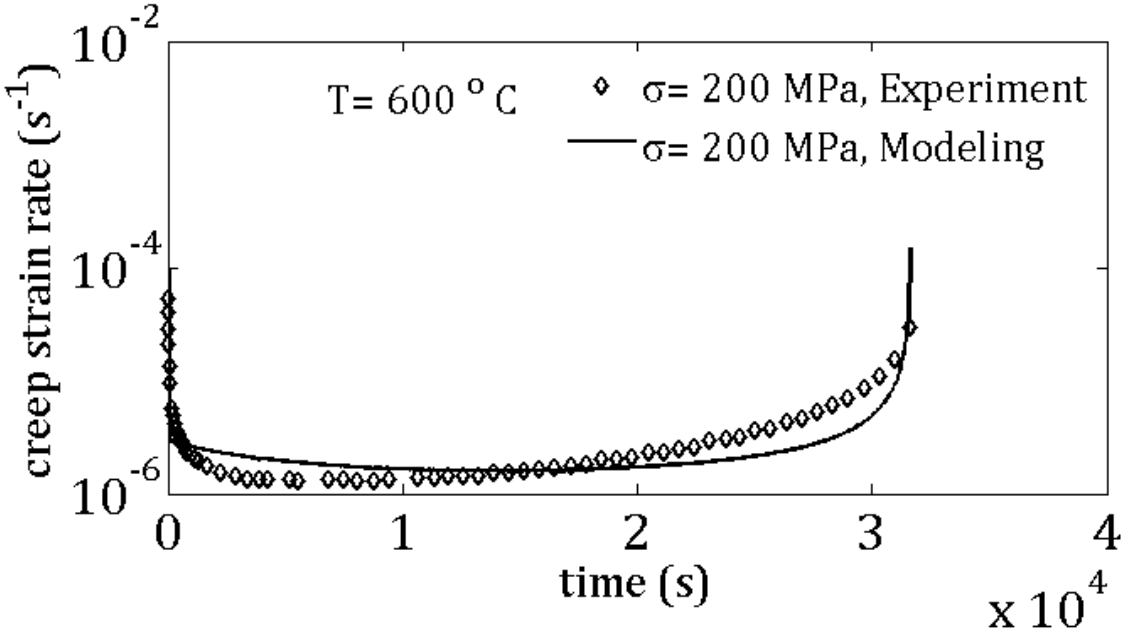

(a)

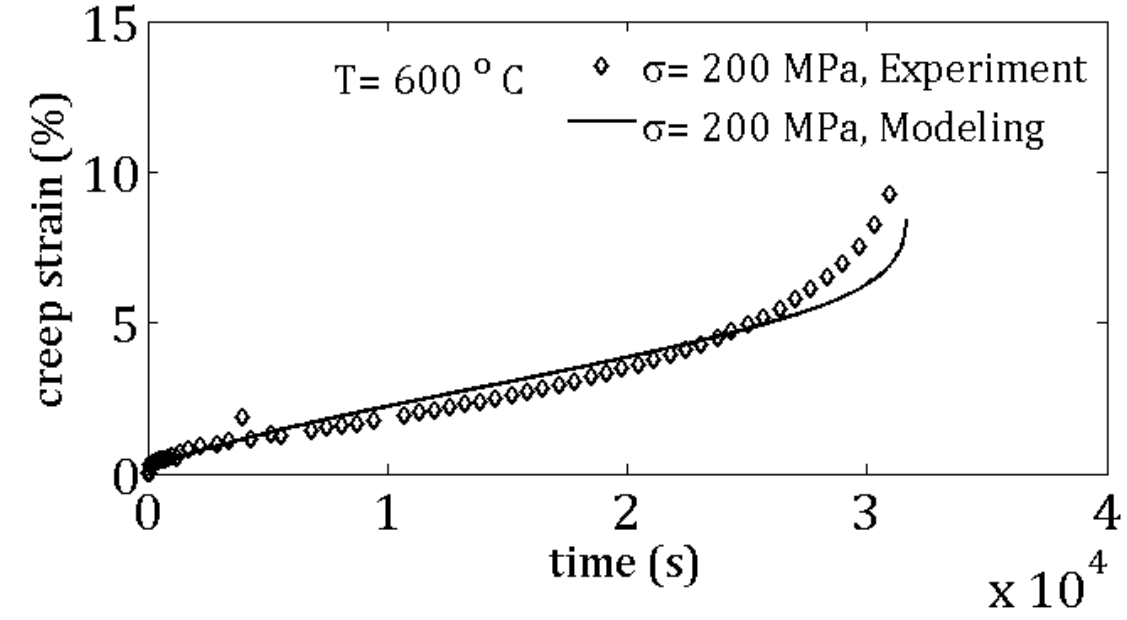

(b)

Figure 4-9. Creep results from experiments and finite element simulation for 200 MPa and 600˚C, (a) true creep strain rate versus time, (b) creep strain versus time.

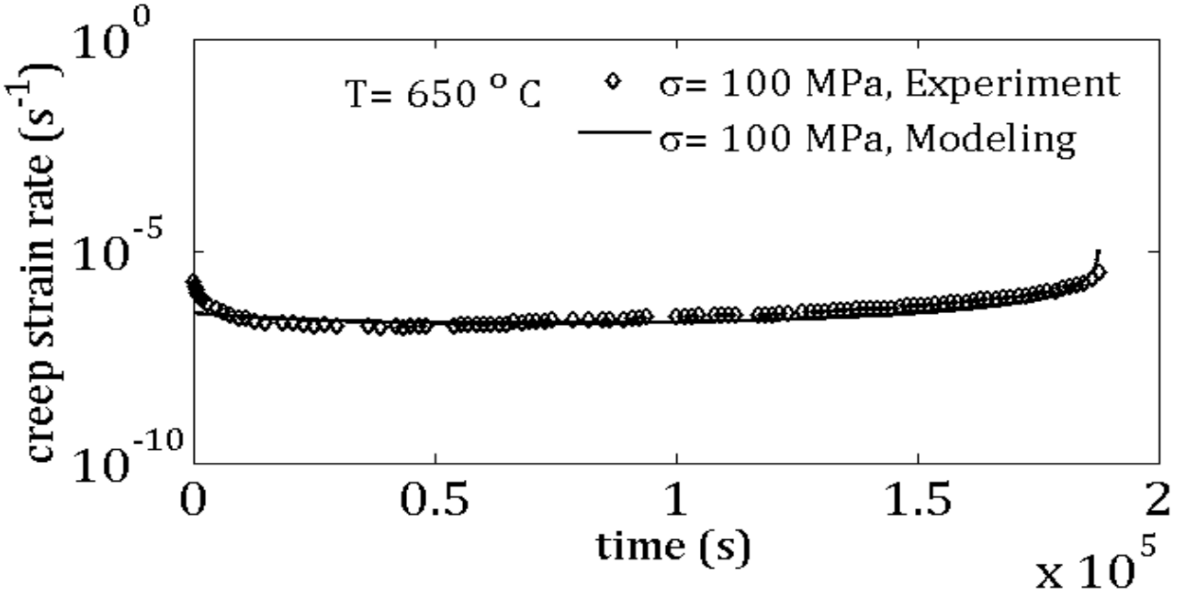

(a)

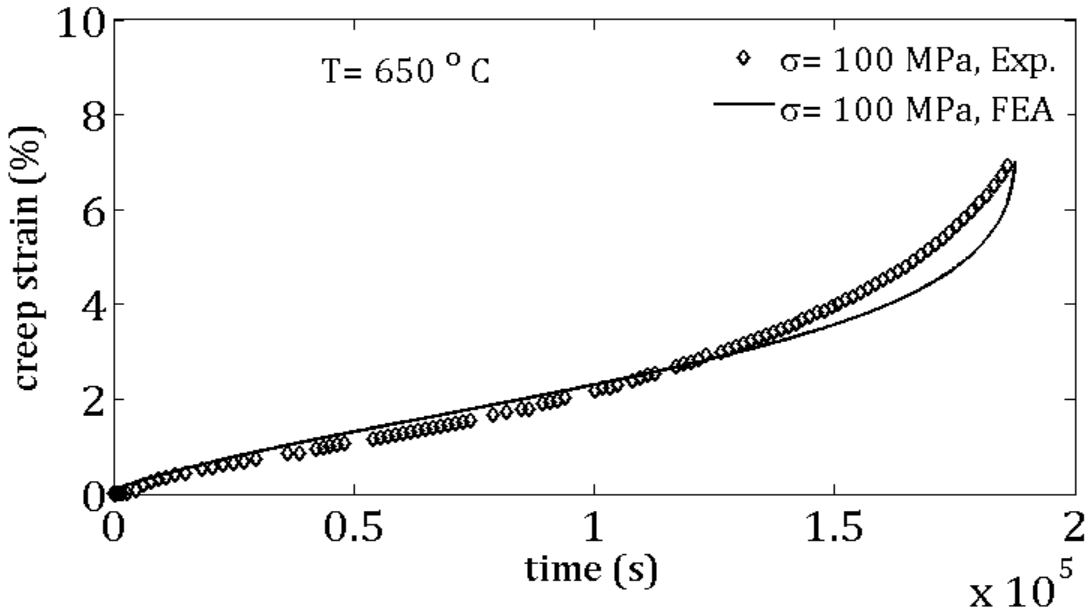

(b)

Figure 4-10. Creep results from experiments and finite element simulation for 100 MPa and 650˚C, (a) true creep strain rate versus time, (b) creep strain versus time.

The comparison of the modeling versus experimental result at 650˚C and applied stresses of 100 MPa, as well as 125 MPa and 200 MPa are shown in Figures 4-10, 4-11 and 4-12, respectively. Figures 13a-b show the comparison of creep strain rate versus time and true creep strain versus time at 700˚C and applied stress of 100 MPa.

In general, the model predicts well the evolution of the total creep strain and the creep strain rate with time, as measured experimentally. This agreement is particularly true for the stage II creep in most of the loading conditions, while a slight disagreement between experimental and simulation data is recorded at the transition between successive stages of creep. The model under-predicts the accumulation of the creep strain with time for the 150 MPa and 600˚C, but this is mainly due to its inability to capture well the transition in the creep strain rate between the I and the II creep stages. An overall assessment of the models leads to the conclusion that it can be used successfully to predict the deformation and fracture in modified 9Cr-1Mo welded steels for the large majority of testing conditions.

To exemplify the applicability of the constitutive model to three dimensional geometries, a creep simulation was performed for a pipe joined by a bolted connection to a flange. The pipe material was modified 9Cr-1Mo steel, while the flange material was Inconel X625. Due to symmetry, only a sector of the overall geometry was modeled in ABAQUS, and axisymmetric boundary conditions were used. The operating temperature is 575˚C, and the internal pressure is 17 MPa. The bolt has been tightened down with a force equal to 7500 N, the simulation has been run for 100 hours under operating condition. As an illustration, the creep deformation and stress distribution in this bolted joint have been plotted in Figure 14.

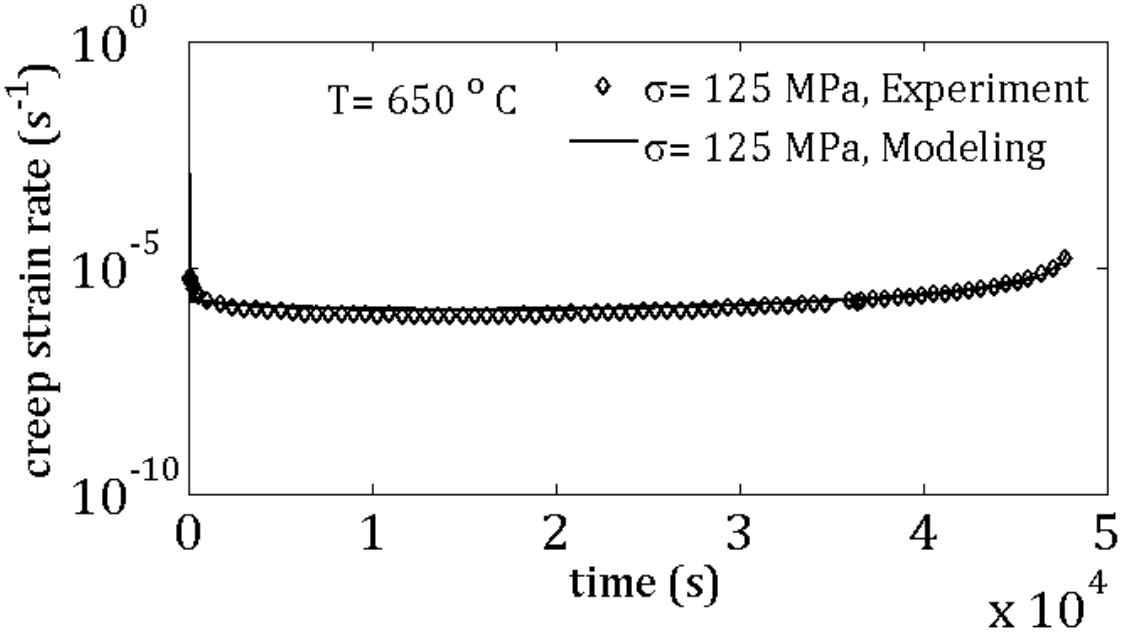

(a)

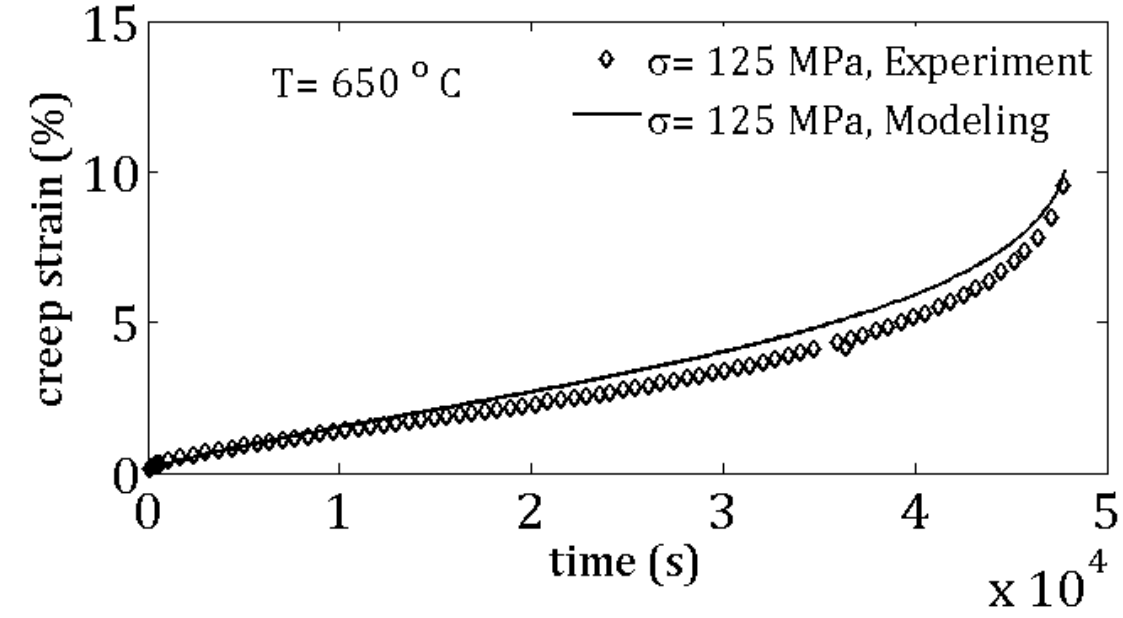

(b)

Figure 4-11. Creep results from experiments and finite element simulation for 125 MPa and 650˚C, (a) true creep strain rate versus time, (b) creep strain versus time.

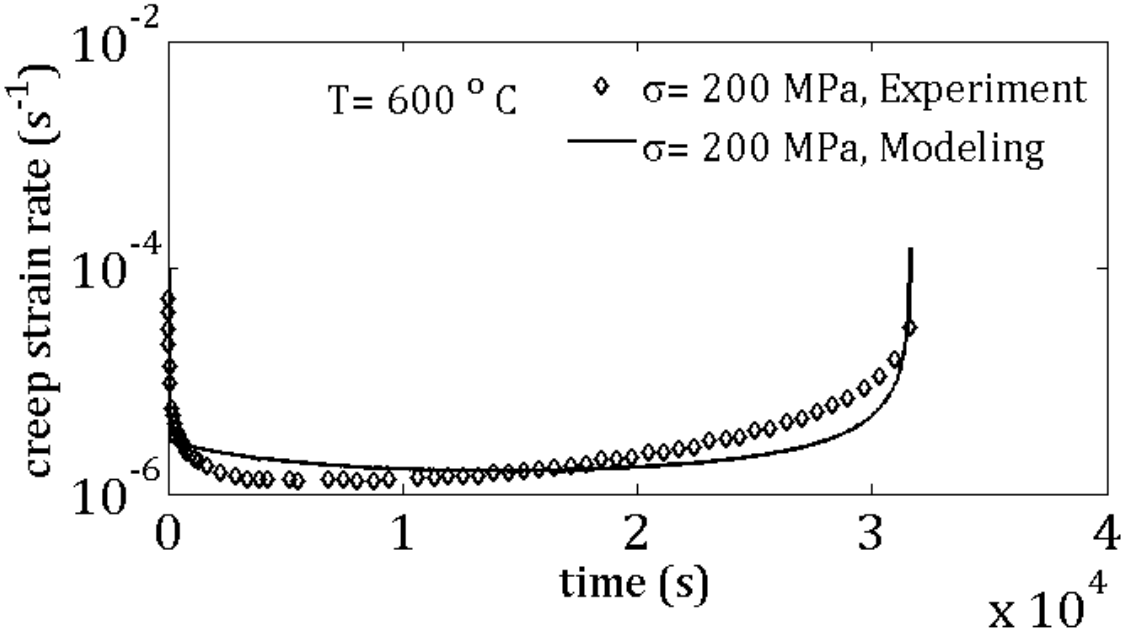

(a)

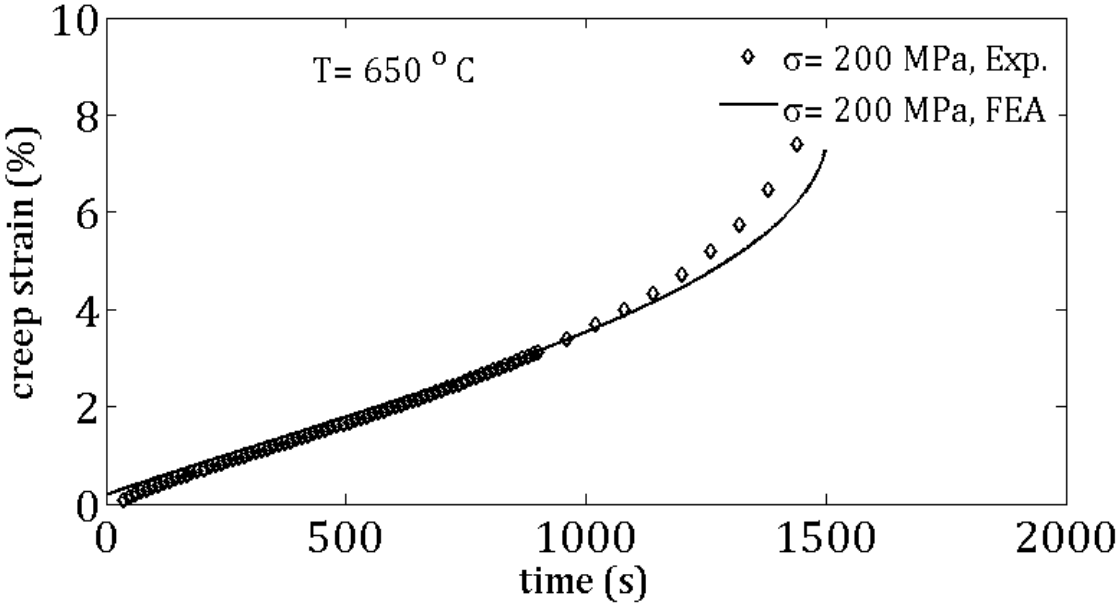

(b)

Figure 4-12. Creep results from experiments and finite element simulation for 200 MPa and 650˚C, (a) true creep strain rate versus time, (b) creep strain versus time.

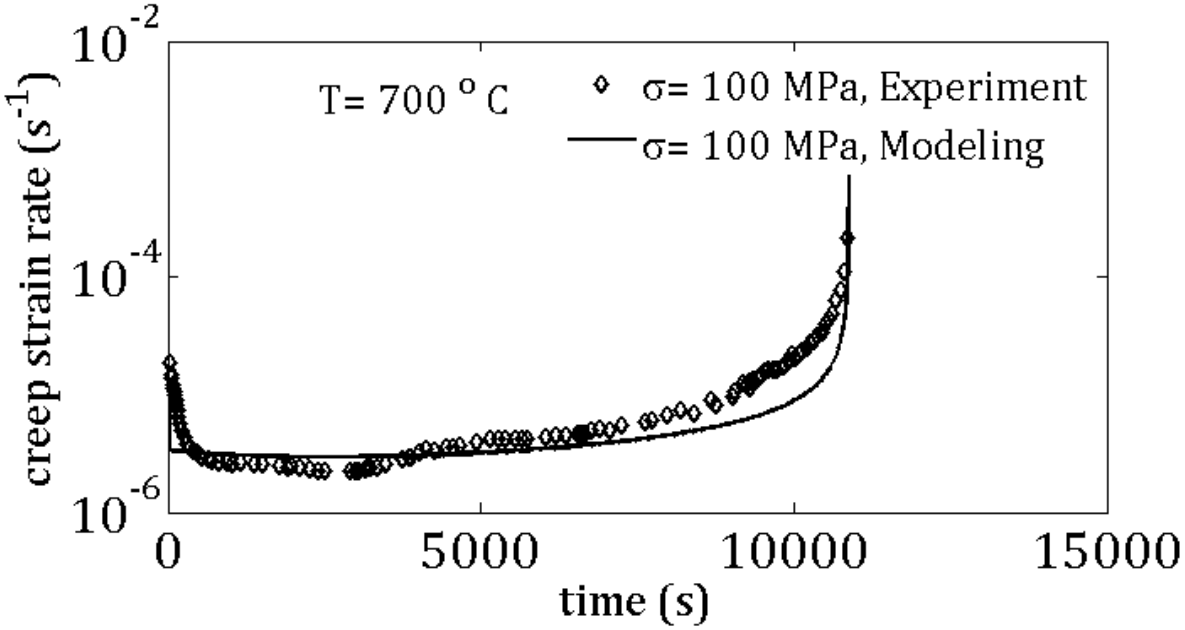

(a)

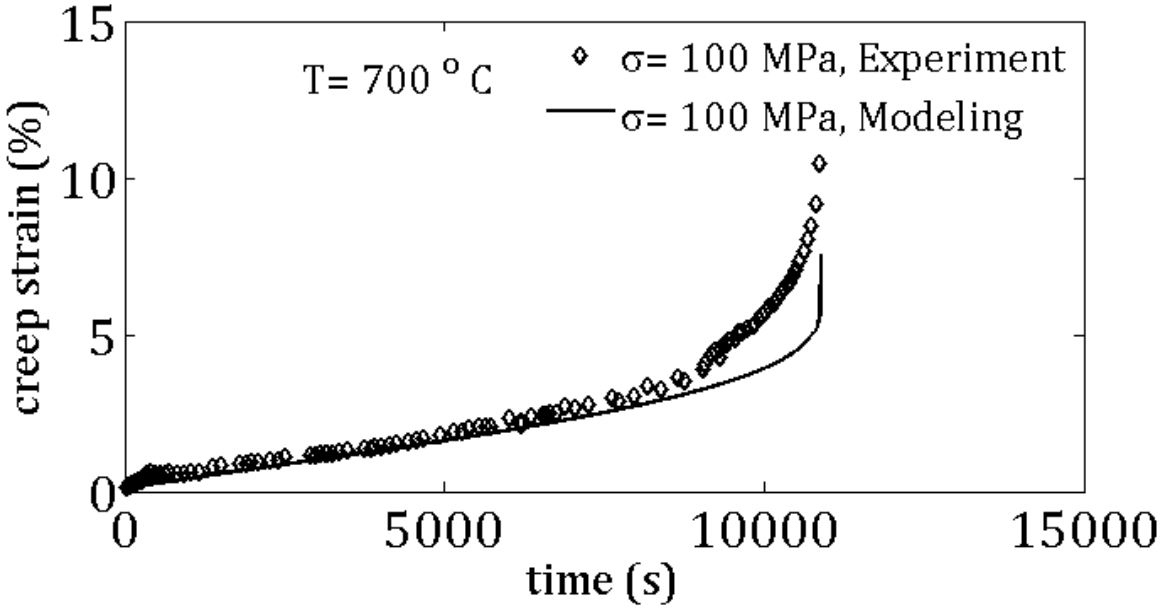

(b)

Figure 4-13. Creep results from experiments and finite element simulation for 100 MPa and 700˚C, (a) true creep strain rate versus time, (b) creep strain versus time.

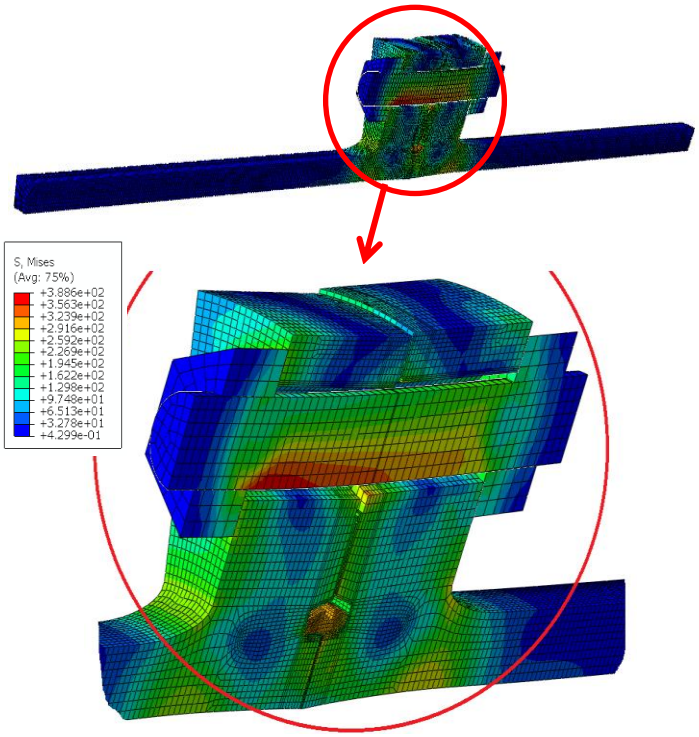

Figure 4-14. Example of a finite element simulation of creep stress distribution in a 9Cr-1Mo steel pipe connected to an Inconel X625 flange under thermo-mechanical loading. The operating temperature is 575˚C, and the internal pressure is 17 MPa.

4.6 Conclusions

A unified elasto-viscoplastic constitutive model for creep-damage was developed for modified 9Cr-1Mo welded steel. The model considered the main creep mechanism in this material to be the evolution of mobile dislocation density in the microstructure. In order to predict the stage III creep, several damage terms were introduced to capture the operating degradation phenomena in this steel. The model was implemented in ABAQUS using a User Material subroutine, and a semi-implicit numerical integration scheme was used to integrate the governing differential equations. Creep tests have been conducted on welded and non-welded specimens made of modified 9Cr-1Mo steel. The creep tests were simulated in ABAQUS utilizing the developed numerical model. The modeling creep results show good correlations with the experimental results for the temperature range of 600-700˚C and stress

range of 80 to 200 MPa. The model can be applied to study creep deformation and failure in three-dimensional complex geometries with different material properties.

4.7 Acknowledgments

The authors would like to gratefully acknowledge the Nuclear Energy University Program (NEUP) for providing the financial support for this research through DOE Grant 42246, release 59. Also we would like to thank Sintra Co., Holland for sharing the ABAQUS input file for the three-dimensional flange connection. The author L.L.B.'s work was also supported by the National Science Foundation Major Research Instrumentation Program, grant 1229766.

4.8 References

Auerkari, P., S. Holmström, J. Veivo, and J. Salonen. 2007. “Creep Damage and Expected Creep Life for Welded 9–11% Cr Steels.” Development of and Integrity Issues with New High Temperature High Strength Steels 84(1–2):69–74.

Basirat, M., T. Shrestha, G. P. Potirniche, I. Charit, and K. Rink. 2012. “A Study of the Creep Behavior of Modified 9Cr-1Mo Steel Using Continuum-Damage Modeling.” International Journal of Plasticity 37:95–107.

Besson, J., S. Leclercq, V. Gaffard, and A. F. Gourgues-Lorenzon. 2009. “Analysis of Creep Lifetime of a ASME Grade 91 Welded Pipe.” Engineering Fracture Mechanics 76(10):1460–73.

Blum, W., P. Eisenlohr, and F. Breutinger. 2002. “Understanding Creep—a Review.” Metallurgical and Materials Transactions A 33(2):291–303. Retrieved March 4, 2018 (http://link.springer.com/10.1007/s11661-002-0090-9).

Chilukuru, H. et al. 2009. “Coarsening of Precipitates and Degradation of Creep Resistance in Tempered Martensite Steels.” Materials Science and Engineering: A 510:81–87.

Dunne, Fionn. 2007. Introduction to Computational Plasticity. Oxford; New York: Oxford University Press.

Gaffard, V., A. F. Gourgues-Lorenzon, and J. Besson. 2005. “High Temperature Creep Flow and Damage Properties of 9Cr1MoNbV Steels: Base Metal and Weldment.” Nuclear Engineering and Design 235(24):2547–62.

Hyde, T. H., M. Saber, and W. Sun. 2010. “Creep Crack Growth Data and Prediction for a P91 Weld at 650 °C.” International Journal of Pressure Vessels and Piping 87(12):721–29.

Hyde, T. H. and A. Tang. 1998. “Creep Analysis and Life Assessment Using Cross-Weld Specimens.” International Materials Reviews 43(6):221–42. Retrieved March 4, 2018 (http://www.tandfonline.com/doi/full/10.1179/imr.1998.43.6.221).

Igari, T. et al. 2011. “Micro–macro Creep Damage Simulation for Welded Joints.” Materials at High Temperatures 28(3):181–87. Retrieved March 4, 2018 (http://www.tandfonline.com/doi/full/10.3184/096034011X13123545763673).

Laha, K., K. S. Chandravathi, P. Parameswaran, and K. Bhanu Sankara Rao. 2009. “Type IV Cracking Susceptibility in Weld Joints of Different Grades of Cr-Mo Ferritic Steel.” Metallurgical and Materials Transactions A 40(2):386–97.

Lee, Hyeong-Yeon, Jong-Bum Kim, Woo-Gon Kim, and Jae-Han Lee. 2010. "Creep-Fatigue Crack Behaviour of a Mod. 9Cr-1Mo Steel Structure with Weldments." Transactions of the Indian Institute of Metals 63(2–3):245–50.

Lemaître, J. 1990. Mechanics of Solid Materials. Cambridge: Cambridge University Press.

Morra, P. V., S. Radelaar, M. Yandouzi, J. Chen, and A. J. Böttger. 2009. "Precipitate Coarsening-Induced Plasticity: Low Temperature Creep Behaviour of Tempered SAE 52100." International Journal of Plasticity 25(12):2331–48.

Muñoz-Morris, M. A., I. Gutierrez-Urrutia, and D. G. Morris. 2009. "Influence of Nanoprecipitates on the Creep Strength and Ductility of a Fe–Ni–Al Alloy." International Journal of Plasticity 25(6):1011–23.

Naumenko, K. D. 2007. Modeling of Creep for Structural Analysis. Berlin; New York: Springer.

Shrestha, Triratna et al. 2012. "Creep Deformation Mechanisms in Modified 9Cr–1Mo Steel." Journal of Nuclear Materials 423(1–3):110–19. Retrieved March 4, 2018 (http://linkinghub.elsevier.com/retrieve/pii/S0022311512000098).

Spigarelli, S. and E. Quadrini. 2002. "Analysis of the Creep Behaviour of Modified P91 (9Cr–1Mo–NbV) Welds." Materials & Design 23(6):547–52. Retrieved March 4, 2018 (http://linkinghub.elsevier.com/retrieve/pii/S0261306902000262).

Watanabe, Takashi, Masaaki Tabuchi, Masayoshi Yamazaki, Hiromichi Hongo, and Tatsuhiko Tanabe. 2006. "Creep Damage Evaluation of 9Cr–1Mo–V–Nb Steel Welded Joints Showing Type IV Fracture." International Journal of Pressure Vessels and Piping 83(1):63–71. Retrieved March 4, 2018 (http://linkinghub.elsevier.com/retrieve/pii/S0308016105001274).

Weber, Gustavo and Lallit Anand. 1990. “Finite Deformation Constitutive Equations and a Time Integration Procedure for Isotropic, Hyperelastic-Viscoplastic Solids.” Computer Methods in Applied Mechanics and Engineering 79(2):173–202. Retrieved March 4, 2018 (http://linkinghub.elsevier.com/retrieve/pii/0045782590901315).

Yaghi, A. H., T. H. Hyde, A. A. Becker, and W. Sun. 2008. “Finite Element Simulation of Welding and Residual Stresses in a P91 Steel Pipe Incorporating Solid-State Phase Transformation and Post-Weld Heat Treatment.” The Journal of Strain Analysis for Engineering Design 43(5):275–93.

Yaguchi, Masatsugu, Takashi Ogata, and Takayuki Sakai. 2010. “Creep Strength of High Chromium Steels Welded Parts under Multiaxial Stress Conditions.” International Journal of Pressure Vessels and Piping 87(6):357–64. Retrieved March 4, 2018 (http://linkinghub.elsevier.com/retrieve/pii/S0308016110000530).

Chapter 5 - Developing A Unified Creep Plasticity Model to Analyze Permanent Deformations Of 9Cr-1Mo Steel

5.1 Introduction

In this chapter a numerical model has been developed for the study of creep fracture in Grade 91 steel specimens. Creep crack incubation in Cr-Mo steels has been studied using an elastic-plastic-creep modeling methodology. To predict creep crack growth under thermal and mechanical loading, a finite element model has been developed for the creep deformation and damage. The model considered the evolution of dislocation density as the main creep deformation mechanism. Furthermore, the effect of void growth and crack nucleation has been taken into account in the damage formulation. In order to measure and study the crack tip plastic zone during creep, the afore-mentioned model has been combined with a linear kinematic hardening model for plastic deformations. The model was implemented as a User Material subroutine (UMAT) in ABAQUS Standard. Crack-tip opening displacement (CTOD), crack tip plastic zone sizes, and material relaxation in the crack tip plastic zone were simulated.

5.2 Unified creep plasticity model

In this chapter the constitutive model for the unified plasticity-creep model is explained.

5.2.1 Constitutive creep plasticity equations

Accumulated strain is modeled here as the summation of the elastic, plastic, and creep strains,

$$\varepsilon_{ij} = \varepsilon_{ij}^{el} + \varepsilon_{ij}^{pl} + \varepsilon_{ij}^{cr} \tag{5-1}$$

and in the rate form

$$\dot{\varepsilon}_{ij} = \dot{\varepsilon}_{ij}^{el} + \dot{\varepsilon}_{ij}^{pl} + \dot{\varepsilon}_{ij}^{cr} \tag{5-2}$$

The creep strain rate is considered a function of the equivalent stress, temperature and some internal state variables,

$$\dot{\varepsilon} = \dot{\varepsilon}(\bar{\sigma}, T, \xi) \tag{5-3}$$

where the equivalent stress is computed as

$$\bar{\sigma} = \sqrt{\frac{3}{2} S_{ij} : S_{ij}}, \ where \, S_{ij} = \sigma_{ij} - \frac{1}{3}\delta_{ij}\sigma_{kk} \tag{5-4}$$

The evolution of state variables has the same general form as that for creep strains as

$$\dot{\xi}_a = q_a(\bar{\sigma}, T, \xi, \alpha) \tag{5-5}$$

In the present model, internal variables refer to the variables measuring dislocation density, solid solutions, precipitate size, and other strengthening mechanisms terms. These strengthening mechanisms could induce isotropic hardening in the material. This isotropic hardening resistance evolves during a thermally-activated deformation, such as creep. In a rate-dependent inelastic deformation, the rate of evolution of internal variables can also be expressed by the internal variable rate equations $\dot{\xi}_a$. Here, $\dot{\xi}_a$ is defined by some functions q_a which depends on σ, T, ξ, H. The elastic response of the material is modeled by the linear isotropic elastic equation. The linear isotropic elastic stress strain equation is valid for creep deformation, and it has been defined in Eq. 5-2.

$$\sigma_{ij} = 2G\varepsilon_{ij}^{el} + \lambda \delta_{ij}\varepsilon_{kk} \tag{5-6}$$

where G is the shear modulus and λ is Lame's constant. A continuum damage creep model has been developed in a previous work (Basirat et al. 2012). A simplified version of the mentioned model has been employed here to analyze the creep behavior of the modified 9Cr-1Mo steel. In the original model the density of the dipole dislocations was taken into account. By performing numerous simulations on the original model, it was observed that neglecting the dipole dislocations density reduces the number of equations significantly, while it doesn't change the simulation results considerably. Starting from the equations presented in (Basirat et al., 2015), the Orowan's equation for creep modified for damage was employed to evaluate the creep strain rate

$$\dot{\bar{\varepsilon}}^{cr} = \frac{\rho_m b B_{visc}}{M\,D}(\bar{\sigma} - \alpha MCGb\sqrt{\rho_m}) \tag{5-7}$$

In this equation ρ_m is the mobile dislocation density, b is the burger's vector, α is a dislocation interaction constant, M is the Taylor factor, C is the inelastic deformation factor (C has been considered equal to *0.2* in this research), and B_{visc} is the dislocation mobility term. For simplicity, the following notation is made $K_1 = \alpha MCGb$. The term D represents the damage caused by precipitate coarsening, depletion of solid solutions, and void and crack formation. The dislocation mobility term is defined according to (Blum, Eisenlohr, and Breutinger 2002) as

$$B_{visc} = \frac{9\Omega D_{sol} K_B T}{MC_0 G^2 b^7 \varepsilon_a^2 \ln(\frac{r_2}{r_1})} \tag{5-8}$$

where Ω is the atomic volume (which has been considered equal to b^3), K_B is the Boltzmann constant, T is the temperature, D_{sol} is the solute atom diffusion coefficient in solvent atoms, C_0 is the solute concentration, r_1 and r_2 are the inner and outer cut-off radii of the dislocation stress field, and ε_a, is the relative size misfit between solute and solvent atoms. The rate of evolution of mobile dislocations density is defined as the difference between the rate of generation of mobile dislocations ($\dot{\rho}_{m,gen}$), and the rate of annihilation of mobile dislocations density ($\dot{\rho}_{m,ani}$),

$$\dot{\rho}_m = \dot{\rho}_{m,gen} - \dot{\rho}_{m,ani} \tag{5-9}$$

The rate of generation of the mobile dislocation density is

$$\dot{\rho}_{m,gen} = \frac{\rho_m B_{visc} \sqrt{\rho_m}}{k_\Lambda D} (\bar{\sigma} - K_1 \sqrt{\rho_m}) \tag{5-10}$$

where k_Λ is a material parameter, and is a function of temperature and equivalent stress. The rate of annihiliation of the mobile dislocationsis modeled as

$$\dot{\rho}_{m,ani} = \frac{4M\dot{\varepsilon} d_{dip} \rho_m}{b n_g} \tag{5-11}$$

The rate of annihilation of mobile dislocation is equal to the summation of the densities of dislocations which annihiliate spontaneously and those which form dipoles. It is a function of strain rate, mobile dislocations density, Burger's vector, Taylor factor and the number of active

slip planes n_g. Replacing the $\dot{\varepsilon}$ in Eq. 5-11 by its value from Eq. 5-7 and the rate of annihilation of mobile dislocations could be expressed as,

$$\dot{\rho}_{m,ani} = \frac{4d_{dip}\rho^2{}_m B_{visc}}{n_g D}(\bar{\sigma} - K_1\sqrt{\rho_m}) \tag{5-12}$$

Two mobile disliocations with opposite sign approaching each other, at a certain distance they will form dipoles and produce sessile dislocations. This distance is d_{dip} called, the dipole formation distance and has been defined as

$$d_{dip} = \frac{M}{8\pi(1-\nu)}\frac{Gb}{\bar{\sigma}} \tag{5-13}$$

In this equation ν is the Poisson's ratio. Replacing d_{dip} in Eq. 5-12, the rate of annihilation of mobile dislocations will be,

$$\dot{\rho}_{m,ani} = \frac{4MbG\rho^2{}_m B_{visc}}{2\pi(1-\nu)n_g D\bar{\sigma}}(\bar{\sigma} - K_1\sqrt{\rho_m}) \tag{5-14}$$

5.2.2 Damage constitutive equations

The material microstructures will degrade during high temperature exposure. In other words, the strengthening mechanisms that have been used to increase the creep resistance of materials will become less effective during creep loading. The main strengthening mechanisms in modified 9Cr-1Mo steel are work hardening, solid solution strengthening, precipitation hardening, and grain boundary strengthening. It has been shown by several researchers that the Mo particles deplete in the subgrain matrix under long term thermo-mechanical loading

(Chilukuru H. 2009; Morra et al. 2009; Muñoz-Morris, Gutierrez-Urrutia, and Morris 2009). Moreover, the precipitate coarsening ($M_{23}C_6$ and MX) in modified 9Cr-1Mo increases the interparticle spacing between precipitates. Solid solutions depletion and precipitate coarsening increase the dislocations mobility. Consequently, dislocations require less energy to move [3]. Furthermore, void nucleation and crack formation is one of the most important creep damage mechanisms in 9Cr-1Mo steel. The cavities usually nucleate at triple junctions or at the particles located at grain boundaries. Grain deformation and cavity coalesce are the main crack formation mechanisms in 9Cr-1Mo steel.

Mo is added to 9Cr-1Mo steel to induce solid solution strengthening. During creep loading the Mo particles deplete in the subgrain matrix and form precipitation of Fe_2Mo Laves phase. It has been shown by experiments that Fe_2Mo precipitates with low volume fraction and larger size could not effectively block dislocations motions. This large size laves phases (Fe_2Mo) are a source for dislocations absorbent, and they are brittle phases. These inopportune properties will lead to a reduction of the creep resistance of modified 9Cr-1Mo. (Lee et al., 2006).

Eq. 5-15 and Eq. 5-16 show the damage caused by solid solution depletion and its corresponding rate, respectively (Kadoya et al., 1997 and Semba et al., 2008). D_s is the solid solution depletion term and is a function of the initial and current solid solution concentrations, C_0 and C_t

$$D_s = 1 - \frac{\bar{C}_t}{C_0} \tag{5-15}$$

$$\dot{D}_S = K_S D_S^{1/3}(1-D_S) \tag{5-16}$$

where, K_S is the material parameter.

Another important damage mechanism in 9Cr-1Mo steel is caused by the coarsening of $M_{23}C_6$ and MX precipitates. The coarsening of precipitates increases interparticle spacing and, consequently, increases dislocation mobility, which in turn decreases the creep resistance. The damage and damage evolution equations due to precipitate coarsening are written as

$$D_P = 1-\frac{P_0}{P_t} \tag{5-17}$$

$$\dot{D}_p = k_p(1-D_p)^4 \tag{5-18}$$

where P_0 and P_t are the initial and current size of the precipitates, and k_P is a material parameter.

A leading failure mechanism during creep deformation of modified 9Cr-1Mo is crack incubation and growth. Microstructural stress concentrations are responsible for grain boundary sliding leading to the formation of creep cavities and creep crack formation. Creep crack formation and growth has been extensively studied in the literature. (Lemaître 1990). In this study, a modified Kachanov damage model has been employed for the crack-driven creep damage. Creep damage is expressed as a function of the creep exposure time (t), creep rupture time ($t_{rupture}$), and a material parameter B. The creep rupture time can be obtained from experiments. To summarize the crack-driven damage is expressed as

$$D_N = 1-(1-\frac{t}{t_{rupture}})^{1/(1+B)} \tag{5-19}$$

For simplicity, the total damage in the material caused by solid solution depletion, precipitate coarsening and crack formation is denoted as D , and is defined as

$$D = D(D_S, D_P, D_N) = (1 - D_S)(1 - D_P)(1 - D_N) \quad (5\text{-}20)$$

5.3 Numerical Integration

In order to be able to simulate three-dimensional geometries or components made of different materials, one has to use the finite element method. The analytical model presented in the previous section was implemented in the finite element code ABAQUS Standard as a User Material (UMAT) subroutine. Creep deformation is a history-dependent process. To solve the set of differential equations representing the constitutive model, it is necessary to discretize these equations and integrate them over time. First, the governing equations for the equivalent stress are presented.

The strain decomposition rule should be valid at any time increment *(n)* for any increment of trial strain,

$$\varepsilon_{ij,n+1}^{el} = \varepsilon_{ij,n}^{el} + (\Delta\varepsilon_{ij}^{tr} - \Delta\varepsilon_{ij}^{cr} - \Delta\varepsilon_{ij}^{pl}) \quad (5\text{-}21)$$

Replacing Eq. 5-21 in Eq. 5-2 and after some re-arrangement, the stress in the predictor-corrector form is

$$\sigma_{ij} = \sigma_{ij}^{tr} - 2G(\Delta\varepsilon_{ij}^{cr} + \Delta\varepsilon_{ij}^{pl}) . \quad (5\text{-}22)$$

From the classical theory of isotropic plasticity, it is possible to express the components of the creep strain rate tensor in the direction of stress as

$$\dot{\varepsilon}_{ij}^{cr} = \lambda S_{ij} = \frac{3}{2}\dot{\bar{\varepsilon}}^{cr}\frac{S_{ij}}{\bar{\sigma}}, where\ \lambda = \frac{3\dot{\bar{\varepsilon}}^{cr}}{2\bar{\sigma}}. \quad (5\text{-}23)$$

where λ is the creep strain multiplier. From the previous equation, multiplying by time increment Δt,

$$\Delta\varepsilon_{ij}^{cr} = \frac{3}{2}\Delta\dot{\bar{\varepsilon}}\frac{S_{ij}}{\bar{\sigma}}\Delta t = \frac{3}{2}\Delta\bar{\varepsilon}^{cr}\frac{S_{ij}}{\bar{\sigma}} = \mathbf{n}\Delta\bar{\varepsilon}^{cr}. \quad (5\text{-}24)$$

where $\mathbf{n}$ is the unit vector normal to the yield surface. The above equation represents the so-called normality rule. It can be shown that $\mathbf{n} = \frac{3}{2}\frac{S_{ij}}{\bar{\sigma}}$. The yield function is defined in Eq. 5-25 and the equivalent plastic strain obtained from Eq. 5-26

$$f_s = \sqrt{\frac{3}{2}(S_{ij} - \alpha_{ij})(S_{ij} - \alpha_{ij})} - \sigma_y = 0 \quad (5\text{-}25)$$

$$\dot{\bar{\varepsilon}}^{pl} = \sqrt{\frac{2}{3}\dot{\varepsilon}^{pl}\dot{\varepsilon}^{pl}} \quad (5\text{-}26)$$

The plastic flow rule is,

$$\dot{\varepsilon}_{ij}^{pl} = \frac{3}{2}\left(\frac{S_{ij} - \alpha_{ij}}{\sigma_y}\right)\dot{\bar{\varepsilon}}^{pl}. \quad (5\text{-}27)$$

The linear isotropic hardening rule is defined as

$$\dot{\alpha}_{ij} = \frac{2}{3}H\dot{\varepsilon}_{ij}^{pl} \quad (5\text{-}28)$$

where, *H* is the kinematic hardening parameter and is obtained from the stress strain curve of the material. Also, the increment in the equivalent plastic strain is

$$\Delta\bar{\varepsilon}^{pl} = \left(\frac{\bar{\sigma}^{tr} - \sigma_y}{H + 3G}\right) \tag{5-29}$$

With some algebra it is possible to rewrite Eq. 5-22 in the equivalent stress format (Dunne 2007).

$$\bar{\sigma} - \bar{\sigma}^{tr} + 3G(\Delta\bar{\varepsilon}^{cr} + \Delta\bar{\varepsilon}^{pl}) = 0 \tag{5-30}$$

Eq. 5-25 is the governing equation for the equivalent creep stress, while the trial stress $\bar{\sigma}^{tr}$ is calculated using Eq. 5-6. In addition to the creep strain, another state variable considered in this model is the density of mobile dislocations ρ_m. Replacing Eq. 5-10 and Eq. 5-14 in Eq. 5-9, the rate of change of mobile dislocation density becomes

$$\dot{\rho}_m = g(\bar{\sigma}, \rho_m, D) = \frac{\rho_m B_{visc}(\bar{\sigma} - K_1\sqrt{\rho_m})}{D}\left(\frac{\sqrt{\rho_m}}{K_\Lambda} - \frac{4d_{dip}\rho_m}{n_g}\right) \tag{5-31}$$

The damage integration is performed using an explicit scheme as

$$D_{n+1} = D_n + \dot{D}_n \Delta t \tag{5-32}$$

The following equations show the discretized form of Eq. 5-25 and Eq. 5-26

$$F(\bar{\sigma}_{n+1}, \rho_{m_{n+1}}, \Delta\bar{\varepsilon}^{pl}_{n+1}, D_n) = \bar{\sigma}_{n+1} - \bar{\sigma}^{Tr}_{n+1} + 3Gf(\bar{\sigma}_{n+1}, \rho_{m_{n+1}}, \Delta\bar{\varepsilon}^{pl}_{n+1}, D_n) = 0 \tag{5-33}$$

$$G(\bar{\sigma}_{n+1}, \rho_{m_{n+1}}, D_n) = \rho_{m_{n+1}} - \rho_{m_n} + g(\bar{\sigma}_{n+1}, \rho_{m_{n+1}}, D_n) = 0 \tag{5-34}$$

$$P(\bar{\sigma}_{n+1}, \rho_{m_{n+1}}, \Delta\bar{\varepsilon}^{pl}_{n+1}, D_n) = \Delta\bar{\varepsilon}^{pl}_{n+1} - (\frac{\bar{\sigma}_{n+1} - \sigma_y}{H + 3G}) = 0 \tag{5-35}$$

To solve the above system of equations, the Newton-Raphson (N-R) method combined with a backline search algorithm was used. The Jacobian matrix needed in the N-R method was computed numerically, however, an analytical form can also be obtained. At the end of each time step, the damage terms have been explicitly updated. The N-R method gives the increments for the equivalent stress and dislocation density

$$\begin{pmatrix} \Delta\bar{\sigma}_{n+1} \\ \Delta\rho_{m_{n+1}} \\ \Delta\bar{\varepsilon}^{pl}_{n+1} \end{pmatrix} = -\begin{pmatrix} \frac{\partial F}{\partial\bar{\sigma}_{n+1}} & \frac{\partial F}{\partial\rho_{m_{n+1}}} & \frac{\partial F}{\partial\bar{\varepsilon}^{pl}_{n+1}} \\ \frac{\partial G}{\partial\bar{\sigma}_{n+1}} & \frac{\partial G}{\partial\rho_{m_{n+1}}} & \frac{\partial G}{\partial\bar{\varepsilon}^{pl}_{n+1}} \\ \frac{\partial P}{\partial\bar{\sigma}_{n+1}} & \frac{\partial P}{\partial\rho_{m_{n+1}}} & \frac{\partial P}{\partial\bar{\varepsilon}^{pl}_{n+1}} \end{pmatrix}^{-1} \begin{pmatrix} F(\bar{\sigma}_n, \rho_{m_n}, \bar{\varepsilon}^{pl}_n, D_{n-1}) \\ G(\bar{\sigma}_n, \rho_{m_n}, \bar{\varepsilon}^{pl}_n, D_{n-1}) \\ P(\bar{\sigma}_n, \rho_{m_n}, \bar{\varepsilon}^{pl}_n, D_{n-1}) \end{pmatrix} \tag{5-36}$$

then, $\bar{\sigma}_{n+1}$, and $\rho_{m_{n+1}}$ will be updated using $\bar{\sigma}_{n+1} = \bar{\sigma}_n + \Delta\bar{\sigma}_{n+1}$, and $\rho_{m_{n+1}} = \rho_{m_n} + \Delta\rho_{m_{n+1}}$.

The damage term D_n is updated with Eq. 5-27. Introducing the updated variables and D_n in Eq. 5-31, the $\dot{\bar{\varepsilon}}^{cr}_{n+1}$ will be found and then $\Delta\bar{\varepsilon}^{cr}$

$$\dot{\bar{\varepsilon}}^{cr}_{n+1} = f(\bar{\sigma}_{n+1}, \rho_{m_{n+1}}, \Delta\bar{\varepsilon}^{pl}_{n+1}, D_n) = \frac{\rho_{m_{n+1}} bB_{visc}}{M D_n}(\bar{\sigma}_{n+1} - \alpha MCGb\sqrt{\rho_{m_{n+1}}}) \tag{5-37}$$

Substituting the equivalent increment of creep strain ($\Delta\bar{\varepsilon}^{cr}$) in Eq. 5-23, the components of the creep strain tensor will be obtainable. Once the strain increment and strain tensors

components are obtained, the stress increment and stress tensor components will be obtain using Eq. 5-38,

$$\sigma_{ij_{n+1}} = C^{el}_{ijkl}\left(\Delta\varepsilon^{tr}_{kl_{n+1}} - \Delta\varepsilon^{cr}_{kl_{n+1}} - \Delta\varepsilon^{pl}_{kl_{n+1}}\right) + \sigma_{ij_n} . \qquad (5\text{-}38)$$

5.4 Results and discussions

The developed UMAT has been used to study the deformation, strain and stress fields around near the crack tip of a Cr-Mo steel specimen. A center crack panel in tension was the specimen chosen for analysis. The geometry was generated and meshed using ANSYS APDL. The crack file was exported to ABAQUS by using a FORTRAN code to generate the required input file. The specimen was loaded under uniform uniaxial tension. Symmetry boundary conditions were applied to the model. Because of double symmetry, only a quarter of the model was studied. Figure 5-1 shows the geometry, mesh and boundary conditions applied to the crack. The symmetry boundary conditions were applied to the nodes on the *X* and *Y* axis and the other side of the plate was restricted from moving in the Z direction.

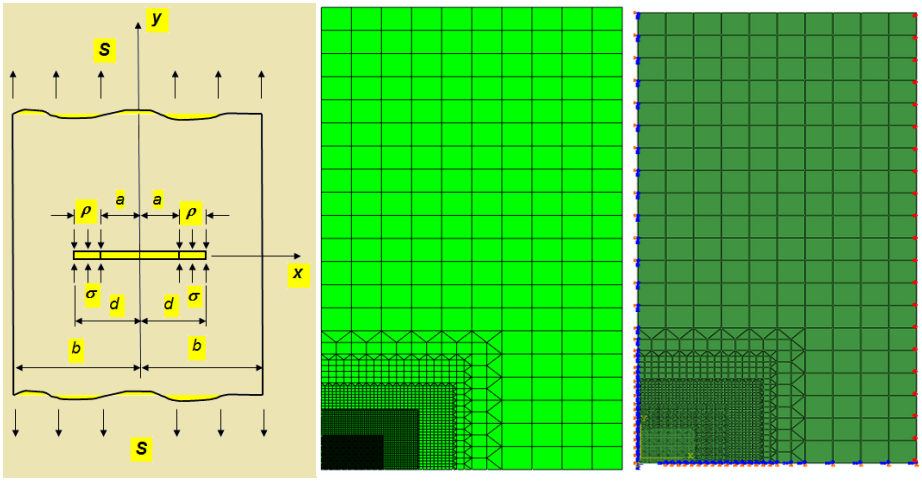

Figure 5-1. Cracked specimen geometry, finite element mesh and boundary conditions.

Figure 5-2 shows the crack mouth opening at different time increments. A tensile distributed load equal to 150 MPa was applied to the top surface of the plate, and the temperature considered in the analysis was 600° C. The deformation scales on the deformed mesh plots have been changed to visualize the creep crack mouth opening. Figure 5-3 shows the crack-tip opening for a plate with a 1-mm center crack under a tensile load equal to 200 MPa.

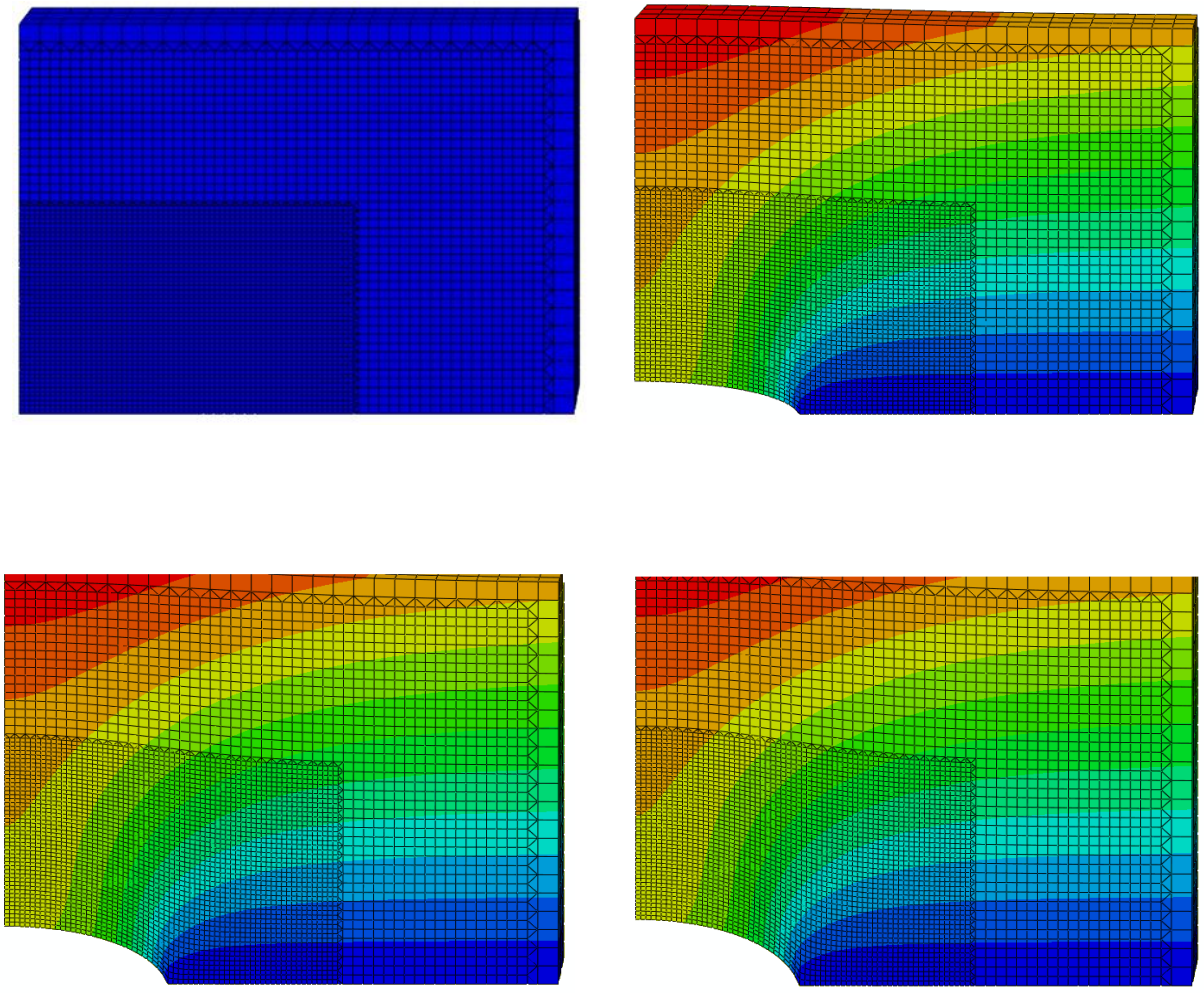

Figure 5-2. Crack opening displacements at creep hold times of 3.3, 34.5, and 70 hours. Deformed shape scale factor is 10.

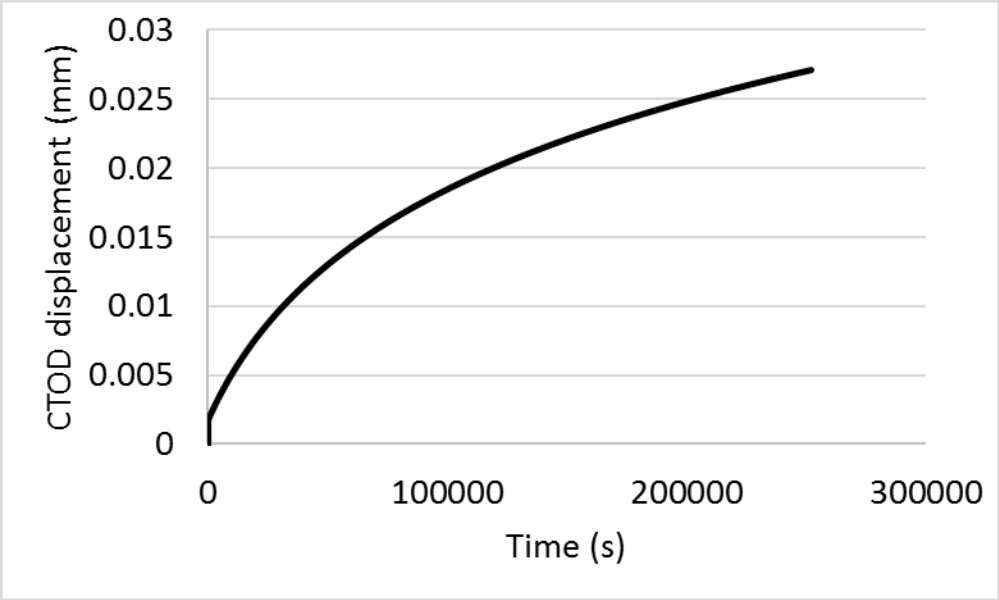

Figure 5-3. Crack tip opening displacement (CTOD) versus time.

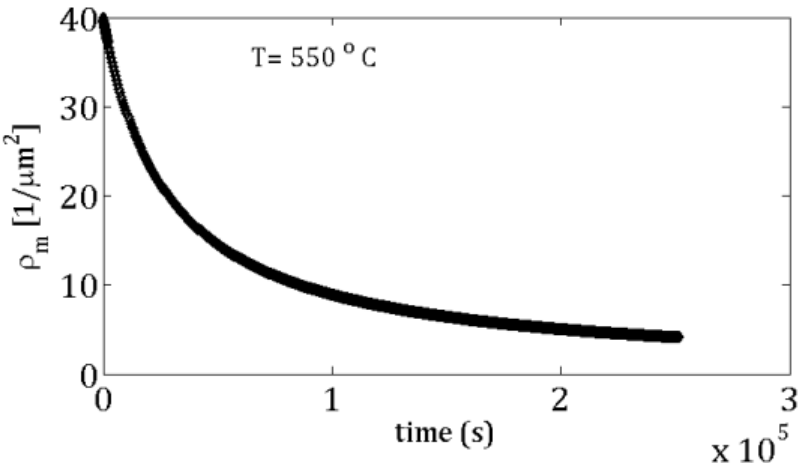

Figure 5-4. Evolution of the mobile dislocation density versus time at the crack tip.

As it was discussed in the model formulation section, the dislocation evolution during creep has been considered as the main mechanism for the creep deformation. Figure 5-4 shows the mobile dislocation evolution versus time at the crack tip. The dislocation density drops by 8 times at the crack tip. This, in turn, will decrease the resistance of the material against creep

deformation. Figure 5-5 show the variations of the stress versus the distance from crack tip axes after 34.4 hours exposure to loading. As it was expected, at further distance from crack tip the stress is lower, and the maximum stress is localized in the near crack-tip region.

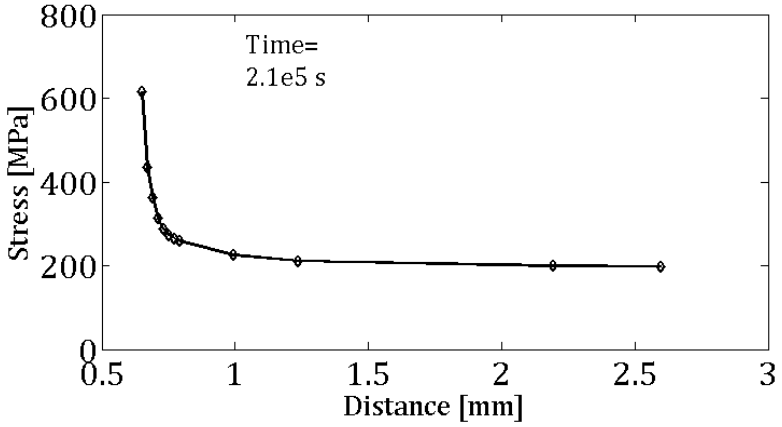

Figure 5-5 Stress variations along the crack axis at time equal to 33 hrs.

The other capability of this model is to predict the plastic zone size around the crack tip. The developed model is also capable of capturing the changes in plastic zone size during exposure at elevated temperatures. Figures 5-6a and 5-6b show a comparison of the plastic zone size at the beginning of creep loading and after 70 hours of loading. As shown in these plots, the crack tip stresses decrease over time. The maximum stress at the crack tip increases significantly, but it decreases as the material gets softer. Because of the large creep deformations and reduction of the specimen cross section, in the near crack-tip region, the stress decreases to approximately 450 MPa. Also, it can be observed that the stresses on the crack edge increases over time, which means that the plastic zone simultaneously shrinks and moves towards the crack edge.

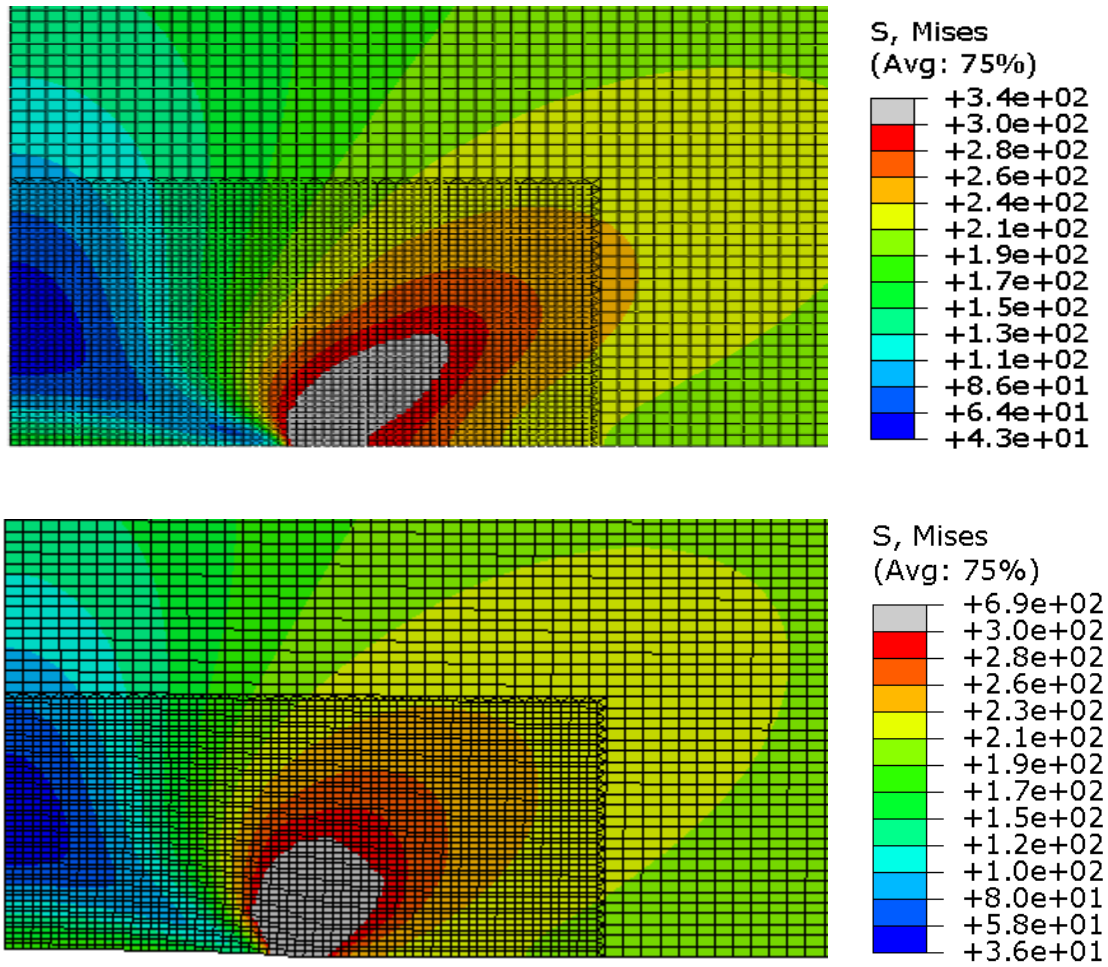

Figure5-6. Comparison between plastic zone before exposure (top) and after 250,000 s of exposure (bottom). The yield strength of the material is 300 MPa.

5.5 Conclusion

A unified creep-plasticity model was developed and used to study the crack evolution in a cracked component. The method uses Orowan's equation for computing creep strains, and combines this equation with isotropic hardening plasticity to capture the large plastic region around the crack tip. The model was used to compute crack-tip opening displacements (CTOD), the change of dislocation density around the crack tip, the variation of stresses at the

crack tip over time and the stress variation with distance in the crack plane for a plate with a center crack in tension. As it was expected, after exposing the crack tip to high stresses, the dislocation density will reduce over time. The reduction in dislocation density will cause material softening consequently more permanent deformations. The model can predict the changes in the plastic zone size as it grows towards the plate edge during the creep loading. The model predicts the stress relaxation in the component and specifically at the crack tip area. The model can be easily applied to any three-dimensional geometry under creep loading.

5.6 References

Basirat, M., T. Shrestha, G. P. Potirniche, I. Charit, and K. Rink. 2012. "A Study of the Creep Behavior of Modified 9Cr-1Mo Steel Using Continuum-Damage Modeling." International Journal of Plasticity 37:95–107.

Basirat, Mehdi, Triratna Shrestha, Lyudmyla Barannyk, Gabriel Potirniche, and Indrajit Charit. 2015. "A Creep Damage Model for High-Temperature Deformation and Failure of 9Cr-1Mo Steel Weldments." Metals 5(3):1487–1506. Retrieved (http://www.mdpi.com/2075-4701/5/3/1487/).

Blum, W., P. Eisenlohr, and F. Breutinger. 2002. "Understanding Creep—a Review." Metallurgical and Materials Transactions A 33(2):291–303. Retrieved March 4, 2018 (http://link.springer.com/10.1007/s11661-002-0090-9).

Chilukuru H., Durst K. 2009. "Coarsening of Precipitates and Degradation of Creep Resistance in Tempered Martensite Steels." Mater. Sci. Eng. A Materials Science and Engineering A 510–511(C):81–87.

Kadoya, Y., N. Nishimura, B. F. Dyson, and M. McLean. 1997. “Origins of Tertiary Creep in High Chromium Steels.” in Proceedings of the International Conference on Creep and Fracture of Engineering Materials and Structures.

Lemaître, J. 1990. Mechanics of Solid Materials. Cambridge: Cambridge University Press.

Morra, P. V., S. Radelaar, M. Yandouzi, J. Chen, and A. J. Böttger. 2009. “Precipitate Coarsening-Induced Plasticity: Low Temperature Creep Behaviour of Tempered SAE 52100.” International Journal of Plasticity 25(12):2331–48.

Muñoz-Morris, M. A., I. Gutierrez-Urrutia, and D. G. Morris. 2009. “Influence of Nanoprecipitates on the Creep Strength and Ductility of a Fe–Ni–Al Alloy.” International Journal of Plasticity 25(6):1011–23.

Semba, H., H. Okada, and M. Igarashi. 2008. “Creep Properties and Strengthening Mechanisms in 23Cr-45Ni-7W (HR6W) Alloy and Ni-Base Superalloys for 700°C A-USC Boilers.” Advances in Materials Technology for Fossil Power Plants - Proceedings from the 5th International Conference 168–84.

Shrestha, Triratna et al. 2012. “Creep Deformation Mechanisms in Modified 9Cr–1Mo Steel.” Journal of Nuclear Materials 423(1–3):110–19. Retrieved March 4, 2018 (http://linkinghub.elsevier.com/retrieve/pii/S0022311512000098).

Appendix A: Copyright From International Journal Of Plasticity

Personal use

Authors can use their articles, in full or in part, for a wide range of scholarly, non-commercial purposes as outlined below:

- Use by an author in the author's classroom teaching (including distribution of copies, paper or electronic)
- Distribution of copies (including through e-mail) to known research colleagues for their personal use (but not for Commercial Use)
- Inclusion in a thesis or dissertation (provided that this is not to be published commercially)
- Use in a subsequent compilation of the author's works
- Extending the Article to book-length form
- Preparation of other derivative works (but not for Commercial Use)
- Otherwise using or re-using portions or excerpts in other works

These rights apply for all Elsevier authors who publish their article as either a subscription article or an open access article. In all cases we require that all Elsevier authors always include a full acknowledgement and, if appropriate, a link to the final published version hosted on Science Direct.

https://www.elsevier.com/about/our-business/policies/copyright/personal-use

Appendix B: Copyright from American Nuclear Society

Article Sharing Policy

Duplication of this product and its content in print or digital form for the purpose of sharing with others is prohibited without permission from the American Nuclear Society. Exceptions include:

- Authors are permitted to share their submitted manuscripts (pre-review) anywhere at any time without asking for permission.
- Authors are permitted to share their accepted manuscripts on a departmental website, personal website (including Facebook), and/or an institutional or subject repository (including ResearchGate) after an embargo period of 12 months.

In all cases, an author should provide a link to the version of record (final published version) on the ANS website or a reference to the published article.

http://www.ans.org/pubs/transactions/

Appendix C: Copyright from Metals

Copyright / Open Access

Articles published in *Metals* will be Open-Access articles distributed under the terms and conditions of the Creative Commons Attribution License (CC BY). The copyright is retained by the author(s). MDPI will insert the following note at the end of the published text:

> © 2018 by the authors; licensee MDPI, Basel, Switzerland. This article is an open access article distributed under the terms and conditions of the Creative Commons Attribution License (http://creativecommons.org/licenses/by/4.0/).

http://www.mdpi.com/journal/metals/about